VISCOUS HYPERSONIC FLOW PHYSICS PREDICTIONS USING UNSTRUCTURED CARTESIAN GRID TECHNIQUES

A Thesis
Presented to
The Academic Faculty

by

Susheel Kumar Sekhar

In Partial Fulfillment
of the Requirements for the Degree
Doctor of Philosophy in the
School of Aerospace Engineering

Georgia Institute of Technology
December 2012

VISCOUS HYPERSONIC FLOW PHYSICS PREDICTIONS USING UNSTRUCTURED CARTESIAN GRID TECHNIQUES

Approved by:

Prof. Stephen M. Ruffin, Advisor
School of Aerospace Engineering
Georgia Institute of Technology

Prof. Lakshmi N. Sankar
School of Aerospace Engineering
Georgia Institute of Technology

Prof. Suresh Menon
School of Aerospace Engineering
Georgia Institute of Technology

Prof. Mitchell L. R. Walker
School of Aerospace Engineering
Georgia Institute of Technology

Dr. Jin Wook Lee
Engineering Specialist
The Aerospace Corporation

Date Approved: October 2012

ॐ पूर्ण अदः पूर्ण इदं पूर्णात् पूर्ण उदच्यते[1] ।

Om poorNam adah, poorNam idam, poorNaath poorNam udachyathe;
That is infinite, this is infinite, infinity emanates from the infinite;

पूर्णस्य पूर्ण आदाय पूर्ण एवा वशिष्यते॥

poorNasya poorNam aadaaya, poorNam eva vashishyathe.
When removing infinity from the infinite, the infinite remains.

[1]बृहदारण्यक उपनिषद् (BrhadaaraNyaka Upanishad), while explaining the concept of ब्रह्मन् (Brahman), or the infinite.

For Amma and Appa.

ACKNOWLEDGEMENTS

This long and personally enriching journey would not have been possible without the support of numerous people along the way. I would like to acknowledge and thank every one of them for their contributions.

The incredible support by Prof. Stephen Ruffin, and his patience with me have been invaluable during my stay at the ARTLab. His frank advice and guidance have been instrumental in my completing this dissertation. It has been an absolute joy and pleasure to interact and work with him all along.

I would like to thank the thesis committee members (Prof. Lakshmi Sankar, Prof. Suresh Menon, Prof. Mitchell Walker and Dr. Jin Wook Lee) for agreeing to review my work with such short notice, and for their valuable suggestions and recommendations.

Special thanks to Prof. Jeff Jagoda for his steadfast support during times of adversity. His constant presence in the Aerospace Department at Georgia Tech is ever so reassuring.

My lab mates in the ARTLab have contributed significantly over the many years. Thanks to Dr. Jae Doo Lee, Dr. Jin Wook Lee, Tim Eymann, Joseph Solomon, Dr. Joel Malo-Molina, Srujal Patel, Alessio Orsini, Alexander Klein, Alex Pace, Vikram Aditya Kumar, Matt Bopp, Harsh Khatri, Daniel Baumgartner, Michael Schlottke, Chester Ong, Roman Keller and Manmohan Chandan Prasad. I would like to thank Alex Pace and Matt Bopp for their support in generating reference solutions using DPLR, and Manmohan Chandan Prasad in helping out with high resolution figures.

Countless hours of philosophical ramblings about work, science and life with Dr. Vishwas Iyengar, Dr. Satish Undapalli, Dr. Sachin Jain, Dr. Kaushik Balakrishnan, Dr. Nischint Rajmohan, Prof. Santosh Hemchandra, Ramraj Sundararaj and Kartik Iyer have always been a pleasant distraction.

Special thanks to Ambarish Vaidyanathan, Matt Bopp and Sukanya Randhawa for their unflinching support and help towards the end of my stay here.

And to my parents, thanks very much for being there always with your unconditional love and support. Your never-ending optimism is infectious, and has had a major impact on this work. This is for you.

TABLE OF CONTENTS

LIST OF TABLES

LIST OF FIGURES

SUMMARY

The present work advances and documents the ability of an unstructured Cartesian grid based formulation to model hypersonic viscous flows. This capability is investigated in the solution adaptive solver NASCART-GT. In particular, the effectiveness of modeling viscous phenomena in hypersonic flows using the immersed boundary ghost cell methodology of this solver is examined.

Preliminary comparisons of the surface pressure coefficient, the skin friction coefficient and the convective heat transfer rate predictions for hypersonic flow of argon gas past a 2-D cylinder for a set of Reynolds numbers are made with reference results from a DSMC code and a structured grid CFD solver. Here, the relation between the accuracy of these predictions with the surface cell size is emphasized. Additionally, the correlation between the smoothness of these predictions and the grids used in these simulations is also investigated.

To demonstrate the advantages of the unstructured Cartesian grid in capturing complex flow physics, a hypersonic axisymmetric test case that involves the interaction between a shock wave and a boundary layer, and a separation bubble is chosen. Comparisons of the surface pressure coefficient and the heat transfer rates for this cases are made with experimental results, and the effects of the temperature clipping strategy used in the immersed boundary ghost cell approach are documented.

In each of these tests, novel strategies installed in the adaptive mesh refinement technique of NASCART-GT are explained. Further, to demonstrate that the solver can make good predictions of convective heating at the surface, a range of freestream Mach numbers are chosen, and the overall trend of the predictions are compared with experimental results and empirical estimates for an axisymmetric hemisphere.

Finally, the inviscid thermochemical nonequilibrium solver in NASCART-GT is extended to compute viscous flows by including diffusion terms in the species and energy

conservation equations. Collision cross-section based transport coefficients are also implemented to compute viscosity, thermal conductivity and the species diffusion coefficients. First, comparisons of off-surface flow features for a 2-D cylinder in hypersonic reacting air flow are made with solutions from a body-fitted grid solver. Next, comparison of the stagnation point heat transfer rate in a thermochemical nonequilibrium environment is made with the same body-fitted grid solver for a similar 2-D cylinder geometry, thereby demonstrating the ability of the immersed boundary ghost cell methodology to make good surface predictions in a hypersonic environment.

Overall, the immersed boundary ghost cell approach in the unstructured Cartesian grid framework makes good predictions of the physics and chemistry of hypersonic reacting flows, and compares well with both experiments and body-fitted grid results. The off-surface physics and chemistry agree very well even with coarse grids being used for the simulations. The surface properties have more stringent requirements with respect to surface cell sizes, and compare very well when the thermal boundary layer is resolved adequately.

CHAPTER I

INTRODUCTION

Aerothermodynamics combines the study of the aerodynamics and thermodynamics associated with high speed flight. It is an integral component in the design and implementation of hypersonic transport systems. Vehicles that travel at speeds of around 10 km/s during entry/re-entry scenarios encounter temperatures that are severe, of the order of 10,000 K, and this significantly impacts the design and materials relative to other applications. For example, during the re-entry of the Stardust probe in January 2006, which was sent out to collect interstellar dust samples from two different solar orbits as it flew through the coma of comet Wild 2, a re-entry speed of 12.8 km/s was reached [3, 69, 62], which is the maximum ever by a man-made object. The peak stagnation temperature seen was around 25,000 K, which far exceeds the 6,000 K temperature of the photosphere of the Sun [1].

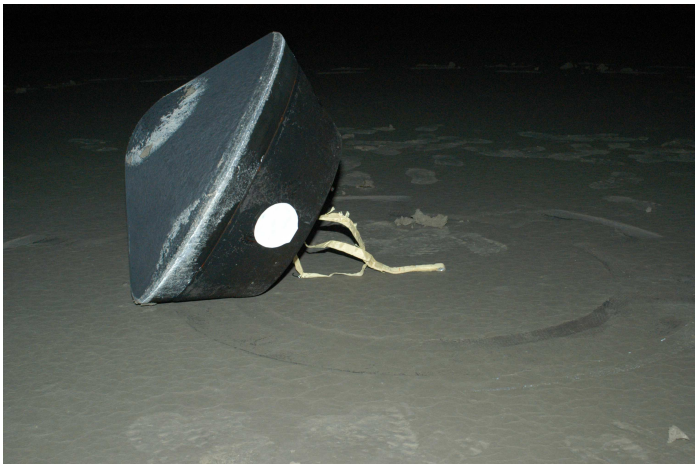

Figure 1: NASA's Stardust sample return capsule[a]

[a] http://stardust.jpl.nasa.gov/photo/er_capsule_ground.jpg

Under such unforgiving conditions, it is critical that prior knowledge of the impending flow environment is available beforehand to ensure a safe and effective design of these transport vehicles. Accurate estimates of the aerodynamic forces and heat transfer rates are critical in trajectory analysis and for payload weight considerations [31, 108].

The prediction of the surface physics is particularly important under these circumstances as it directly affects the design and materials of the TPS (Thermal Protection System). Appropriate TPS design is essential for the survival of the payload which may include critical expensive scientific equipment and/or life in the form of astronauts. Such deliberations, in turn, affect the weight of the payloads of these transport systems, as well as the choice of the propulsion system itself. Looking at the Stardust spacecraft again, the peak stagnation heating during re-entry of the capsule reached 1,200 W/cm^2. Special ablative TPS materials had to be installed to protect the payload, which for this mission was an aerogel with cosmic dust samples. In this case, NASA used PICA-15 (Phenolic Impregnated Carbon Ablators) developed at Ames Research Center for the TPS, which took up nearly 22% of the total mass of the probe. The ablative characteristics of PICA have been shown to withstand heat flux magnitudes of up to 3,360 W/cm^2 [95].

The extreme conditions encountered by a spacecraft during entry/reentry situations are difficult to reproduce experimentally. High costs are incurred to generate the low pressure/density and high enthalpy environments. The energy required to produce such conditions can be unsurmountable, and the number of capable facilities equipped to conduct these experiments are limited. Analytical expressions and empirical formulations make far too many assumptions to have a wide range of applicability in hypersonic flow cases. Computational Fluid Dynamics (CFD) tools are a cheaper alternative to the experiments, and have been used extensively with various levels of success over the past decades in the design of a multitude of space probes: Mars Pathfinder [27, 66, 28], Stardust [69, 62], Huygens-Cassini [44, 101], and the recent Mars Science Lab [23, 104, 24, 25], to name a few.

Advances in high performance computing trends have had a very positive impact on the complexity of the simulations being conducted. Increasing computer speeds and reducing costs of hardware have allowed for calculations to include more physical and chemical processes in the flow. Problems that would generally take days and even weeks to complete a decade ago can be run in significantly less time today. For example, the first instance of computing hypersonic flows in thermochemical nonequilibrium was carried out almost two decades ago for a simple 2-D test case [79]. Using a modest 50,000 grid points on a 20

Mflops supercomputer, this simulation took several hours to compute. Today, the fastest supercomputers can reach petaflop speeds, which are nine orders of magnitude faster [2]. More recently, the massively parallel architecture of current video cards (GPUs) have added an additional dimension to the computing resources, changing the landscape of high performance computing altogether [93].

1.1 Challenges in Hypersonic Flow Simulations

At hypervelocities, the assumption of a perfect gas fails due to effects of the high temperatures associated with such flow conditions. The excitation of internal energy modes and the occurrence of chemical reactions require modifications to the standard Navier-Stokes equations that represent ideal gas flows.

When a high speed fluid is decelerated to near stagnation at the surface of a vehicle, the kinetic energy associated with such a flow is converted to internal energy, causing a very large increase in temperature. Stagnation regions in such situations could generate temperatures as high as 25,000 K (for e.g. Stardust). Due to very high flow speeds and relatively low densities in the freestream, the distances between shock waves and the spacecraft are generally very small. With the high temperatures near the surface, boundary layers associated with these flows are also much thicker than those seen at lower temperatures. These phenomena combine in creating a viscous-shock layer, complicating the physics of the flow.

The sudden transfer of a large amount of kinetic energy into internal energy results in the excitation of various internal energy modes of the gas. Chemical reactions amongst the constituent species can happen if the temperature is high enough to facilitate their occurrence. Such reactions can change the physical and chemical properties of the gas, and its response at the surface of the spacecraft.

In the case of monotomic gases, the translational mode of internal energy can get excited. For diatomic gases, additional rotational and vibrational modes of internal energy can get activated. With each internal energy mode having a different rate of excitation and relaxation, the prevalence of multiple temperatures associated with each mode can be

observed under such circumstances.

At even higher temperatures, ionization of the gas molecules can result, leading to more complex flow phenomena. The presence of ionized gases enhances the radiation emitted by the shock layer, which needs to be taken into account while designing the TPS of hypersonic vehicles. Also with reacting gases, depending on the catalycity of the wall material, such reactions could cause ablation of the heat shield surface, injecting different chemical species into the flow.

It is therefore imperative that the fluid flow model equations take into account all of these phenomena to yield correct predictions of heat transfer and aerodynamic loads in hypersonic flows.

1.2 Governing Equations

The model equations derived by Lee [52] in a seminal work almost three decades ago are inclusive of the phenomena explained in the previous section. These equations have since been presented by Gnoffo et al. [30], Park [76], Candler [14] and others. The Navier-Stokes equations have been presented in these references accounting for differences in temperatures associated with translation-rotational, vibrational and electronic internal energy modes. All assumed that the translational and rotational modes equilibrate very fast, and were therefore represented by a single temperature. Gnoffo et al. [30] further simplified the equations assuming that the vibrational and electronic modes were in equilibrium, resulting in a two-temperature thermochemical nonequilibrium model.

Also, due to the chemically reacting nature of hypersonic flows, transport properties associated with the gas must take into account the local chemical composition of the gas mixture. Gupta et al. [34] reviewed and presented the reaction rate coefficients and transport properties for a 11-species air model, with curve fits for various parameters in the high-energy environment. McBride et al. [60, 61] have presented similar curve fits for reacting gases for various other species, enabling the computation of thermodynamic and transport properties for any combination of species.

With the availability of the detailed model equations and a comprehensive set of data for

various gases, the next step would be to investigate the current state-of-the-art in computing hypersonic flows.

1.3 CFD Tools

Notwithstanding the challenging physics and chemistry modeling in hypersonic flows, the situation is further intensified by the implications of such extreme conditions on CFD tools. Extremely high Mach numbers, vacuum like environments with very low densities and temperatures, and borderline continuum-rarefied settings each introduce challenges in programming an effective solver to compute hypersonic flows. These are further complicated with the presence of chemical reactions, ionization, radiation and ablative phenomena. Ablation could also introduce turbulence in the surrounding flow which can constitute a separate field of study altogether. Additionally, the shapes of vehicles that do not conform to simple geometric patterns add an extra dimension of complexity. Due to these challenges, the prediction of aerodynamic heating in a hypersonic flow is considered a cornerstone enabling requirement [108].

In situations where the hypersonic flow environment encounters very low density gases in vacuum like conditions, DSMC (Direct Simulation Monte Carlo) techniques have been able to make very good predictions of the flow [13, 64, 96, 65, 71, 12, 54]. Developed by Bird [8, 9], DSMC techniques consider the individual gas molecules and trace the motion of each of these molecules using a statistical Monte Carlo simulation. Codes, such as the DS2V/3V Program Suite [10] and MONACO [21] have been used extensively to simulate hypersonic rarefied gas flows. Additionally, hybrid DSMC-Navier Stokes simulations have also been carried out, where regions of high Knudsen number are computed using a DSMC solver and the rest of the domain is solved using a continuum solver [102, 86, 87, 88, 85]. Extra care is required in considering the overlap region where the gas can be considered neither continuum nor rarefied. Monte Carlo simulations become prohibitively expensive when used in regions of low Knudsen numbers.

Several finite volume CFD solvers have been developed to solve chemically reacting hypersonic continuum flows. With the current study aimed at tackling this problem, these

are further explained in the following sub-sections.

CFD codes can be broadly categorized into structured and unstructured grid solvers depending on the topology of the discretization strategy. Each technique has its own set of advantages and disadvantages. Whereas body-fitted structured grids have been used for a significantly longer period of time in the field of hypersonics resulting in a extensive knowledge-base, recent developments in the field of high performance computing have made unstructured grids a more attractive and viable option. A series of review papers in the recent past have highlighted and documented the state-of-the-art in hypersonic flow modeling [31, 32, 108, 17, 11, 56]. A few prominent solvers amongst many are detailed in the following sub-sections.

1.3.1 Hypersonic Structured Grid Solvers: State-of-the-Art

Body-fitted, structured grid solvers have in the past established their capability in predicting viscous hypersonic flows. These grids are orthogonal to the surface panels, facilitating the implementation of exact boundary conditions at the wall [41]. NASA codes LAURA [29] and DPLR [105] have been shown to predict off-surface flow features, as well as surface phenomena such as hypersonic convective heating to very good levels of accuracy [40].

LAURA (Langley Aerothermodynamic Upwind Relaxation Algorithm) uses an upwind-biased, point-implicit or a line-relaxation algorithm for three-dimensional, viscous, compressible flows. It uses a finite-volume formulation that sets up the inviscid fluxes using Roe's averaging and Harten's entropy fix with second-order corrections based on Yee's symmetric total variation-diminishing scheme. The viscous terms are discretized by using a central difference scheme.

DPLR (Data-Parallel Line Relaxation) uses data-parallel line relaxation methodology to integrate the equations to steady state. Here, the inviscid fluxes are computed using a modified (low-dissipation) form of the Steger-Warming flux vector splitting scheme [55], with a third-order spatial accuracy obtained using MUSCL extrapolation coupled with a minmod limiter.

Both of these solvers are parallel, multi-block, structured, finite volume codes that

solve the reacting Navier-Stokes equations including finite-rate chemistry and the effects of thermal nonequilibrium. DPLR assumes that the species remain in the electronic ground state, whereas LAURA assumes that the electronic mode to be excited and in equilibrium with the vibrational mode.

Other structured grid codes, such as GASP [4] and GIANTS [70], have also been used effectively in computing flow physics in the hypersonic regime.

Unfortunately, the amount of time, effort and expertise required in setting up a test case for complicated transport geometries can be quite a deterrent with such structured grid solvers. For example, during the X-33 design phase, it took approximately four weeks just to construct a high-quality multi-block structured grid for LAURA [31]. Therefore, the desire for an unstructured grid code [32] capable of computing viscous diffusion phenomena in the hypersonic environment is the motivation behind this work.

1.3.2 Hypersonic Unstructured Grid Solvers: State-of-the-Art

To avoid the extensive time and expertise required in setting up effective body-fitted grids around hypersonic transport systems for structured grid solvers, there has recently been a concerted effort made in moving towards unstructured grid solvers.

Primarily, the relative ease of grid generation and the capability of performing solution adaption without having to consider the deformation of the grid topology have driven this effort. Advancements in high speed computing and cheaper memory costs have increased the attractiveness of unstructured grid solvers, which require the explicit determination and maintenance of neighbor cell information [92]. Parallelization of these codes has further reduced the costs of running such test cases, making them ideal for simulations around complex geometries.

LeMANS (Le Michigan Aerothermodynamic Navier-Stokes code) [83], for example, has been extensively used in computing and analyzing hypersonic reacting flows. It is a parallelized finite-volume solver that is capable of simulating gases in thermal and chemical nonequililbrium. It uses a modified Steger-Warming FVS scheme, and is 2^{nd} order accurate in space and time. A 2-temperature model is used to account for the nonequilibrium

between vibrational and translational-rotational modes, and the energy exchange rates are modeled using the Landau-Teller model. Different boundary conditions, including no-slip and slip velocity and temperature are enforced.

Of the aforementioned body-fitted grid solvers, attempts have been made to extend the technology of LAURA and DPLR to the unstructured framework. FUN3D [5] and US3D [68], respectively, have been efforts along these lines, with the former using a tetrahedral framework and the latter accommodating tetrahedral, prismatic and hybrid hexahedral-prismatic-tetrahedral grids.

FUN3D is the product of the integration of the structured grid external flow solver (LAURA) and an internal flow solver (VULCAN [103]). It is a tetrahedral grid based code that was developed to implement robust schemes with quantified uncertainties, resulting in minimum user intervention for hypersonic applications. However, hypersonic stagnation region heat transfer predictions using FUN3D have been significantly poorer compared to LAURA [32].

The accuracy of the predictions were found to be very sensitive to the choice of algorithm, with the high aspect ratio, poorly aligned, tetrahedral cells complicating high Reynolds number simulations, compared to locally structured meshes aligned to the flow (Fig. 2). Particularly, the prediction of the post-shock velocities and entropy that are convected to the edge of the boundary layer significantly affected the quality of the heat transfer predictions [32].

This was further investigated by Nompelis et al. [67], who studied various configurations of the unstructured grids to compare hypersonic heat transfer predictions (Fig. 3). Heating estimates were found to be very sensitive to the grid design due to the extremely large gradients near the shock.

Here again, the inability of the poorly shock-aligned tetrahedral cells to produce a smooth shock introduced pronounced errors in the subsonic entropy layer behind the bow shock. This resulted in a poorly resolved solution affecting the heat transfer rate, compared to shock-aligned hexahedral cells. Refining the tetrahedral cells around the shock did improve the solution significantly, showing that the quality of the predicted solution depends

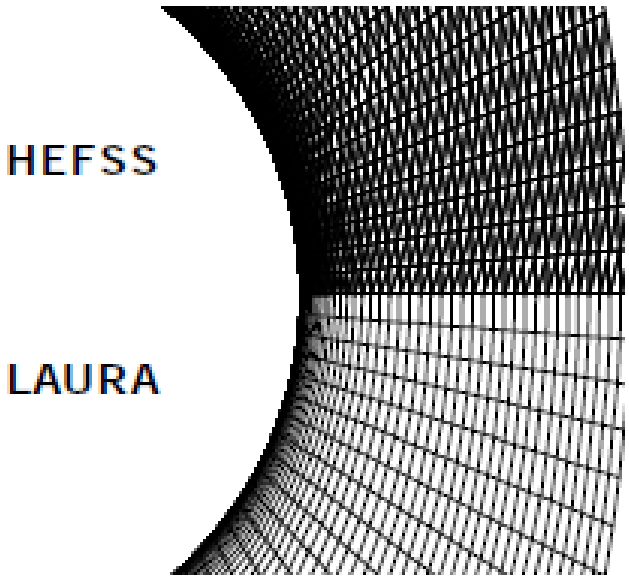

Figure 2: Structured grid (bottom) and equivalent uniformly biased unstructured grid (above) in Ref. [32]

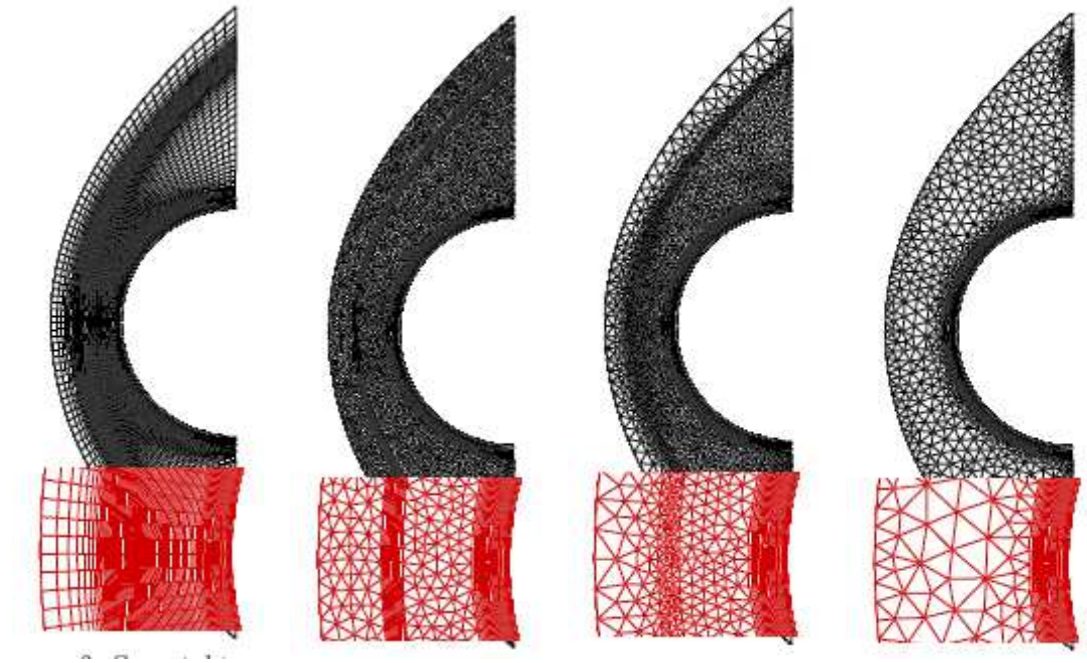

(a) Fully hexahedral mesh (b) Hexahedral near shock and wall (c) Clustered tetrahedral mesh (d) Isotropic tetrahedral mesh

Figure 3: Grid configurations in Ref. [67]

both on the orientation of the cell boundaries to flow features, as well as the size of each control volume.

US3D uses the same data-parallel line relaxation integration scheme that DPLR does,

but has an option of using this in the boundary layer region alone. Elsewhere, it uses a point-implicit scheme. Using tetrahedral elements for an inviscid analysis, Candler et al. again confirmed the observations made by Gnoffo and White [32], elucidating the sensitivity of the shock solution to the grid alignment [15]. Based on the results of simulations with various configurations (Fig. 4), it was shown that the lack of alignment of tetrahedral cells to the shock resulted in the injection of spurious momentum into the flow field, poorly predicting the post-shock velocities.

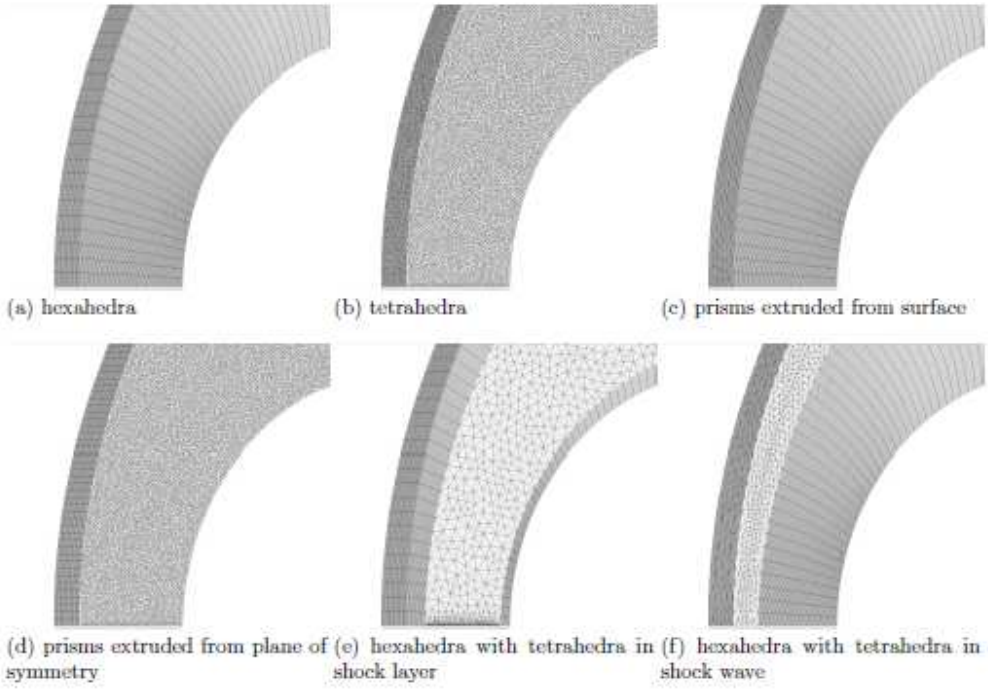

Figure 4: Computational grids used in Ref. [15]

Further, when hexahedral cells were used at the shock, such non-physical velocity and entropy predictions were controlled, significantly improving the flow physics estimations. As the cylinder analysis was conducted for an inviscid flow, the effect of the surface cells on heat transfer were not investigated for this setup. Results of the convective heat transfer rate over a sphere did show discrepancies between triangular and quadrilateral surface cells (triangular cells over-predicted the stagnation point heat transfer rate by $\approx 15\%$), but the inference was inconclusive because the reason behind the difference was unknown.

In computing the flux terms, the Cartesian grid framework is advantageous relative to

other unstructured grid topologies, like tetrahedral or prismatic grids, as it is associated with perfectly orthogonal grid cells. Complex coordinate transformations and calculations of contra-variant velocities can be avoided, thus reducing the truncation error. Also, such a framework eliminates the need for body-fitted cells, allowing for automatic grid generation around even very complex geometries.

Several studies have been carried out to compute viscous flows using unstructured Cartesian grids. Marshall [57] showed that such a framework could indeed be used to predict viscous fluid physics for subsonic, transonic and supersonic test cases. Laminar flows alone were considered in that study, and very good predictions of the surface pressure and skin friction coefficients were made and compared with experiments. Lee [50] extended this capability to the turbulent regime using the κ-ϵ model, with particular application to rotorcrafts. Here too, comparisons with experiments showed excellent agreement of the surface pressure and skin friction coefficients. Both of these studies were carried out in the NASCART-GT flow solver, using Roe's Approximate Riemann Solver.

Chemically reacting inviscid fluids in thermal nonequilibrium have also been computed using the Cartesian grid framework. Tu [97] implemented a two-dimensional, two-temperature thermochemical nonequilibrium Euler solver, and showed very good off-surface flow physics prediction capability using unstructured Cartesian grids. That code used the HLLC Approximate Riemann Solver for inviscid flux vectors. Lee [51] further extended the frozen flow capability of NASCART-GT to compute inviscid flows in thermochemical nonequilibrium using the AUSMPW+ scheme. A point-implicit solver was implemented to compute the chemical source terms, and the off-surface physics compared very well with those computed using DPLR.

Hypersonic convective heat transfer predictions continue to remain a challenge, requiring accurate estimations of the surface temperature gradients. Hamilton et al. [35, 36] have used approximate methods to predict convective heat transfer rates based on the chemically reacting inviscid solution using unstructured Cartesian grids. Studies with both laminar and turbulent flows were conducted and rapid approximate predictions were made for preliminary TPS design concepts. Good comparisons with LAURA show potential for

implementing such a methodology during the intial stages of the design process.

Being a subset of the hexahedral mesh topography, Cartesian cells can be better aligned to the shock in front of a bluff body, when compared to tetrahedral cells. The normal shock portion generally orients itself along the Cartesian directions, resulting in good predictions of the flow physics even for hypersonic Mach numbers. Tu [97] and Lee [51] have shown this for inviscid flows, and Sekhar et al. [90] presented preliminary comparisons for viscous hypersonic flows using the unstructured Cartesian grid framework.

For the portion of the shock away from the stagnation region, the Cartesian cell topology lends itself to be misaligned to the shock-shape. Such misalignment can also be observed for sharp bodies, such as wedges, where oblique shocks are often encountered. Nompelis et al. [67] showed that the accuracy of the post-shock velocities and entropy can be significantly improved by refining shock-misaligned cells for a tetrahedral mesh. Given the solution adaption capability of Cartesian solvers such as NASCART-GT, shock regions are typically well refined using very fine Cartesian cells. This efficient refinement of shock regions has been shown to provide very good predictions of shock shape and overall post-shock flow physics [57, 51].

Also, the surface pressure variation and the skin friction coefficient predictions using Cartesian cells for different Mach regimes (subsonic, transonic and supersonic) have been established [57, 50]. The estimation of these parameters in the hypersonic regime, combined with the lack of conclusive investigation into the heat transfer prediction capability using non-surface-aligned cells (specifically Cartesian cells) are the motivation behind this research effort.

1.4 Scope of Present Work

The inherent advantages of the unstructured Cartesian grid framework make it an attractive alternative to body-fitted structured meshes, and even other unstructured grid topologies. Recent research of this technology have shown significant advances in computing flows under various conditions, with applications ranging from LES of turbulence to moving body analyses. However, there is a dearth of comprehensive research studies on utilizing

this technique in computing viscous, hypersonic flows. The present work seeks to fill that gap. Specifically, the combination of this framework with the immersed boundary method is used as the basis for this research effort. Additionally, viscous, hypersonic flows in thermochemical nonequilibrium are simulated to advance the state-of-the-art in this field. This is a first such effort, and will lay the foundation for further essential studies in this area. The overall outline of the research effort is given below.

As a preliminary exercise, the capacity of the immersed boundary ghost cell approach in NASCART-GT to predict the surface physics in a hypersonic non-reacting environment is investigated. High velocity argon gas flows past a 2-D cylinder are simulated for a set of freestream conditions (Reynolds numbers), and the impact of grid cell sizes on the quality of solution is evaluated. Additionally, the solver's prediction ability is verified over a series of hypersonic Mach numbers for flows past a hemisphere, and compared to experimental data and empirical estimates.

A test case that involves complex hypersonic flow physics is chosen, and the advantages of using an unstructured Cartesian mesh are demonstrated next by using the adaptive mesh refinement strategy installed in the solver. This setup involves flow separation and the interaction between a hypersonic shock wave and a boundary layer, and is studied using this unstructured Cartesian grid framework. The immersed boundary ghost cell approach is tested with two temperature clipping strategies, and their impact on the overall solution accuracy and smoothness of the surface property predictions are compared.

Finally, having incorporated the species diffusion terms in the conservation equations, and collision cross-section based transport coefficients, reacting flow environments are next studied, and comparisons of the off-surface flow physics and the surface physics predictions are made. First, a 2-D cylinder in a hypersonic reacting air flow is tested with an adiabatic wall boundary condition. Next, the same 2-D cylinder geometry is tested to evaluate the isothermal wall boundary condition, and to identify the strengths and weaknesses of the immersed boundary ghost cell methodology in computing convective heating rates in a hypersonic environment.

This dissertation is organized as follows. Chapter 2 details the governing equations, and

the physics and chemistry models that set the stage for the analysis of hypersonic flows. In Chapter 3, the numerical tools incorporated in NASCART-GT that are used to compute these flows are explained. This includes the time integrations schemes as well as the immersed boundary ghost cell approach. Chapters 4, 5 and 6 present the results of hypersonic flow studies, with comparisons with experiments and other CFD results included. Conclusions are drawn and recommendations for further research in this area are summarized in Chapter 7.

CHAPTER II

MATHEMATICAL FORMULATION

At hypersonic speeds, accurate aerothermodynamic predictions of the near-field and far-field flow features require detailed definitions of the fluid property gradients, transport mechanisms of various attributes of the fluid, chemical compositions and reaction rates, and the state of the gas throughout the computational domain. The governing equations that are used to compute fluid flows at subsonic or supersonic speeds fail to model the complex phenomena that are encountered when internal energy modes of the gas are excited. The perfect gas assumptions made in the basic Navier-Stokes equations should therefore be extended to account for these modes, as well as to compute the chemical reactions that are seen at such extreme conditions. In this chapter, model equations that are used to describe such physical processes and chemical reactions are detailed.

2.1 Conservation Equations

Conservation equations for the simulation of fluid flows in thermochemical nonequilibrium are presented in this section. It is primarily assumed that the fluid under consideration satisfies the continuum hypothesis, i.e. the Knudsen number (defined as the ratio of the mean free path of the gas to the characteristic length scale of the flow) associated with the fluid flow is small enough that the continuum formulation (Navier-Stokes) of the fluid dynamics can be used, instead of the molecular dynamics formulation (Boltzmann).

It is important to emphasize this assumption given that much of the flow regimes that are encountered in hypersonic flight range between continuum and free-molecular. Additionally, the low densities in such environments lend to added complexities in the flow physics and chemistry. The combination of low densities and the high velocities that dominate these situations creates an environment where the time taken by the bulk fluid flow to adjust to the body under consideration and the relaxation time for the internal energy modes to equilibrate are comparable. Generally, at lower speeds and sea-level densities, the

bulk fluid motion accommodates to the body at a much slower rate than the equilibration process of the internal energy modes (aided by increased number of molecular collisions at higher densities). Therefore, simpler perfect gas assumptions can be used to compute such flow conditions. With these assumptions failing for hypersonic flow regimes, it is critical to account for such nonequilibrium phenomena while setting up the model equations to compute these flows as they affect various aspects of the flow environment, such as shock stand-off distances, surface pressure distributions, peak temperatures in the flow, etc.

Much of the equation sets presented below were derived from the works of Lee [52], Gnoffo et al. [30], Park [76] and Candler [14]. This formulation accounts for the fact that the translational and rotational modes of internal energy equilibrate very fast (within a few molecular collisions), and can thus be represented by a single temperature. Further, considering that the process of exchange of energy between these and the vibrational mode is much slower, a separate temperature is used to define the vibrational internal energy. Thus, nonequilibrium in this formulation is manifested in the form of a two-temperature model. The conservation equations in tensor form can be written as:

$$\frac{\partial \rho}{\partial t} + \frac{\partial}{\partial x^i}\rho u^i = 0 \tag{1}$$

$$\frac{\partial}{\partial t}\rho u^j + \frac{\partial}{\partial x^i}\rho u^j u^i + \frac{\partial p}{\partial x^j} = \frac{\partial}{\partial x^i}\left[\mu\left(\frac{\partial u^j}{\partial x^i} + \frac{\partial u^i}{\partial x^j}\right) + \lambda \frac{\partial u^k}{\partial x^k}\delta^{ij}\right] \tag{2}$$

$$\frac{\partial}{\partial t}\rho e + \frac{\partial}{\partial x^i}\rho\left(e + \frac{p}{\rho}\right)u^i = \frac{\partial}{\partial x^i}\left(K_{tr}\frac{\partial T_{tr}}{\partial x^i} + K_v \frac{\partial T_v}{\partial x^i}\right) + \frac{\partial}{\partial x^i}\left(\rho \sum h_s D_s \frac{\partial \chi_s}{\partial x^i}\right) + \frac{\partial}{\partial x^i}\left[u^j \mu\left(\frac{\partial u^j}{\partial x^i} + \frac{\partial u^i}{\partial x^j}\right) + u^j \lambda \frac{\partial u^k}{\partial x^k}\delta^{ij}\right] \tag{3}$$

$$\frac{\partial \rho_s}{\partial t} + \frac{\partial}{\partial x^i}\rho_s u^i = \frac{\partial}{\partial x^i}\left(\rho D_s \frac{\partial \chi_s}{\partial x^i}\right) + \dot{\omega}_s \tag{4}$$

$$\frac{\partial}{\partial t}\rho e_v + \frac{\partial}{\partial x^i}\rho e_v u^i = \frac{\partial}{\partial x^i}\left(K_v \frac{\partial T_v}{\partial x^i}\right) + \frac{\partial}{\partial x^i}\left(\rho \sum h_{v,s} D_s \frac{\partial \chi_s}{\partial x^i}\right) + \sum \rho_s \frac{e^*_{v,s} - e_{v,s}}{\langle \tau_s \rangle} + \sum \dot{\omega}_s \hat{e}_{v,s} \tag{5}$$

These model conservation equations include the total density equation (Eq. 1), 3 momentum equations (Eq. 2), the total energy equation (Eq. 3), individual species density equations (Eq. 4) and the vibrational energy equation (Eq. 5). Here, ρ and ρ_s are the total and individual species densities of the gas, respectively, u^i is the bulk velocity along the i^{th} direction, e and e_v are the total and the vibrational energies per unit mass of the gas, respectively, p is the static pressure associated with the gas, T_{tr} and T_v are the translational-rotational and vibrational temperatures of the gas, respectively.

It should be noted that ionization is taken to be absent in this formulation even though it is based on a single temperature representing the vibrational and electronic internal energy modes. Also, the vibrational energies of different molecules are all assumed to be in equilibrium with each other, thereby requiring a single vibrational temperature to model this internal energy mode. These simplifications may not be adequate for problems that involve much higher temperatures and radiation, but provide reasonable results for most reentry configurations [30]. Furthermore, the accuracy of multi-vibrational temperature models are limited by the quality of the available data that describes the energy exchange between individual species vibrational energy modes.

The terms in each of these equations are arranged such that the time rate of change of the conserved variables and the advective processes that transport the conserved variables lie on the left hand side, whereas the dissipative processes and the source terms lie to the right of the equality sign. These are explained below and in the subsequent sections of this chapter.

The mixture density is the sum of the individual species densities in the gas, and the total pressure is defined based on Dalton's law of partial pressures:

$$\rho = \sum \rho_s \tag{6}$$

$$p = \sum p_s = \sum \rho_s \bar{R} T_{tr} / M_s \tag{7}$$

Here, $\bar{R}$ is the universal gas constant and M_s is the molecular weight of species s. The

total energy is defined as the sum of internal energy modes of the gas, plus the heat of formation of each species and the kinetic energy of the bulk gas:

$$e = \sum C_{V,s} T_{tr} + \sum e_{v,s}\left(T_v\right) + \sum h_s^\circ + \frac{u^i u^i}{2} \tag{8}$$

where, $C_{V,s}$ is the specific heat capacity of species s at constant volume. This includes the translational and rotational components of the specific heat capacity. The vibrational energy in this two-temperature gas model is evaluated by subtracting the calorically linear translational-rotational mode of internal energy, the heats of formation and the bulk kinetic energy from the total energy at the vibrational temperature:

$$e_v\left(T_v\right) = e\left(T_v\right) - \sum C_{V,s} T_v - \sum h_s^\circ - \frac{u^i u^i}{2} \tag{9}$$

With that explanation of the parameters that constitute the advective terms in the conservation equations, the viscous diffusion terms are explained in the next section.

2.2 Transport Properties

The viscous diffusion terms in the governing equations describe the transport of momentum, energy and species concentrations across the control volume. In this study, the fluid is assumed to be Newtonian for the viscous stresses, and Fourier's law and Fick's law are used to determine the heat transfer rates and the species diffusion rates, respectively.

The computation of the transport coefficients, i.e. the viscosity (μ), thermal conductivities (K_{tr}, K_v), and the species diffusion coefficients (D_s), are explained here. For a perfect gas, Sutherland's formulation (Eq. 10) is generally used to determine molecular viscosity. This model is valid for temperatures below 1,000 K. Additionally, thermal conductivity is computed from the relation between the Prandtl number and molecular viscosity (Eq. 11). Of course, species diffusion is absent for a perfect gas.

$$\mu = C_1 \frac{T^{3/2}}{T + C_2} \tag{10}$$

$$\kappa = \frac{\mu C_p}{\mathrm{Pr}} \tag{11}$$

In Eq. 10, μ is the viscosity of the gas, T is the temperature at which the viscosity is being computed and C_1 and C_2 are the Sutherland's coefficients for that gas. In Eq. 11, C_p is the specific heat constant at constant pressure for that gas and Pr is the Prandtl number. Also, the bulk viscosity (λ) is determined using Stokes' hypothesis, i.e.:

$$\lambda = -\frac{2}{3}\mu \tag{12}$$

For a gas in thermal nonequilibrium, the computation of the transport properties must take into account the differences in the temperatures associated with the internal energy modes [52]. There can be significant differences in the values of the diffusion coefficient, viscosity and the thermal conductivity, depending on the extent of the nonequilibrium phenomenon. Furthermore, individual contributions from the reacting constituents of the gas in chemical nonequilibrium must also be considered.

For temperatures above 1,000 K, where the Sutherland's model for transport properties fails, empirical relations based on the collision cross-sections can be used instead. The formulations of Lee [52], Gnoffo et al. [30] and Gupta et al. [34] are given below. These use a simplification of the first-order Chapman-Enskog approximation of the mixing rule [34], which is adequate for weakly ionized gases. The mixing rule is extended to a gas in thermal nonequilibrium by evaluating collision integrals at the controlling temperatures. The integrals for heavy particles are based on the translational-rotational temperature. These are evaluated as curve fits to tabulated data [34, 61].

$$\begin{aligned}
\pi\bar{\Omega}_{si}^{(1,1)} &= \left[\exp\left(D_{\bar{\Omega}_{si}^{(1,1)}}\right)\right] T^{\left[A_{\bar{\Omega}_{si}^{(1,1)}}(\ln T)^2 + B_{\bar{\Omega}_{si}^{(1,1)}} \ln T + C_{\bar{\Omega}_{si}^{(1,1)}}\right]} \\
\pi\bar{\Omega}_{si}^{(2,2)} &= \left[\exp\left(D_{\bar{\Omega}_{si}^{(2,2)}}\right)\right] T^{\left[A_{\bar{\Omega}_{si}^{(2,2)}}(\ln T)^2 + B_{\bar{\Omega}_{si}^{(2,2)}} \ln T + C_{\bar{\Omega}_{si}^{(2,2)}}\right]}
\end{aligned} \tag{13}$$

The integrals in Eq. 13 are modified and used in the determination of transport properties. The modified integrals take the form (Eq. 14):

$$\Delta_{si}^{(1)}(T) = \frac{8}{3}\left[\frac{2M_sM_i}{\pi\bar{R}T(M_s+M_i)}\right]^{1/2}\pi\bar{\Omega}_{si}^{(1,1)}$$
$$\Delta_{si}^{(2)}(T) = \frac{16}{5}\left[\frac{2M_sM_i}{\pi\bar{R}T(M_s+M_i)}\right]^{1/2}\pi\bar{\Omega}_{si}^{(2,2)} \tag{14}$$

To take into account the composition of the gas whose transport coefficients are the be determined, the molar concentration of the species s in the mixture is defined as:

$$c_s = \frac{\rho_s}{\rho M_s} \tag{15}$$

Thus, based on the collision integrals and the species concentrations, the viscosity of the gas mixture is computed using the following expression:

$$\mu = \sum \frac{m_s c_s}{\sum_{i=1}^{Ns} c_i \Delta_{si}^{(2)}(T)} \tag{16}$$

Here, m_s is the mass of a single particle of species s.

The expression for the thermal conductivity associated with the translation mode of internal energy is given in Eq. 17. k in the formula is the Boltzmann's constant.

$$K_t = \frac{15}{4}k\sum \frac{c_s}{\sum_{i=1}^{Ns} a_{si}c_i\Delta_{si}^{(2)}(T)} \tag{17}$$

Here, the nondimensional parameter a_{si} is defined as:

$$a_{si} = 1 + \frac{[1-(m_s/m_i)]\,[0.45 - 2.54\,(m_s/m_i)]}{[1+(m_s/m_i)]^2} \tag{18}$$

To compute the thermal conductivity of the gas mixture associated with the rotational mode of internal energy, the molecules are assumed to be fully excited and the formulation is given by:

$$K_r = k\sum_{\text{molec}} \frac{c_s}{\sum_{i=1}^{Ns} c_i\Delta_{si}^{(1)}(T)} \tag{19}$$

The conductivity of the mixture for the combination of translational and rotational modes is thus taken as the sum of the individual components. The vibrational component of thermal conductivity is assumed to be equal to the rotational component.

$$K_{tr} = K_t + K_r \tag{20}$$

$$K_v = K_r \tag{21}$$

To account for the species diffusion phenomena occurring due to the gradients in species concentrations across the flow, consider the binary diffusion coefficient for a pair of particles. This is defined as:

$$D_{si} = \frac{kT}{p\Delta_{si}^{(1)}(T)} \tag{22}$$

The effective diffusion coefficient of species s in the entire gas is given by:

$$D_s = \frac{c_t^2 M_s (1 - M_s c_s)}{\sum_{\substack{i=1 \\ i \neq s}}^{Ns} (c_i / D_{si})} \tag{23}$$

Here, c_t is the sum of the molar concentrations of all the species in the entire gas mixture:

$$c_t = \sum c_s \tag{24}$$

Also, the species mole-fractions are defined as:

$$\chi_s = \frac{(\rho_s / M_s)}{\sum_{i=1}^{Ns} (\rho_i / M_i)} \tag{25}$$

2.3 Chemistry Model

Next, the chemistry model used to compute the chemical source term is explained here. A standard finite-rate chemistry model is assumed for the reacting gas. The equation for a single generic chemical reaction can be represented as [100]:

$$\sum_{i=1}^{Ns} \nu_i' \mathbf{X}_i \underset{k_b}{\overset{k_f}{\rightleftharpoons}} \sum_{i=1}^{Ns} \nu_i'' \mathbf{X}_i \tag{26}$$

Here, $\mathbf{X}_i$ represents the participating species in the reaction, and ν_i' and ν_i'' are the stoichiometric coefficients corresponding to each species, on the reactants side and the products side, respectively.

During chemical nonequilibrium, the difference between the rates of production and destruction of a species constitutes the chemistry source term. For each species, during each reaction, this can be represented as:

$$\frac{d\mathbf{X}_i}{dt} = \left(\nu_i' - \nu_i''\right)\left\{k_f \prod_{Ns} \left[\mathbf{X}_i\right]^{\nu_i'} - k_b \prod_{Ns} \left[\mathbf{X}_i\right]^{\nu_i''}\right\} \tag{27}$$

Summing this term over all the reactions, and multiplying by the molecular weight of each species yields:

$$\dot{\omega}_s = M_s \sum_{i=1}^{Nr} \frac{d\mathbf{X}_i}{dt} \tag{28}$$

The forward and backward reaction rate constants are very sensitive to temperature, and therefore, in thermochemical nonequilibrium flow simulations, significant differences in the reaction rate constants can be seen depending on the temperatures used in the calculations. The forward reaction rate constant is computed in the Arrhenius form as follows:

$$k_f\left(T_q\right) = C_f T_q^{\eta} \exp\left(-E_f/kT_q\right) \tag{29}$$

T_q in the above equation represents the temperature at which the forward reaction rate constant is determined. Depending on the chemical model, this parameter can take different forms, resulting in more reactive or less reactive gases. Park [74] suggested the use of a temperature that represents both translational-rotational as well as the vibrational modes of internal energies. This model assumes that the reaction rate constants are governed by the geometric average of these temperatures:

$$T_q = \sqrt{T_{tr} T_v} \tag{30}$$

Lee [51] implemented this, as well as models recommended by Dunn and Kang [22], Gupta [34], and Park [72, 75, 77, 74, 78] for the forward reaction rate constants. The backward reaction rate constant is computed from the equilibrium constant:

$$k_b\left(T_q\right) = \frac{k_f\left(T_q\right)}{K_{eq}\left(T_q\right)} \tag{31}$$

The equilibrium constant, in turn, is determined in the form of curve fits from Gibb's free energy (Eq. 35) [34]. It should be noted here that the backward reaction rate is generally not governed by the same temperature as the forward reaction rate, but is instead controlled by the translational-rotational temperature. The relation between the equilibrium constant based on the partial pressures and the Gibb's free energy is as follows [46]:

$$K_p\left(T\right) = \exp\left(-\Delta g^{p_{1\mathrm{atm}}}/\bar{R}T\right) \tag{32}$$

where,

$$\Delta g^{p_{1\mathrm{atm}}} = \sum_i \left(\nu_i' - \nu_i''\right) g^{p_{1\mathrm{atm}}}\left(T\right) \tag{33}$$

From which the equilibrium constant based on the concentrations can be computed as:

$$K_{eq}\left(T\right) = K_p\left(T\right) / \left(\bar{R}T/p_{1\mathrm{atm}}\right)^{\sum_i\left(\nu_i' - \nu_i''\right)} \tag{34}$$

The Gibb's free energy per unit mole can be computed at a specific temperature using an empirical curve fit [34]:

$$g^{p_{1\mathrm{atm}}}\left(T\right) = \bar{R}T\{A_1\left[1 - \ln T\right] - \frac{A_2 T}{2} - \frac{A_3 T^2}{6} - \frac{A_4 T^3}{12} - \frac{A_5 T^4}{20} - \frac{A_6}{T} - A_7\} \tag{35}$$

2.4 Relaxation Model

In the vibrational energy conservation equation, the source term accounts for two phenomena: the first is the energy exchange between the vibrational and the translational-rotational modes due to collisions, and the second is the vibrational energy change due to dissociation/recombination reactions.

As there are no definitive models to describe the latter phenomenon, the second term is determined based on the non-preferential model [30, 83], where the molecules are created or destroyed at the average vibration energy level.

$$\sum \dot{\omega}_s \hat{e}_{v,s} = \sum \dot{\omega}_s e_{v,s} \tag{36}$$

The energy exchange between the vibration and translation-rotation mode is modeled based on the Landau-Teller model, where the relaxation time in the first term is computed

using the molar-averaged correlation by Millikan and White. It is expressed as [30, 51]:

$$\langle \tau_s \rangle = \frac{\sum_{i=1}^{Ns} \chi_i}{\sum_{i=1}^{Ns} \chi_i / \tau_{si}} \tag{37}$$

where χ_i is the species mole-fraction. The inter-species relaxation time, τ_{si}, is modeled as:

$$\tau_{si} = \frac{\exp\left[A_{si}\left(T^{-1/3} - 0.015\mu_{si}^{1/4}\right) - 18.42\right]}{p/101325} \tag{38}$$

In this model,

$$\begin{aligned} A_{si} &= 1.16 \times 10^{-3} \mu_{si}^{1/2} \theta_{v,s}^{4/3} \\ \mu_{si} &= \frac{M_s M_i}{M_s + M_i} \end{aligned} \tag{39}$$

For temperatures above 8,000 K, Park's high temperature correction is adopted as [73, 51]:

$$\tau_s^{\text{Park}} = \frac{1}{(\sigma_s \bar{c}_s' n_s)} \tag{40}$$

Here, n_s is the number density of species s, $\bar{c}_s'$ is the average molecular velocity of that species and σ_s is the effective cross-section for collisions. The latter two properties are computed as:

$$\begin{aligned} \bar{c}_s' &= \left(\frac{8kT}{\pi M_s}\right)^{1/2} \\ \sigma_s &= 10^{21}\left(50000/T^2\right) \end{aligned} \tag{41}$$

The total relaxation time is the sum total of the molar-averaged relaxation time and Park's correction. At high temperatures, vibrational relaxation obeys a diffusion-like model with respect to vibrational energy levels [30]. Lee implemented Park's appropriate modification which takes the form [51]:

$$\frac{1}{\langle \tau_v^c \rangle} = \frac{1}{\langle \tau_v \rangle} \left| \frac{T_{sh} - T_v}{T_{sh} - T_{v,sh}} \right|^{s'-1} \tag{42}$$

where,

$$s' = 3.5 \exp\left(-5000/T_{sh}\right) \tag{43}$$

In this correction, T_{sh} and $T_{v,sh}$ are the translational-rotational and vibrational temperatures at the point on the shock where relaxation is initiated.

CHAPTER III

NUMERICAL FORMULATION

The numerical methodology used to compute the model equations that represent the physics and chemistry of hypersonic flows are presented here. The explanations are within the context of the unstructured Cartesian grid solver, NASCART-GT.

3.1 Vector Formulation

The conservation equations presented in the previous chapter are rearranged in the vector form to distinguish the inviscid and viscous terms, as well as the source terms. Identifying these is crucial since each term is treated differently (the spatial and temporal integration of inviscid, viscous and source terms) in the flow solver. The resulting set of equations can be represented as [51, 84]:

$$\frac{\partial \mathbf{U}}{\partial t} + \frac{\partial \left(\mathbf{F} - \mathbf{F_v}\right)}{\partial x} + \frac{\partial \left(\mathbf{G} - \mathbf{G_v}\right)}{\partial y} + \frac{\partial \left(\mathbf{H} - \mathbf{H_v}\right)}{\partial z} = \mathbf{S} \tag{44}$$

Here, $\mathbf{U}$ is the vector of conserved state variables, $\mathbf{F}$, $\mathbf{G}$ and $\mathbf{H}$ are the inviscid flux vectors along the Cartesian **X**-, **Y**- and **Z**- directions respectively, $\mathbf{F_v}$, $\mathbf{G_v}$ and $\mathbf{H_v}$ are their viscous counterparts, and $\mathbf{S}$ is the vector of source terms due to chemical reactions and thermal relaxation. Each of these vectors can be expanded as:

$$\mathbf{U} = \left[\begin{array}{ccccccccc} \rho & \rho u & \rho v & \rho w & \rho e & \rho_1 & \dots & \rho_{N_s} & \rho e_v \end{array} \right]^{\mathrm{T}} \tag{45}$$

$$\mathbf{S} = \left[\begin{array}{ccccccccc} 0 & 0 & 0 & 0 & 0 & \dot{\omega}_s & \dots & \dot{\omega}_{N_s} & \dot{\omega}_v \end{array} \right]^{\mathrm{T}} \tag{46}$$

where the superscript $^{\mathrm{T}}$ refers to the transpose of each matrix. The flux vectors can be expressed as (terms along the **X**- direction alone are presented in this section; a complete listing along all three Cartesian axes is given in the appendix A):

$$\mathbf{F} = \begin{bmatrix} \rho u \\ \rho u^2 + p \\ \rho v u \\ \rho w u \\ \rho\left(e+p\right)u \\ \rho_1 u \\ \vdots \\ \rho_{N_s} u \\ \rho e_v u \end{bmatrix} \qquad \mathbf{F_v} = \begin{bmatrix} 0 \\ \tau_{xx} \\ \tau_{xy} \\ \tau_{xz} \\ \tau_{xx}u + \tau_{xy}v + \tau_{xz}w - \left(q_{TR,x} + q_{V,x}\right) - \sum \rho_s h_s u_{D,s} \\ \rho_1 u_{D,1} \\ \vdots \\ \rho_{N_s} u_{D,N_s} \\ -q_{v,x} - \sum \rho_s e_v u_{D,s} \end{bmatrix}$$

3.2 Numerical Scheme

Adequate representation of the physical and chemical process using appropriate models alone is not sufficient in developing an effective numerical solver to compute hypersonic flows. Appropriate techniques to counter the numerical stiffness and other associated problems with computing such complex phenomena have to be taken into consideration.

The following sections in this chapter explain the numerical techniques implemented in NASCART-GT for the time integration of the conservation equations to compute hypersonic flows with a multitude of physical/chemical phenomena.

3.2.1 Spatial Discretization: AUSMPW+ Scheme

In a control volume, shock waves and boundary layers are generally regions where gradients of the flow properties are high. At hypersonic Mach numbers, the magnitudes of these gradients become even more protracted due to the strengths of the shock waves and the severity of the viscous dissipation in the boundary layers. Solving the conservation equations in such regions can lead to numerically stiff problems resulting in non-physical flow property calculations and instabilities. For accurate calculations in stiff regions, numerical dissipation has to be reduced, which in turn can lead to numerical instabilities adversely affecting the efficiency of the solver. Non-physical oscillations therefore adversely affect the overall robustness of the solver. Additionally, the presence of the chemical source term can further

affect the stiffness of the computation. Therefore, a spatial discretization methodology that can ensure high levels of accuracy, robustness and efficiency is essential for computing hypersonic flows.

The significant feature of upwind-biased numerical schemes is that the discretization of the equations on a grid conforms to the direction of propagation of information on that grid [94]. Thereby, critical aspects of the physical phenomena are automatically incorporated into the discretization scheme. There are essentially two methods of identifying the upwind directions, namely the flux vector splitting (FVS) approach and the flux difference splitting (FDS) approach. FVS formulations are generally more suited to be used in implicit schemes where the steady state of the flow is the desired outcome of the simulation. However, the simplicity of FVS schemes results in poorer resolution of discontinuities when compared to FDS schemes. The rationale behind FDS formulations is to take advantage of the solution of the local Riemann problem, which results in more accurate solutions. Such a scheme is better suited for explicit upwind formulations.

Roe's Riemann solver [81] is the most popular amongst FDS schemes due to its efficiency and accuracy. However, around expansion fans, numerical instabilities significantly affect the quality of the solutions, more so for hypersonic test cases because of the extremely high velocities associated with such flows. Additionally, this scheme has been known to show evidences of the carbuncle phenomenon. Liou and Steffen [53] introduced the AUSM (Advection Upwind Splitting Method) scheme as a robust alternative to the Roe's solver, with appropriately defined cell-face advection Mach numbers to determine the upwind extrapolation for convective quantities. With this, the AUSM scheme resolved shear layers much better than Roe's scheme, and was more suited to be used in computing hypersonic flows. Kim et al. [48] improved this scheme by introducing pressure weighted functions to avoid numerical oscillations near the wall and prediction overshoots behind shockwaves. This was further enhanced by Kim et al. [47] to be applied to hypersonic flows. With a new definition of the numerical speed of sound at cell interfaces, oblique shocks were better defined, avoiding non-physical expansion fans in the computations.

Lee [51] implemented the AUSMPW+ spatial discretization scheme in NASCART-GT

for the calculation of the inviscid fluxes, while extending the solver to compute inviscid flows in thermochemical nonequilibrium. Details of the implementation are given below. For the sake of simplicity, the flux computation along the **X**- direction alone is presented here.

While computing the flux terms in Eq. (44) using AUSMPW+, the inviscid flux terms at the cell interface take the following form [47]:

$$F_{\frac{1}{2}} = \bar{M}_L^+ c_{\frac{1}{2}} \mathbf{\Phi}_L + \bar{M}_R^- c_{\frac{1}{2}} \mathbf{\Phi}_R + \left(P_L^+|_\alpha \left[\mathbf{P}_L\right] + P_R^-|_\alpha \left[\mathbf{P}_L\right] \right) \tag{47}$$

where, for $m_{1/2} \geq 0$

$$\begin{aligned} \bar{M}_L^+ &= M_L^+ + M_R^- \left[(1-\omega_p)\left(1+f_R\right) - f_L \right] \\ \bar{M}_R^- &= M_R^- \omega_p \left(1+f_R\right) \end{aligned} \tag{48}$$

and for $m_{1/2} \leq 0$

$$\begin{aligned} \bar{M}_L^+ &= M_L^+ \omega_p \left(1+f_L\right) \\ \bar{M}_R^- &= M_R^- + M_L^+ \left[(1-\omega_p)\left(1+f_L\right) - f_R \right] \end{aligned} \tag{49}$$

Here, $m_{1/2}$ is the Mach number at the cell interface given by:

$$m_{1/2} = M_L^+ + M_R^- \tag{50}$$

Also,

$$\omega_p \left(p_L, p_R\right) = 1 - \min\left(\frac{p_L}{p_R}, \frac{p_R}{p_L} \right)^3 \tag{51}$$

and

$$f_{L,R} = \begin{cases} \left(\frac{p_{L,R}}{p_s} - 1 \right) \min\left[1, \frac{\min\left(p_{1,L}, p_{1,R}, p_{2,L}, p_{2,R}\right)}{\min\left(p_L, p_R\right)} \right]^2, & p_s \neq 0 \\ 0, & p_s = 0 \end{cases} \tag{52}$$

In the above expression, p_s is defined as follows:

$$p_s = P_L^+ p_L + P_R^- p_R \tag{53}$$

Also,

$$\begin{aligned} \mathbf{\Phi} &= \left[\rho, \rho u, \rho v, \rho w, \rho h, \rho_1, \ldots, \rho_{N_s}, \rho e_V\right]^T \\ \mathbf{P} &= \left[0, p, 0, 0, 0, 0, \ldots, 0, 0\right]^T \end{aligned} \tag{54}$$

Function ω_p varies as the cube of the pressure ratio and is small in most regions of the computational domain except around high pressure gradient regions like shocks. The Mach number and the pressure splitting function in the AUSMPW+ scheme at the cell interface are given by:

$$M^{\pm} = \begin{cases} \pm\frac{1}{4}\left(M \pm 1\right)^2, & |M| \leq 1 \\ \frac{1}{2}\left(M \pm |M|\right), & |M| > 1 \end{cases} \tag{55}$$

and

$$P^{\pm}|_{\alpha} = \begin{cases} \pm\frac{1}{4}\left(M \pm 1\right)^2\left(2 \mp M\right) \pm \alpha M\left(M^2-1\right)^2, & |M| \leq 1 \\ \frac{1}{2}\left(1 \pm \mathrm{sign}\left(M\right)\right), & |M| > 1 \end{cases} \tag{56}$$

with α ranging from 0 to 3/16. At 0, the scheme is more robust with the pressure splitting function being more diffusive, and at 3/16 the scheme becomes more accurate. The Mach number on each side is defined as:

$$M_{L,R} = \frac{U_{L,R}}{c_{\frac{1}{2}}} \tag{57}$$

The critical speed of sound at the cell interface is given below:

$$c_{\frac{1}{2}} = \begin{cases} c_s'^2 / \max\left(|u_L|, c_s'\right), & \frac{1}{2}\left(u_L + u_R\right) > 0 \\ c_s'^2 / \max\left(|u_R|, c_s'\right), & \frac{1}{2}\left(u_L + u_R\right) < 0 \end{cases} \tag{58}$$

Here,

$$c_s' = \left(2h_{\mathrm{normal}} \frac{\left(\tilde{\gamma}_L - 1\right)/\left(\tilde{\gamma}_L u_R\right) - \left(\tilde{\gamma}_R - 1\right)/\left(\tilde{\gamma}_R u_L\right)}{\left(\tilde{\gamma}_R + 1\right)/\left(\tilde{\gamma}_R u_R\right) - \left(\tilde{\gamma}_L + 1\right)/\left(\tilde{\gamma}_L u_L\right)}\right)^{0.5} \tag{59}$$

In the above expression, for chemically reacting flows in thermal nonequilibrium:

$$\tilde{\gamma} = 1 + \frac{p}{\rho e} \tag{60}$$

and the average sensible total enthalpy, h_{normal} is given by:

$$h_{\mathrm{normal}} = \frac{\left(h_{\mathrm{sensible},L} + \frac{1}{2}u_L^2 + h_{\mathrm{sensible},R} + \frac{1}{2}u_R^2\right)}{2} \tag{61}$$

3.2.2 MUSCL Extrapolation

For upwind schemes, the first spatial derivative of a property can be approximated to a first order discretization using a 2-point stencil; a 3-point stencil is required for second order accuracy. In FDS schemes, higher order approximations are determined based on the flux

values at the cell faces. In the original FDS schemes, the state vectors were assumed to be a constant throughout the grid cells. This assumption was sufficient for first order accurate discretizations [92]. Van Leer extended this by assuming that the state variables have a gradient from the cell center to the faces of each cell [99]. This strategy led to higher order extrapolations of the fluxes and state variables to the cell boundaries.

Such an implementation for data reconstruction at the cell faces (MUSCL: Monotone Upstream-centered Schemes for Conservation Laws) is combined with the AUSMPW+ scheme in NASCART-GT for higher order inviscid fluxes. The expressions for extrapolating the cell centered values to the cell faces are given below:

$$
\begin{aligned}
W^L_{i+1/2,j,k} &= W_{i,j,k} + \\
&\frac{\varepsilon_{i,j,k}\Delta x_{i,j,k}}{2}\left[(1-\kappa)\,\frac{W_{i,j,k}-W_{i-1,j,k}}{\Delta x_{i,j,k}+\Delta x_{i-1,j,k}} + (1+\kappa)\,\frac{W_{i+1,j,k}-W_{i,j,k}}{\Delta x_{i+1,j,k}+\Delta x_{i,j,k}}\right] \\
W^R_{i+1/2,j,k} &= W_{i+1,j,k} - \\
&\frac{\varepsilon_{i,j,k}\Delta x_{i+1,j,k}}{2}\left[(1+\kappa)\,\frac{W_{i+1,j,k}-W_{i,j,k}}{\Delta x_{i+1,j,k}+\Delta x_{i,j,k}} + (1-\kappa)\,\frac{W_{i+2,j,k}-W_{i+1,j,k}}{\Delta x_{i+2,j,k}+\Delta x_{i+1,j,k}}\right]
\end{aligned}
\tag{62}
$$

where,

$$
W = [\rho, u, v, w, h, c_1, \ldots, c_{N_s}, e_V]^T \tag{63}
$$

Depending the values of $\varepsilon_{i,j,k}$ and κ, different spatial orders of accuracies can be achieved at the cell faces. The combinations are presented in Table 1.

Table 1: Coefficients for MUSCL extrapolation

$\varepsilon_{i,j,k}$	κ	Order of accuracy
0	-	First-order piecewise constant
1	-1	Second-order fully upwind biased
1	0	Second-order upwind biased
1	1	Second-order central-differenced
1	1/3	Third-order upwind biased

It should be noted here that at the cell faces, viscous fluxes are calculated using a standard second order central difference scheme [50].

3.2.3 Flux Limiter

To ensure the stability during the progress of the simulations and to avoid non-physical overshoots, monotonicity of the scheme is maintained by using a limiter in the MUSCL extrapolation that becomes effective in regions of large gradients in density, total internal energy, total enthalpy, species concentrations and the energy associated with the vibrational mode [50]. This limiter reduces the order of accuracy of the MUSCL extrapolation when the magnitude of the difference in the flux terms from the cell center to the cell face is found to be greater than a threshold (ϕ_{lim}). For example, at the $i + 1/2$ face, the formulation looks like:

$$\varepsilon_{i+1/2,j,k} = \min\left[\varepsilon_{i,j,k}, \max\left(1 - \frac{\Delta\phi_{\max}}{\phi_{\text{lim}}}, 0\right)\right] \tag{64}$$

where,

$$\begin{aligned}\Delta\phi_{\max} = \max\Big[&\Big\{\max\left(\phi_{L_{i+1/2,j,k}}, \phi_{R_{i+1/2,j,k}}\right) - \max\left(\phi_{i,j,k}, \phi_{i+1,j,k}\right)\Big\}, \\ &\Big\{\min\left(\phi_{L_{i+1/2,j,k}}, \phi_{R_{i+1/2,j,k}}\right) - \min\left(\phi_{i,j,k}, \phi_{i+1,j,k}\right)\Big\}, 0\Big]\end{aligned} \tag{65}$$

and

$$\phi_{\text{lim}} = \text{osslimit} \times \min\left(\phi_{i,j,k}, \phi_{i+1,j,k}\right) \tag{66}$$

"osslimit" controls the level of dissipation of the limiter. The smaller its value, the more dissipative the limiter is. In other words, it limits the magnitude of any new maxima or minima created by the MUSCL extrapolation to the left or the right face. Here, ϕ represents ρ, e, h_o, χ_s and e_v.

This combination of the AUSMPW+ scheme for spatial discretization in tandem with MUSCL extrapolation, as well as the flux limiter installed in NASCART-GT, have been shown to make very good predictions of the inviscid hypersonic flows when compared with both experiments as well as other body-fitted mesh flow solvers [51]. Therefore, it has been naturally extended to compute viscous flows in thermochemical nonequilibrium by the addition of diffusion terms and transport coefficients based on the chemistry of the gas.

3.2.4 Temporal Discretization

3.2.4.1 Explicit 2-stage Hancock Scheme

To provide reasonably efficient and time-accurate solutions of the governing equations, NASCART-GT employs Hancock's two-stage (dual time-stepping) explicit scheme that has been tested and validated for various flow conditions [50, 51]. This explicit scheme comprises of predictor-corrector stages during time integration shown here:

$$\text{Stage 1, Predictor:} \quad \mathbf{U}^{n+1/2}_{i,j,k} = \mathbf{U}^{n}_{i,j,k} - \frac{1}{2}\frac{\Delta t^{n}_{i,j,k}}{V_{i,j,k}}\mathbf{R}^{n}_{i,j,k} \tag{67}$$

$$\text{Stage 2, Corrector:} \quad \mathbf{U}^{n+1}_{i,j,k} = \mathbf{U}^{n}_{i,j,k} - \frac{\Delta t^{n}_{i,j,k}}{V_{i,j,k}}\mathbf{R}^{n+1/2}_{i,j,k} \tag{68}$$

where,

$$\mathbf{R}^{n}_{i,j,k} = \{\mathbf{F}^{n}_{i-1/2,j,k} - \mathbf{F}^{n}_{i+1/2,j,k}\} + \{\mathbf{G}^{n}_{i-1/2,j,k} - \mathbf{G}^{n}_{i+1/2,j,k}\} + \{\mathbf{H}^{n}_{i-1/2,j,k} - \mathbf{H}^{n}_{i+1/2,j,k}\} - \mathbf{S}^{n}_{i,j,k} \tag{69}$$

This explicit solver has been used in a multitude of test cases that include sub- and supersonic viscous flows, as well as inviscid hypersonic thermochemical nonequilibrium flows. In all these cases, to adequately capture the gradients in the flow field, the minimum cell sizes in the computational domain were not required to be very small, which in turn allowed for much larger time steps during time integration (based on the stability criterion for explicit schemes). Therefore, the associated costs in their computation were within reasonable limits.

For hypersonic viscous flows, on the other hand, realistic freestream Reynolds numbers result in very thin boundary layers, requiring extremely small cells to capture the gradients here. With such cell sizes, the stability criterion for explicit schemes (controlled by the CFL number) results in prohibitively small time steps. This was indeed the case during the preliminary investigation where the Δt values were of the order of 10^{-12} seconds. To reach even a microsecond (10^{-6} seconds) in physical time, such simulations would be required to run for at least 10^{6} iterations! Clearly, the costs associated with such simulations

are extremely high and impractical. Therefore, alternative time integration schemes were considered for the test cases in this research study.

3.2.4.2 Implicit LU-SSOR Scheme

As an alternative to explicit schemes which require intractable number of iterations to compute viscous thermochemical nonequilibrium flows, implicit schemes can be used instead. In contrast to explicit formulations, the overall stability of the computations with implicit schemes can be maintained over a large range of Δt values, resulting in much less simulation time and cost [45].

A number of body-fitted mesh solvers have been using various implementations of implicit schemes to successfully compute viscous flows in thermochemical nonequilibrium [16, 105, 29]. Therefore, the natural step towards implementing that capability in an unstructured Cartesian grid framework would be to consider implicit schemes. Yoon and Jameson [109] developed an implicit formulation in the form of an efficient multigrid relaxation scheme for Newton iteration. The LU-SSOR (Lower Upper Successive Symmetric Over-Relaxation) scheme that they developed requires only scalar diagonal inversions, whereas Gauss-Seidel and other LU implicit schemes require block matrix inversions. This results in order-of-magnitude speedups, especially when considering hypersonic flows with finite-rate chemistry.

Klein [49] incorporated this scheme in NASCART-GT, and made preliminary comparisons of the relative speedups for frozen inviscid and viscous test cases with the explicit 2-stage Hancock scheme. The details of the implementation are given here. The following set of equations explain the formulation for frozen simulations. In NASCART-GT, the chemical source terms are computed using a point-implicit solver; therefore, they were excluded from the LU-SSOR formulation. Details regarding the extension to reacting flows will follow the perfect gas implementation details.

The LU-SSOR scheme is based on the linearization of the governing Navier-Stokes equations. Steger-Warming flux vector splitting [91] is applied to the Jacobian terms to avoid the inversion of a large block banded matrix, replacing it instead by forward and backward

relaxation sweeps through the computational domain. This scheme has been implemented in a manner such that time integration has been decoupled from the spatial discretization. Therefore, the explicit formulation of the viscous (2^{nd} order central differenced) and inviscid (Roe's, AUSMPW+, etc.) fluxes can still be utilized in computing the residuals required in the LU-SSOR formulation.

The finite-volume temporal and spatial discretization results in:

$$\mathbf{U}_{i,j,k}^{n+1} = \mathbf{U}_{i,j,k}^{n} - \frac{\Delta t_{i,j,k}^{n}}{V_{i,j,k}} \left[\beta \mathbf{R}_{i,j,k}^{n+1} + (1-\beta)\, \mathbf{R}_{i,j,k}^{n} \right] \tag{70}$$

where $\mathbf{R}$ is the residual at the (i, j, k) location. Depending on the values that β takes, this formulation can represent different schemes (Table 2):

Table 2: LU-SSOR formulations

β	Resulting formulation
0	Explicit time integration
0.5	Second-order semi-implicit time integration (Crank-Nicholson)
1	First-order fully-implicit time integration

Rearranging Eq. 70 and removing the (i, j, k) notation for simplicity, the time-marching form of the implicit upwind scheme can thus be written as [109, 33]:

$$V_{i,j,k} \left[\mathbf{I} + \beta \Delta t \{ \delta_x \mathbf{A} + \delta_y \mathbf{B} + \delta_z \mathbf{C} \} \right] \Delta \mathbf{U} = -\Delta t \mathbf{R}^{n} \tag{71}$$

where,

$$\mathbf{R}^{n} = \delta_x \mathbf{F} + \delta_y \mathbf{G} + \delta_z \mathbf{H} \tag{72}$$

The Jacobians in Eq. 71 are defined as:

$$\mathbf{A} = (\partial \mathbf{F} / \partial \mathbf{U})^{n} \quad \mathbf{B} = (\partial \mathbf{G} / \partial \mathbf{U})^{n} \quad \mathbf{C} = (\partial \mathbf{H} / \partial \mathbf{U})^{n} \tag{73}$$

$\Delta \mathbf{U} = \mathbf{U}^{n+1} - \mathbf{U}^{n}$ is the increment vector of the conservative variables for time step Δt. It should be emphasized here that the Jacobian terms consist of the inviscid terms alone in this formulation [42]. When Steger-Warming flux vector splitting is applied to the flux terms in this linearized equation, the unfactored system produces a large block banded

matrix which requires expensive matrix inversion computation. However, the system can be further simplified to obtain a matrix-free expression with significantly less computational cost. For this purpose, the split Jacobian matrix terms are approximated by their spectral radii. Here, $\mathbf{A}^{+}_{i,j,k}$, $\mathbf{A}^{-}_{i,j,k}$, $\mathbf{B}^{+}_{i,j,k}$, $\mathbf{B}^{-}_{i,j,k}$, $\mathbf{C}^{+}_{i,j,k}$ and $\mathbf{C}^{-}_{i,j,k}$ are constructed as follows:

$$\mathbf{A}^{\pm}_{i,j,k} = \frac{1}{2}\left[\mathbf{A}_{i,j,k} \pm \rho_{\mathbf{A}}\mathbf{I}\right] \implies \mathbf{A}^{+}_{i,j,k} - \mathbf{A}^{-}_{i,j,k} = \rho_{\mathbf{A}}\mathbf{I} \tag{74}$$

$$\mathbf{B}^{\pm}_{i,j,k} = \frac{1}{2}\left[\mathbf{B}_{i,j,k} \pm \rho_{\mathbf{B}}\mathbf{I}\right] \implies \mathbf{B}^{+}_{i,j,k} - \mathbf{B}^{-}_{i,j,k} = \rho_{\mathbf{B}}\mathbf{I} \tag{75}$$

$$\mathbf{C}^{\pm}_{i,j,k} = \frac{1}{2}\left[\mathbf{C}_{i,j,k} \pm \rho_{\mathbf{C}}\mathbf{I}\right] \implies \mathbf{C}^{+}_{i,j,k} - \mathbf{C}^{-}_{i,j,k} = \rho_{\mathbf{C}}\mathbf{I} \tag{76}$$

This ensures that the eigenvalues of the "+" matrices are non-negative and those of the "-" matrices are non-positive [109]. Here, $\rho_{\mathbf{A}}, \rho_{\mathbf{B}}, \rho_{\mathbf{C}}$ are the inviscid spectral radii of the Jacobians $\mathbf{A}$, $\mathbf{B}$ and $\mathbf{C}$. Substituting these approximations back into the Steger-Warming FVS form eliminates the need for matrix inversion. This is instead replaced with forward and backward relaxation sweeps, which account for the symmetric successive overrelaxation steps.

The LU-SSOR scheme can thus be summarized as:

$$\mathbf{L}_{LU}\mathbf{D}^{-1}_{LU}\mathbf{U}_{LU}\Delta\mathbf{U} = -\mathbf{R}^{n} \tag{77}$$

where,

$$\mathbf{L}_{LU} = \mathbf{D}_{LU} + \mathbf{L}^{*}_{LU} \quad \mathbf{U}_{LU} = \mathbf{D}_{LU} + \mathbf{U}^{*}_{LU} \quad \mathbf{D}_{LU} = \{\frac{1}{\Delta t} + \beta(\rho_{\mathrm{A}} + \rho_{\mathrm{B}} + \rho_{\mathrm{C}})\}\mathbf{I} \tag{78}$$

and

$$\mathbf{L}^{*}_{LU} = -\mathbf{A}^{+}_{i-1,j,k} - \mathbf{B}^{+}_{i,j-1,k} - \mathbf{C}^{+}_{i,j,k-1} \quad \mathbf{U}^{*}_{LU} = -\mathbf{A}^{-}_{i+1,j,k} - \mathbf{B}^{-}_{i,j+1,k} - \mathbf{C}^{-}_{i,j,k+1} \tag{79}$$

This solution procedure can be extended to viscous flow computations by incorporating the viscous Jacobians, which are approximated by their spectral radii as:

$$\rho^{v}_{\mathbf{A}} = \rho^{v}_{\mathbf{B}} = \rho^{v}_{\mathbf{C}} = \frac{\gamma}{\mathrm{Pr}}\frac{\mu}{\rho d} \tag{80}$$

where, γ is the ratio of the specific heats, Pr is the Prandtl number, μ is the molecular viscosity, ρ is the density and d is the distance between the centers of adjacent grid cells

[20, 18]. By using this approximation of the Jacobian of the viscous terms (using the viscous spectral radii), the diagonal form of the scheme is not disrupted.

This formulation of the LU-SSOR scheme does not include the source terms associated with reacting flows either. In NASCART-GT, Lee [51] installed a point-implicit chemistry solver to compute the chemical source terms for inviscid thermochemical nonequilibrium problems. With that already implemented, a novel strategy to compute viscous chemically reacting flows has been setup. Just as the spatial discretization and temporal integration are decoupled, so is the point implicit solver that computes the chemical source term. Thus, the solver calculates this term independently based on the state vectors at the previous time. Then, the LU-SSOR time integration procedure updates the rest of the state vectors, resulting in an efficient update of the flow properties. By not interfering with the LU-SSOR time integration, no additional computational cost is incurred. Of course, the state vectors in the viscous spectral radii are computed taking into account the thermochemical nonequilibrium in the flow. Thus, the chemically reacting nature of the flow field is preserved. The details of the point-implicit chemistry solver are given in the next section.

3.2.5 Point-Implicit Chemistry Solver

With the introduction of the chemical source term, a point-implicit methodology was implemented in NASCART-GT involving an $N_s \times N_s$ matrix inversion for each cell in the computational domain [51].

For each cell, the conservation equations can be represented in the following vector form:

$$\frac{\partial [\mathbf{U}]}{\partial t} V + \mathbf{R}(\mathbf{U}^n) = [\mathbf{S}]^{n+1} V \tag{81}$$

where, V is the cell volume and $\mathbf{R}$ is the sum total of the flux terms. Using the Taylor series to expand the species production term yields:

$$[\mathbf{S}]^{n+1} \approx [\mathbf{S}]^n + \frac{\partial [\mathbf{S}]^n}{\partial [\mathbf{U}]^n} \frac{d[\mathbf{U}]}{dt} \Delta t \tag{82}$$

Substituting and rearranging the conservation equation results in:

$$\left\{\mathbf{I} - \Delta t \frac{\partial [\mathbf{S}]^n}{\partial [\mathbf{U}]^n}\right\} \frac{d[\mathbf{U}]}{dt} V + \mathbf{R}(\mathbf{U}^n) = [\mathbf{S}]^n V \tag{83}$$

Using LU decomposition, the final time integration routine can be written in the following format:

$$\frac{d[\mathbf{U}]}{dt} V = \left\{\mathbf{I} - \Delta t \frac{\partial [\mathbf{S}]^n}{\partial [\mathbf{U}]^n}\right\}^{-1} \left\{ [\mathbf{S}]^n V - \mathbf{R}(\mathbf{U}^n) \right\} \tag{84}$$

3.2.6 Time Stepping Strategy

For the time integration of the governing equations, an appropriate time step must be considered based on the stability criterion of the scheme used. For the explicit 2-step Hancock scheme, Lee [50] extended the standard inviscid CFL number-based time-step criterion to account for the viscous terms. That formulation is given in Eq. 85.

$$\Delta t^n_{i,j,k} = \mathrm{CFL} \times \min \left\{ \begin{array}{l} \Delta x_{i,j,k} \left[(|u_{i,j,k}| + c_{i,j,k}) \left(1 + \frac{2}{\mathrm{Re}_{\Delta x}}\right)\right]^{-1}, \\ \Delta y_{i,j,k} \left[(|v_{i,j,k}| + c_{i,j,k}) \left(1 + \frac{2}{\mathrm{Re}_{\Delta y}}\right)\right]^{-1}, \\ \Delta z_{i,j,k} \left[(|w_{i,j,k}| + c_{i,j,k}) \left(1 + \frac{2}{\mathrm{Re}_{\Delta z}}\right)\right]^{-1} \end{array} \right\} \tag{85}$$

For the viscous hypersonic simulations, this time stepping strategy was found to be lacking due to the thermal effects being more restrictive than the viscous effects. The solution was found to be unstable even for very low CFL numbers. Therefore, an alternative time-stepping scheme was implemented, which was derived using a heuristic argument based on the relationship between the stability criteria in one- and multi-dimensions [80]:

$$\Delta t^n_{i,j,k} \leq \Delta x^2_{i,j,k} \left[\Delta x_{i,j,k} \left(|u_{i,j,k}| + |v_{i,j,k}| + |w_{i,j,k}| + c_{i,j,k}\sqrt{2} \right) + \frac{2\mu}{\mathrm{Re}\rho} \left(\frac{2\gamma}{\mathrm{Pr}} + \sqrt{\frac{2}{3}} \right) \right]^{-1} \tag{86}$$

This formulation was originally designed for an explicit scheme. However, it was also used for the implicit LU-SSOR scheme with much higher CFL numbers. The expression in Eq. 86 is a 3-D extended form of the 2-D formulation in Ref. [80].

3.3 Boundary Conditions

In NASCART-GT at the start of the simulation, freestream conditions are set throughout the computational domain. Starting with the first time iteration, the effects of the surface boundary conditions propagate throughout the domain until a steady state is reached. With this strategy, it is important to set appropriate inflow/outflow, as well as surface boundary conditions.

3.3.1 Inflow/Outflow BCs

Inflow and outflow boundary conditions in NASCART-GT are based on the characteristics of the flow solution. Information about the flow propagates along the characteristic directions, where the Riemann invariants remain constant. Table 3 lists the Riemann invariants and corresponding characteristics for a perfect gas simulation.

Table 3: Characteristics and Riemann invariants

Characteristics	Riemann invariants
$dx/dt\|_1 = u$	$R_1 = P/\rho^\gamma$
$dx/dt\|_2 = u$	$R_2 = v$
$dx/dt\|_3 = u$	$R_3 = w$
$dx/dt\|_4 = u + a$	$R_4 = u + 2a/(\gamma - 1)$
$dx/dt\|_5 = u - a$	$R_5 = u - 2a/(\gamma - 1)$

For subsonic flows, the variables R_1, R_2, R_3 and R_4 are propagated from the exterior and R_5 from the interior of the computational domain along the inflow boundary. Similarly, R_1, R_2, R_3 and R_4 are propagated from the interior and R_5 from the exterior of the domain along the outflow boundary. All flow variables are, therefore, calculated from the specified Riemann invariants along the inflow and outflow boundaries. For supersonic flow along the inflow boundary all 5 invariants are propagated from outside to inside of the domain, and from inside to outside of the domain along the outflow boundary.

For flows in thermochemical nonequilibrium, a simple extrapolation of the conserved state variables is done from the interior of the computational domain to the exterior.

3.3.2 Immersed Boundary Ghost Cell Approach

First, a note on the nomenclature used in this section is warranted. Cells in the flow domain that do no have surface panels intersecting them are considered "flow cells." Those that have panels slicing through them are termed "surface cells." The cells in the interior of the body that are used in the immersed boundary methodology are called "ghost cells."

The most significant difficulty in using Cartesian unstructured grids has to do with the definition of the surface of the immersed body. The fact that the volume mesh adjacent to the surface is usually not body-aligned makes it imperative to use special techniques to handle the cells that are sliced through by the surface panels. The treatment of these surface cells can vary depending on the methodology used to set or compute the state vectors at their cell centers/centroids, and how they are treated during the flux integration process.

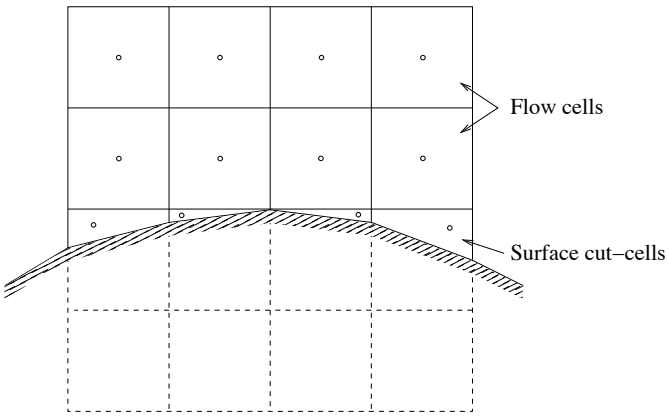

Figure 5: Schematic of cut-cell approach

In the cut-cell approach, cells generated by the intersection of the surface panels and the computational mesh result in trapezoidal shapes, as shown in Fig. 5. This method has been used extensively with varying levels of success in computing fluid flows under many different conditions [19, 98, 106, 37]. A common problem with this approach is the generation of very small cells due to the orientation and location of the surface panels with respect to the grid cells. Such tiny cells cause non-physical fluctuations in the flow variables near the body, in addition to increasing the stiffness of the problem. Additionally, depending on the shape of the geometry, cut-cell sizes could vary significantly along the surface, adding to the noise in

the surface property predictions. Besides, since cut-cell centroids are generally not aligned with the flow cell centers, the order of accuracy of the spatial discretization gets reduced during flux integration. One strategy to overcome these issues is by merging the tiny cut-cells with those that are adjacent to them, thereby reducing the stiffness of the equations. More recently, Berger and Aftosmis [7] have included a wall model to mitigate the effect of the mesh irregularities while using cut-cells, and have shown good predictions of skin friction and surface pressure distributions for turbulent flows. One important advantage of using the cut-cell approach is that the conservation laws at the wall are exactly satisfied.

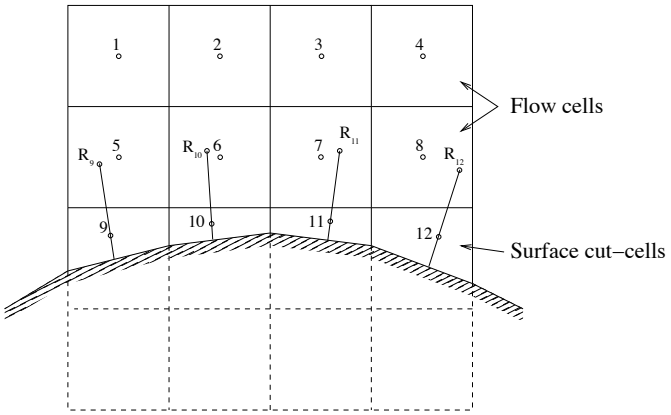

Figure 6: Schematic of embedded boundary method

An alternative method is the embedded boundary method where the surface cut-cells are removed from the flux integration formulation, thereby eliminating the stiffness problem that arises due to smallness of these cells. The flow properties at the centroid of the cut-cells are instead set based on reference points chosen in the flow domain from where the values are extrapolated [58, 59]. For example, in Fig. 6, the state vectors at the centroids of the cells numbered 9, 10, 11 and 12 are based on the properties at the reference points represented by R_9, R_{10}, R_{11} and R_{12}. The properties at the reference points are interpolated from the state vectors at the centers of the grid cells in which each reference point lies (cells 5, 6, 7 and 8, respectively), and the neighbors of these cells. Marshall implemented this methodology in NASCART-GT [57], and used it in the computation of Euler and Navier-Stokes equations. Since the flow properties are extrapolated to the centroid of the cut-cells, determining the

centroids added to the computational cost. Also, the non-alignment of these centroids with the flow cell centers still resulted in reducing the order of accuracy of flux integration near the wall. Additionally, this methodology does not explicitly guarantee the satisfaction of the conservation laws at the wall panels.

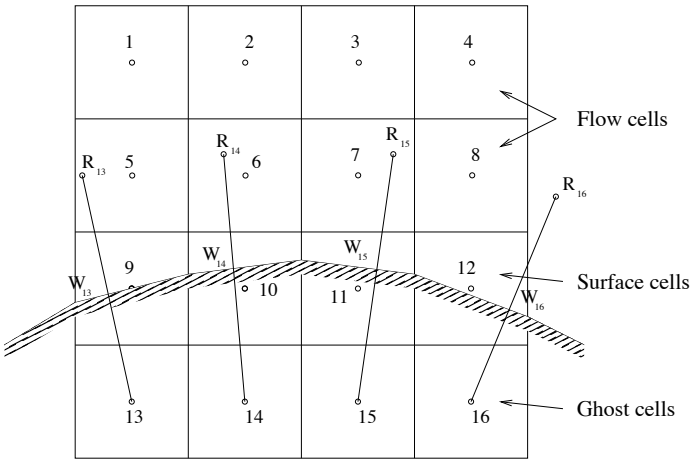

Figure 7: Schematic of immersed boundary ghost-cell approach

In the immersed boundary method, even though surface panels cut through the computational mesh, surface cells are retained in their entirety, which eliminates some of the problems faced in using the cut-cell or the embedded boundary approach (stiffness of the problem, orientation of centroid with respect to the flow cells). Flux integration is carried out at their cell centers just as they are for flow cells. Lee [50] implemented this ghost cell approach in NASCART-GT with specific emphasis on subsonic turbulent flows. This methodology is explained further in view of hypersonic applications.

Consider the flux integration stencil used in a Cartesian grid solver as shown in Fig. 8. To update the state vectors in cell number 6 for a 2^{nd} order accurate spatial integration scheme, the state vectors of 2 neighboring cells along each direction are needed to be known (cells 7, 8 along the positive **X** direction, 5, 23 along the negative **X** direction, 2, 34 along the positive **Y** direction and 10, 14 along the negative **Y** direction). Additionally for viscous flow simulations, cross derivative terms for shear stress calculations require the state vectors in cells numbered 3, 11, 1 and 9. This stencil represents the cells required in the flux integration scheme for a 2-D case; this can be easily extended to a 3-D flow calculation.

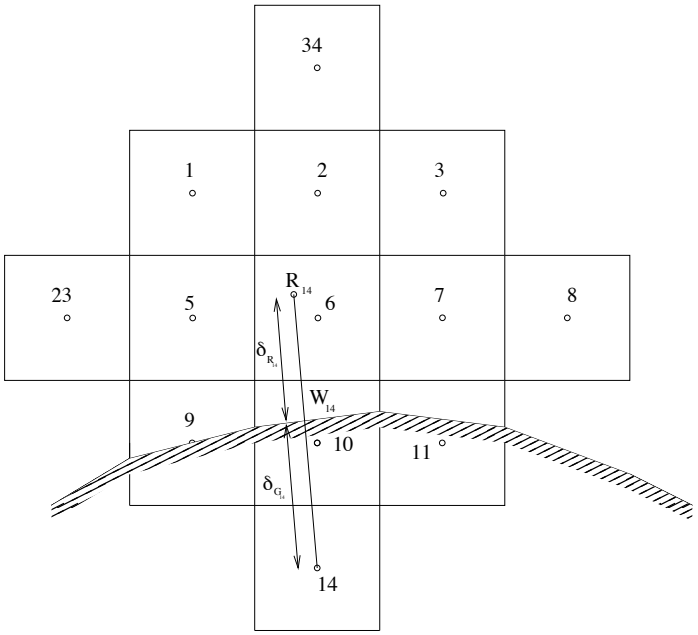

Figure 8: Viscous stencil: Immersed boundary ghost cell approach

In this stencil, cells numbered 7, 8, 5, 23, 2, 34, 3 and 1 are all flow cells and therefore have valid state properties assigned to their centers. Cells 11, 10 and 9 are surface cells that are included in the flux integration, and they as well have appropriate state vector values assigned to their cell centers. Cell number 14 on the other hand is completely inside the surface of the geometry and is turned off during flux integration. Therefore, appropriate state properties are required to be set there to complete the flux integration stencil. The methodology used to assign appropriate flow property values at the centers of such cells (ghost cells) forms the crux of the immersed boundary ghost cell approach.

To assign appropriate state values at the ghost cell, a "reference point" in the flow is identified; for cell number 14, the corresponding reference point is marked R_{14} in Fig. 7. Based on the state properties at this reference point and the known boundary conditions at the wall (W_{14}), values at the ghost cell are appropriately extrapolated.

Reference points in most cases do not coincide with the centers of flow or surface cells. Therefore, appropriate state vector properties are interpolated to these using a 2^{nd} order accurate distance-weighted least-square formulation. The location of the reference point is chosen along the wall normal direction from the ghost cell, and the distance ($\delta_{R_{14}}$) is set to

half the diagonal length of the surface cells. Previous investigations have shown that setting the reference points at a uniform distance from the surface yielded smoother variations of the surface properties compared to varying this parameter along the wall. For example, an alternative strategy to locate the reference points would be to use the distance between the ghost cell and the surface ($\delta_{G_{14}}$) as the same as the distance from the surface to the reference point ($\delta_{R_{14}}$). Depending on the curvature of the body, this can result in large variations in the reference cell distances along the surface, which can lead to large fluctuations in the interpolated reference cell properties. This adversely affects the ghost cell values, which impacts the flux integration of the surface cells.

Once the reference point location is decided, the cell within which it lies is identified, and its neighboring cells are determined. This strategy is similar to that followed in the embedded surface boundary condition. Using a 2^{nd} order accurate distance-weighted least-square formulation, the state vector at the reference point is interpolated using the values at the 3 closest cells that surround the reference point. In the stencil shown in Fig. 8, these would be cells numbered 6, 2 and 5. Thus, using the interpolated state properties at the reference point and the known boundary conditions at the wall, the values are extrapolated linearly to the ghost cell.

For the 1^{st} five governing equations (basic Navier-Stokes), the values of 5 different state properties are required to be known at the wall to completely define the state vector at the ghost cell. Depending on the type of flow being simulated, the wall values vary accordingly. Additionally, for flows in thermochemical nonequilibrium, information regarding the species concentrations and the vibrational energy/temperature are also required to completely define the state at the ghost cell.

For example, in viscous simulations the velocity of the fluid at the wall is uniformly zero throughout (no-slip BC); therefore, by using the interpolated values of the components of the fluid velocity at the reference point ($u^i_{R_{14}}$) and the no-slip boundary condition ($u^i_{W_{14}} = 0$), the 3 components of the velocity at the ghost cell (u^i_{14}) can be determined using a linear extrapolation formulation:

$$u^i_{14} = -\left(\frac{\delta_{G_{14}}}{\delta_{R_{14}}}\right) u^i_{R_{14}} \tag{87}$$

To set the pressure at the ghost cell, the normal momentum equation is considered across the wall. In the simulations presented in this thesis, a flat-wall boundary is assumed at the surface panels, and therefore the pressure gradient normal to the wall is taken to be zero; i.e. the pressure at the reference point and the ghost cell are taken to be the same:

$$P_{14} = P_{R_{14}} \tag{88}$$

Considering that the simulations presented here involve laminar boundary layers and that the surface cells that are used to resolve the boundary layers are small enough to capture the gradients well (resulting in very small distances between the reference point and the surface panels), this assumption conforms to that used in deriving the Blasius boundary layer equations, where the normal pressure gradient at the wall is considered to be zero.

For the temperature at the ghost cell, depending on the type of wall being simulated, the value at the ghost cell is set accordingly. For instance, if the wall is considered to be adiabatic, heat flux across the surface panels is zero. Thus, temperature at the ghost cell is set to the interpolated reference point temperature:

$$T_{14}^{\text{adiabatic}} = T_{R_{14}} \tag{89}$$

For the isothermal wall boundary condition, a linear extrapolation of the reference point and the wall temperatures is set at the ghost cell center:

$$T_{14}^{\text{isothermal}} = T_{W_{14}} + \left(\frac{\delta_{G_{14}}}{\delta_{R_{14}}}\right)(T_{W_{14}} - T_{R_{14}}) \tag{90}$$

Thus, with the extrapolated velocities, pressure and temperature at the ghost cell, the conserved state vector at this cell center is computed using perfect gas relations and the definitions of the momentum and total energy. For reacting cases, in addition to the aforementioned state variables, information regarding the species concentration gradients at the wall are also required. For the non-catalytic wall boundary condition that is being modeled in this research effort, these gradients across the surface are assumed to be zero as well. Therefore, the species mole fractions at the ghost cell center are set to the interpolated

reference point values:

$$\chi^s_{14} = \chi^s_{R_{14}} \tag{91}$$

Of course, for various catalytic wall boundary conditions, this assumption will fail, and the individual species mole fractions at the ghost cell center will have to be determined according the wall catalycity and the ghost cell temperature. In addition, the vibrational temperature is also extrapolated linearly from the reference point value to the ghost cell center.

$$T^{\text{isothermal}}_{v_{14}} = T_{W_{14}} + \left(\frac{\delta_{G_{14}}}{\delta_{R_{14}}}\right)(T_{W_{14}} - T_{vR_{14}}) \tag{92}$$

As for reacting cases, the state variables are computed taking into account the local species concentrations and the temperatures at the reference point and the ghost cell center. For example, to determine the density at the ghost cell, a pseudo-perfect gas relation is used where the gas constant is determined based on the local chemical composition of the gas.

A note on the temperature extrapolation for hypersonic flow conditions: While setting the temperature at the ghost cell center based on the values at the reference point and the wall temperature, additional checks had to be installed to ensure non-physical values were not being computed here. This was largely not seen in subsonic and supersonic cases where the temperatures in the boundary layer were not exceedingly high; but in hypersonic flow conditions where the boundary layers can reach very large magnitudes of temperatures, of the order of $\mathcal{O}(10,000\text{ K})$, the linear extrapolation can lead to negative temperatures being computed at the ghost cell centers. This is explained using an example here.

Suppose the simulated flow conditions result in a reference cell temperature of 2000 K ($T_{R_{14}}$ in Fig. 8) for an isothermal wall at 500 K ($T_{W_{14}}$); if the reference point and the ghost cell were equidistant from the surface ($\delta_{G_{14}} = \delta_{R_{14}}$), based on the linear extrapolation formulation, the temperature at the ghost cell center (T_{14}) would be computed to be -1500 K! To avoid such non-physical values here, NASCART-GT follows a clipping strategy that prevents this temperature from being set to values below a prescribed threshold limit. For example, if this limit was set to half the reference cell temperature ($T_{R_{14}}/2 = 1000$ K), then the ghost cell would be set to 1000 K (instead of -1500 K). Naturally, this would imply that the wall temperature which the fluid sees would not correspond to the value set during

the start of the simulation ($T_{W_{14}} = 500$ K). Such a shortfall is countered by the adaptive refinement strategy which includes the refinement of the surface cells. Again, assuming the same linear variation of the temperature across the wall, if the cell sizes were half of those used in above example, then the temperatures at the reference point ($T_{R_{14}}$) and the ghost cell (T_{14}) would be computed to be 1000 K and 0 K, respectively. By using the same clipping strategy, this would limit the ghost cell temperature and set it at 500 K (instead of 0 K). If the grid cells were refined to one additional refinement level, the reference point would have a temperature of 500 K, as would the the ghost cell (since $T_{W_{14}} = 500$ K). Since this a realistic value ($T_{14} = 500$ K), this temperature is not clipped and the immersed boundary method would reflect the exact temperature set during the start of the simulation.

During the preliminary investigations, a series of temperature clipping strategies were analyzed and the most stable of those was chosen for the cases presented in the results section. Comparisons of two such implementations are presented there. Additionally, alternative strategies for setting the ghost cell temperatures were also considered. These involved setting 2 different temperatures at the ghost cell, one for the inviscid flux calculation and the other for the viscous flux calculation. For the inviscid fluxes, as the temperature at the ghost cell hardly influences the terms here, this could correspond to an adiabatic wall setup ($T_{14} = T_{R_{14}}$). And for the viscous flux terms, since the gradient of the temperature alone is required in determining the heat flux terms here, this temperature could actually be set to a negative value (and the gradient would correspond to the actual wall temperature). Preliminary investigations into this strategy showed good predictions of the thermal boundary layer, but the noise associated with this implementation required a much more detailed research effort. This has been left as a future area of study in the immersed boundary ghost cell methodology.

3.4 Solution Adaption

The solution adaptive mesh refinement strategy used in NASCART-GT has been described by Tu [97], Marshall [57], Lee [50] and Lee [51]. In each of these references, strategies used to adapt the cells for specific flow conditions encountered are described. In a similar

manner, the refinement approach was adjusted for the viscous hypersonic flows, and the strategy followed is described here.

In each flow cell, the gradient of the velocity divergence, vorticity, pressure or the species mass fractions, represented by ϕ, is computed and scaled to the cell dimension as:

$$\tau_{\phi_{i,j,k}} = \phi \times l_{i,j,k}^{3/2} \tag{93}$$

where, l is the cube-root of the cell volume. The average root-mean-square of the gradient throughout the computational domain is then determined for the reference value as:

$$\sigma_\phi = \frac{1}{N} \sum_{i=1}^{N} \tau_\phi^2 \tag{94}$$

where, N is the total number of flow cells. Depending on whether the local gradient is less than or greater than the domain averaged threshold value for unrefinement and refinement, respectively, the cell is appropriately modified, i.e.

$$\begin{aligned} \tau_{\phi_{i,j,k}} &< \kappa_{\mathrm{U}} \times \sigma_\phi, \qquad \text{Unrefine} \\ \tau_{\phi_{i,j,k}} &> \kappa_{\mathrm{R}} \times \sigma_\phi, \qquad \text{Refine} \end{aligned} \tag{95}$$

where, κ_{U} and κ_{R} are the user-input threshold values for unrefinement and refinement. In addition to the existing solution adaption parameters, temperature and stagnation enthalpy gradients based refinement were introduced to capture the gradients in the stagnation region accurately. As the fluid comes to a standstill in this region, gradients of the previously listed properties failed to effect the refinement of coarse cells, severely impacting the stagnation point convective heating rate predictions. Including temperature and stagnation enthalpy based gradients in the adaptive refinement strategy resulted in a much better suited grid for computing heating rates. The impact of this implementation is explained further in the results section.

In addition to the existing adaptive mesh refinement strategy, which loops through the list of flow cells alone in the computational domain to evaluate gradients of one or more of the aforementioned list of parameters, refinement of the surface cells after the start of the simulation was included in the solver. Given the smallest cell size requirement to

make reasonable predictions of the surface quantities in hypersonic flow conditions, this implementation enabled the option of restarting converged coarse grid simulations with refinement turned on to include surface cells, and improve upon the already developed coarse grid solutions. This strategy dramatically improved the convergence rates of the simulations, which would have otherwise taken significantly longer periods of time to converge due to the excessive number of cells generated.

Two implementations of the surface cell refinement strategy were tested in the process. These are explained with the help of representative grids in Figs. 9-12. Figures 9 and 10 show the initial and final coarse grids that were used for a hypersonic inviscid flow test case. The first refinement strategy involved the surface cells and their neighbors alone in the computational domain, leaving the rest of the flow cells at lower refinement levels (coarser cells) (Fig. 11). The second setup included the surface cells in the regular solution adaption process, whereby all the cells in the computational domain would have their refinement levels increased at the same time (subject to the refinement thresholds) (Fig. 12). The former resulted in fewer cells in the computational domain, but ended up having significant refinement level differences between surface and flow cells over very short distances. The latter generated more number of cells, but there was a more systematic order in which the cell sizes dropped.

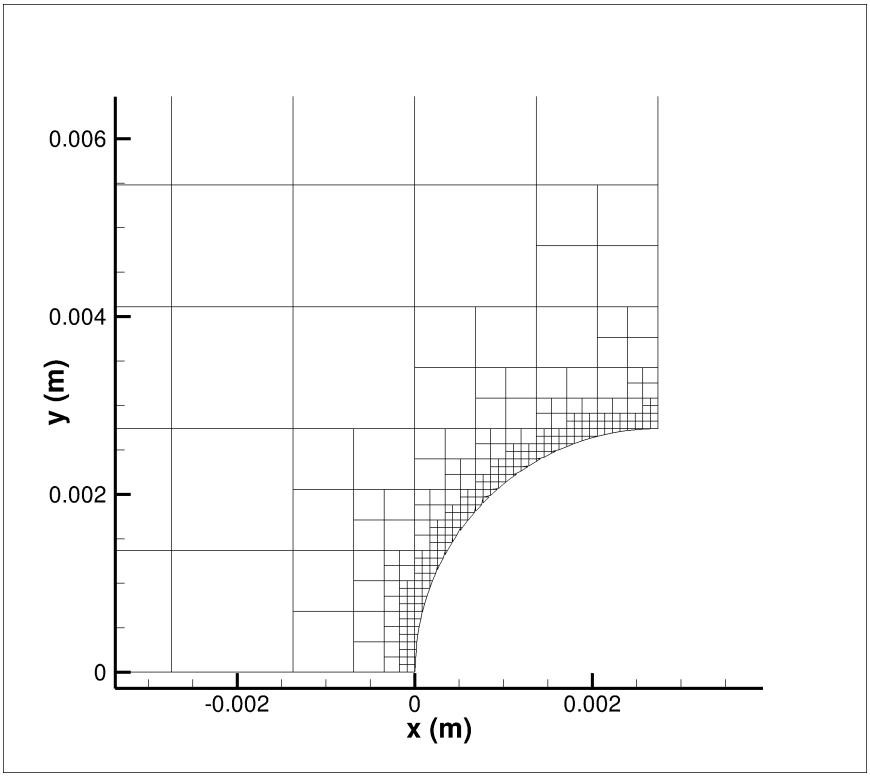

Figure 9: Solution adaption strategies: Initial coarse grid

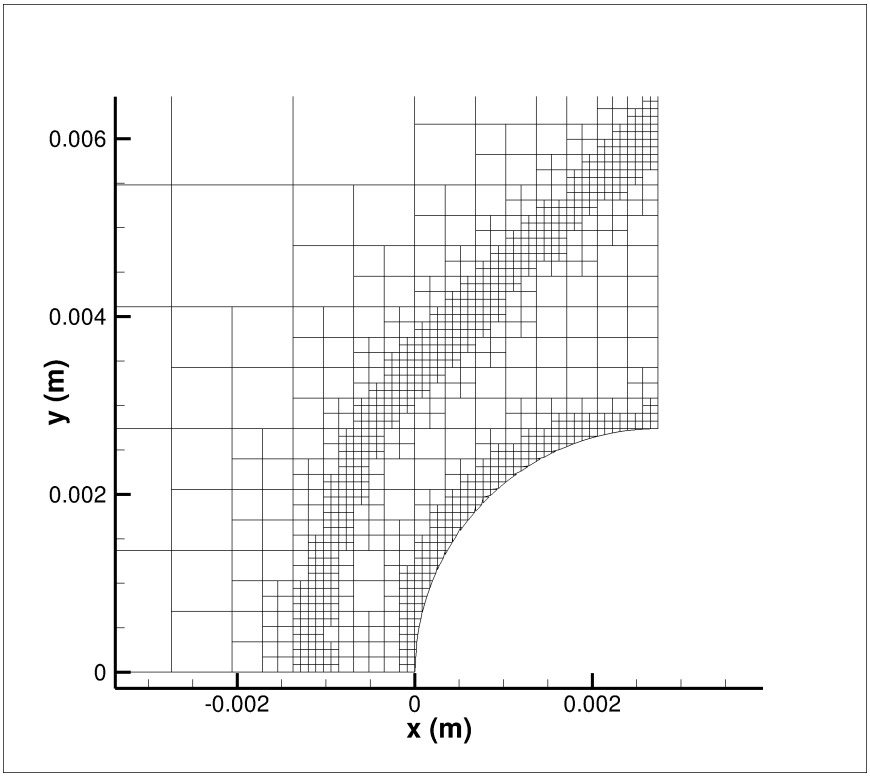

Figure 10: Solution adaption strategies: Converged coarse grid

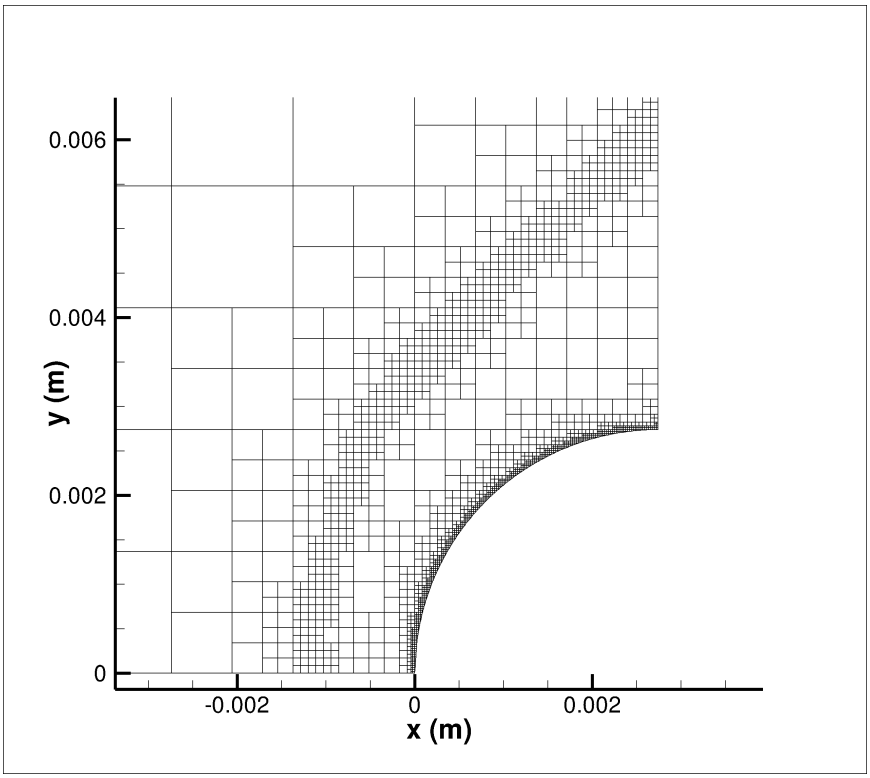

Figure 11: Solution adaption strategies: Surface cells refinement only

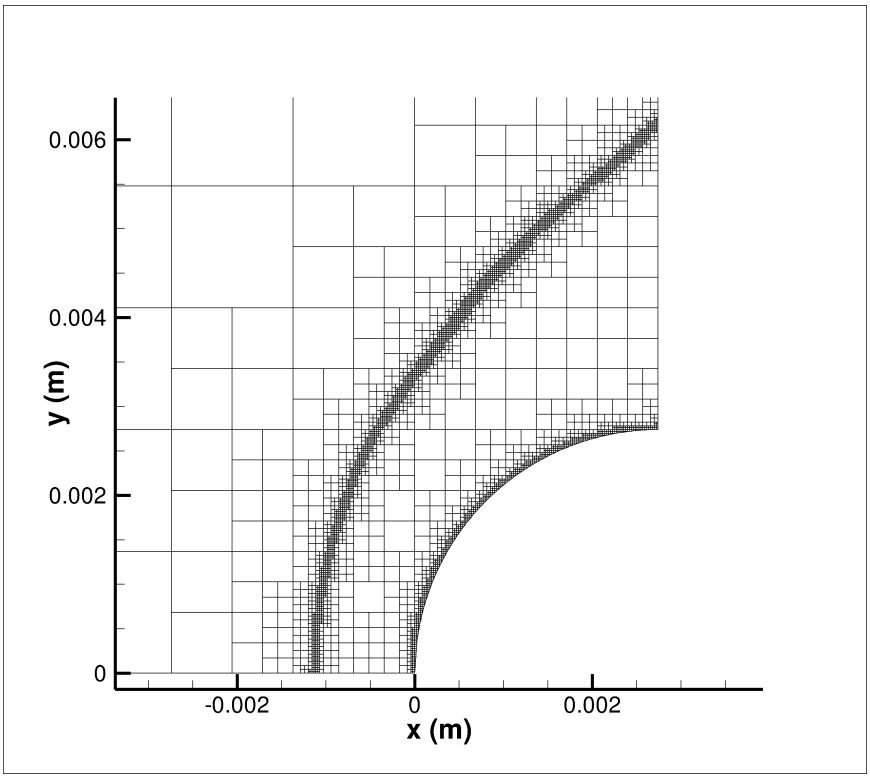

Figure 12: Solution adaption strategies: Solution adaption including surface cells

CHAPTER IV

FROZEN FLOW RESULTS - I

4.1 Introduction

The goal of predicting variations in the pressure, skin friction and convective heating rates at the surface for hypersonic flows is a challenging task given the complex physics and chemistry associated with such flows. The problems associated with computing the sharp gradients and the chemical source terms add to the difficulty, requiring adequate care in the choice of spatial and temporal discretization schemes. Using an unstructured Cartesian grid solver for making these estimates causes the problem to be all the more challenging because of the non body-aligned and shock-aligned nature of the computational grid cells. But given their inherent advantages in the ease of grid generation around complex geometries and adaptive mesh refinement capabilities, it is important to establish the strengths and shortcomings of using such a framework in computing complex flows. Such a heuristic study will not only serve as a benchmark for future calculations of similar flow conditions, but it will also aid in furthering the state-of-the-art in the field.

In the current investigation of the immersed boundary methods, a simple 2-D test case was first identified, and preliminary analysis of the workings of the framework were studied. Following that, more complex flows that involve interactions between shock waves and boundary layers were chosen to further evaluate the accuracy of the predicted surface properties, simultaneously emphasizing the inherent advantages of the solution adaptive capability of unstructured Cartesian grids. Each of these tests were conducted with frozen gas flows for the preliminary investigations. To further demonstrate the predictive capability of the solver, a range of hypersonic freestream Mach numbers were chosen for an axisymmetric test case, and the overall trend in the heating estimates were compared with empirical relations and experimental results. Finally, flow predictions for 2-D geometry in a thermochemical nonequilibrium environment with both adiabatic and isothermal wall boundary

conditions were made and compared with reference body-fitted grid results, confirming the effectiveness of using the immersed boundary ghost cell methodology in predicting convective heating for hypersonic flow conditions.

4.2 Frozen Flow Surface Prediction Comparisons

To evaluate the convective heating rate prediction capability using unstructured Cartesian grids at hypersonic Mach numbers, the choice of preliminary test cases should take into account the relative computational costs associated with the preparatory investigation. For instance, higher Reynolds number flows result in thinner boundary layers, which require extremely small surface cells for adequate resolution. This increases the total number of cells in the computational domain, adding significantly to the cost of the computations. Instead, flows with lower freestream Reynolds number can be used as preliminary test conditions, but here too care must be taken to ensure that the continuum hypothesis is not invalidated in the process. Since Kn $\propto$ M/Re, at the same Mach number, lower Reynolds numbers result in higher Knudsen numbers (more prone to rarefaction). Furthermore, reducing the freestream Mach number to ensure continuum is not an option, since that would defeat the purpose of the investigation (hypersonic heating predictability).

Lofthouse [54] identified a series of test conditions for comparing heat transfer predictions for Mach 10 and 25 flows past a cylinder (argon and nitrogen gases). Even though these tests were catered towards comparing predictions using a DSMC code (MONACO) and a Navier-Stokes solver (LeMANS), the conditions are ideal for this preliminary investigation of the surface pressure, skin friction and convective heating rate predictions. In that reference, the choice of the Reynolds and Knudsen numbers resulted in establishing the advantages and disadvantages of using molecular dynamics and/or continuum flow solver at various rarefied/continuum regimes.

From those cases, two were identified for the hypersonic flow tests past a cylinder of radius 12 in. (0.3048 m) using NASCART-GT. Mach 10 flow of argon gas was chosen, since argon, being an inert monatomic gas, would ensure the absence of thermochemical nonequilibrium phenomena in the flow. For each test case, the freestream Reynolds number

Table 4: Mach 10 argon flow conditions

Re_∞	Kn_∞	ρ_∞ [kg/m^3]	P_∞ [Pa]
289	0.050	5.636×10^{-6}	0.2346
1445	0.010	2.818×10^{-5}	1.1642

and density were appropriately set to analyze flow conditions at a constant freestream velocity ($\approx$ 2624 m/s). The cylinder wall was set at 500 K and the freestream was computed to be at 200 K. For these tests, the front half of the cylinder alone was considered to avoid the rarefied wake region, where the continuum assumption often fails. This also resulted in far fewer cells as the solution adaption feature of NASCART-GT otherwise tended to automatically generate excessive number of cells to resolve the vorticular structures in the wake. The freestream Reynolds numbers for the test cases were approximately 289 and 1445, and the corresponding Knudsen numbers were 0.050 and 0.010, respectively. The conditions are summarized in Table 4.

It should be pointed here that according to Ref. [54], continuum breakdown was observed for the Kn = 0.01 and 0.05 cases in regions within the shock wave and some portions of the boundary layer. Therefore, differences were observed between the predicted properties using the DSMC code and the Navier-Stokes solver in these regions. The plots of the variations of the Knudsen number in the domain from that reference are shown in Figs. 13 and 14.

For these flow conditions, grids of different specifications were used for each case. Simulations were started with initial coarse grids and run to convergence. In the process, solution adaption of these coarse grids was performed at specified intervals. The initial adaptive refinement strategy included the flow cells alone, keeping the smallest size of the cells the same. Once the coarse grid converged solution was reached, additional refinement cycles that included the surface cells in the adaption process were started. During each such refinement cycle, the smallest cell in the domain was split into 4 (2-D), reducing the minimum cell size by 50% each time. This resulted in the better resolution of the surface variations of the pressure, velocities and temperature.

Each test case was run using NASCART-GT's implicit LU-SSOR scheme, allowing for

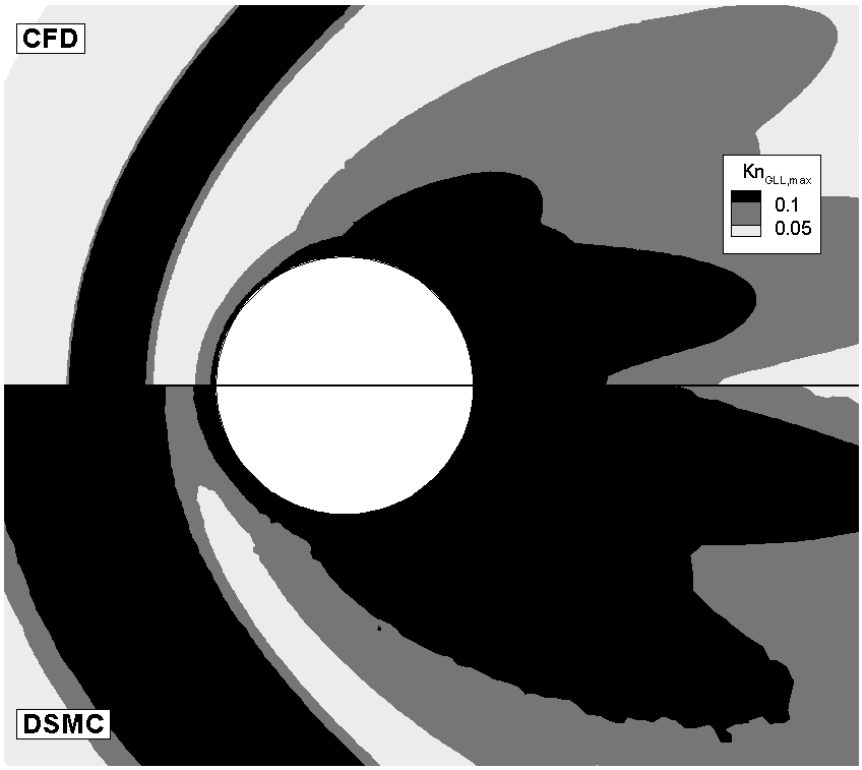

Figure 13: Kn around cylinder in Mach 10 argon: $\mathrm{Re}_\infty = 289$ [54]

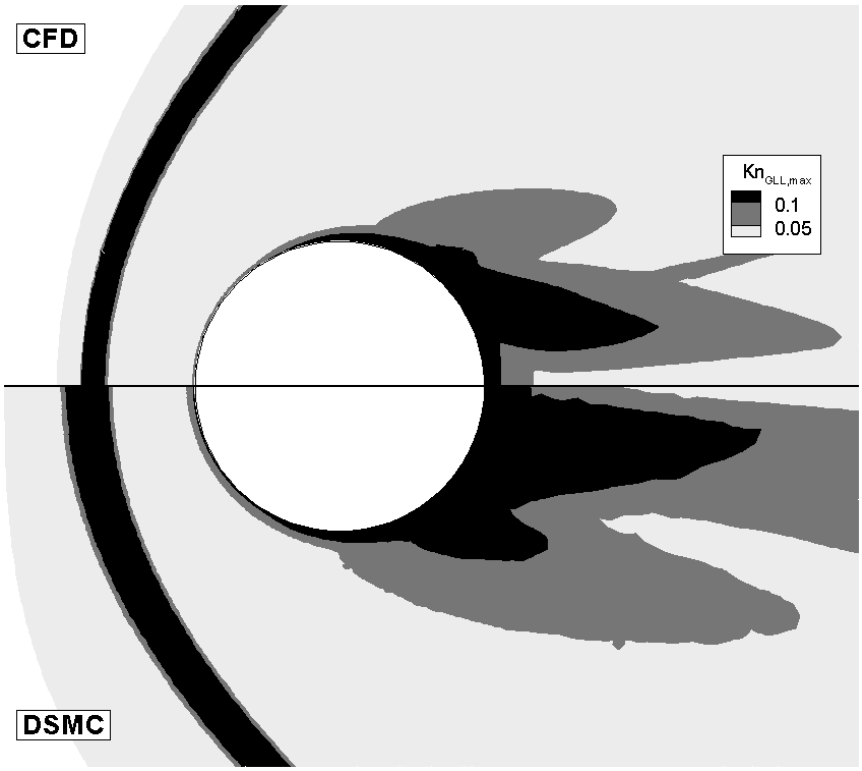

Figure 14: Kn around cylinder in Mach 10 argon: $\mathrm{Re}_\infty = 1445$ [54]

CFL numbers to be ramped up from 0.1 to 10,000. The inviscid fluxes were extrapolated to the faces to 2^{nd} order accuracy using the MUSCL scheme. "osslimit" in the flux limiter was set at 0.05. AUSMPW+ scheme was used to spatially discretize the inviscid fluxes, and the corresponding viscous terms were computed using a central difference scheme. For the temperature clipping strategy adopted in the immersed boundary ghost cell approach, the minimum limit for the ghost cell temperatures was set to half the reference cell temperatures. The results of these simulations are presented here.

4.2.1 Cylinder in Mach 10.0 Argon Flow

4.2.1.1 Re 289, Kn 0.05

Figures 15 and 16 are representative coarse and fine grids used for the Re 289 test case. At such a low Reynolds number, this case was dominated by viscosity resulting in a very thick boundary layer enveloping the cylinder. The advantage of using this setup was that reasonably coarse surface cells could be used to capture the gradients within the boundary layer. The drawback, on the other hand, was that these conditions meant that the flow was prone to rarefaction, especially at such high Mach numbers.

The coarse converged grid accounted for approximately 4,500 cells with the smallest cell size $\Delta x = 4.7 \times 10^{-3}$ m. The finest grid used for this freestream condition resulted in a total of approximately 7 million cells, with the corresponding smallest cell size $\Delta x = 7.4 \times 10^{-5}$ m. At such low Reynolds numbers where viscosity dominates the flow, the resulting shock wave and boundary layer were considerably thicker that those generally seen for higher Reynolds numbers. With smooth gradients in the flow properties across such larger areas, the resulting number of cells turned out to be quite large.

Contours of the Mach number, pressure and temperature gradients in the computational domain are presented in Figs. 17-22. As mentioned above, the gradients in the flow are very smooth given the magnitude of the freestream Reynolds number. The results show the evidence of a very thick bow shock wave and boundary layer, which the finer cells resolved better. Again, with the finer grids, the thermal boundary layer was resolved better and a cooler fluid was computed near the wall; thereby, the density in this region was seen to be

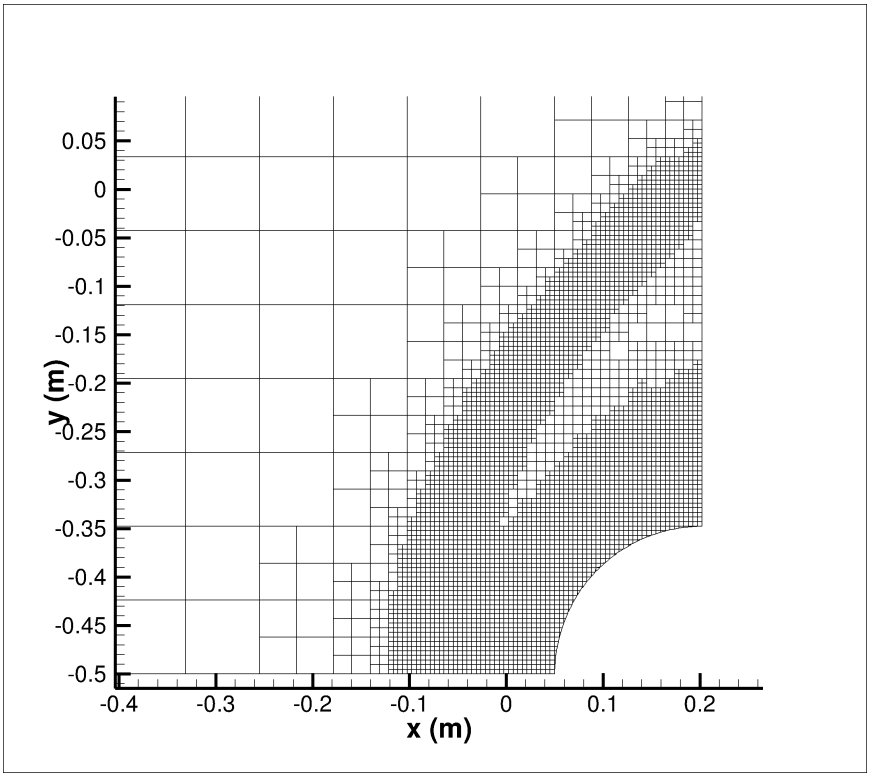

Figure 15: Mach 10, Re 289 flow: coarse grid

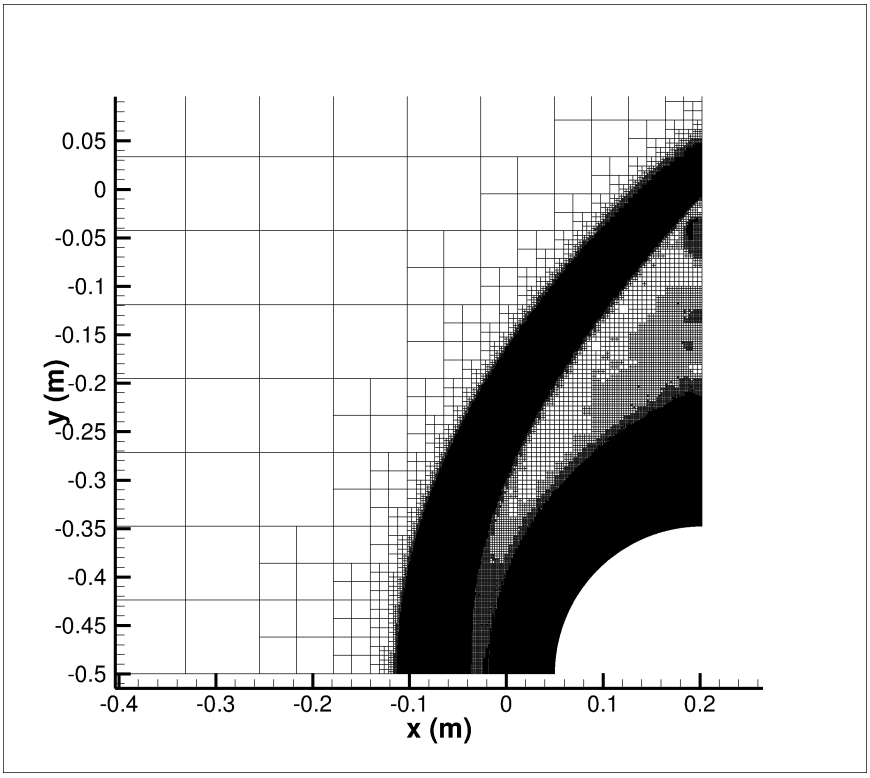

Figure 16: Mach 10, Re 289 flow: finer grid

higher, which marginally reduced the shock stand-off distance.

These results compare very well with those presented by Lofthouse [54]. The shock stand-off distances are very similar, and the peak temperature computed in the post-shock wave region are identical ($\approx$ 6500 K).

Predictions of the pressure coefficient, skin friction coefficient and the convective heat transfer rate are presented in Figs. 23-25. Results from the DSMC code (MONACO) and the reference Navier-Stokes solver with no-slip boundary conditions (LeMANS) are overlaid in these plots, to evaluate and analyze the trends of the surface property predictions. Each of these are plotted along the circumferential-angle direction. Each plot shows the results of the simulations using 3 representative grid cell sizes, to show the evidence of the progress of the solution trend as the surface cell refinement cycles kick in during the solution adaption routines in NASCART-GT.

The overall prediction of the pressure coefficient matches well with the reference computational results. C_p in the stagnation region is somewhat under-predicted for the finer grid cells, but the general trend of the variation matches perfectly with the other code predictions. The smoothness of the curves compare very well with reference variations, and is least sensitive to the non-body conforming nature of Cartesian unstructured grids.

The next 2 plots show the comparisons of the variations of shear stress (skin friction coefficient) and heat flux along the surface of the cylinder. It is evident that the predictions of NASCART-GT tend to be significantly noisier compared to the reference results, and even when compared to its own C_p predictions. Both the skin friction and the convective heat flux are computed based on the gradients of the velocities and temperature at the surface of the geometry, whereas C_p is computed using the absolute pressure value at the wall.

In the immersed boundary ghost cell approach, the normal gradient of the pressure at the wall is set to zero, whereas temperature and velocities have non-zero variations. For these non-zero gradients, the values set at the ghost cell center are dependent on the distances of the reference point and the ghost cell center from the wall panel. The reference point distance is held constant in these simulations, but the ghost cell center distance from the

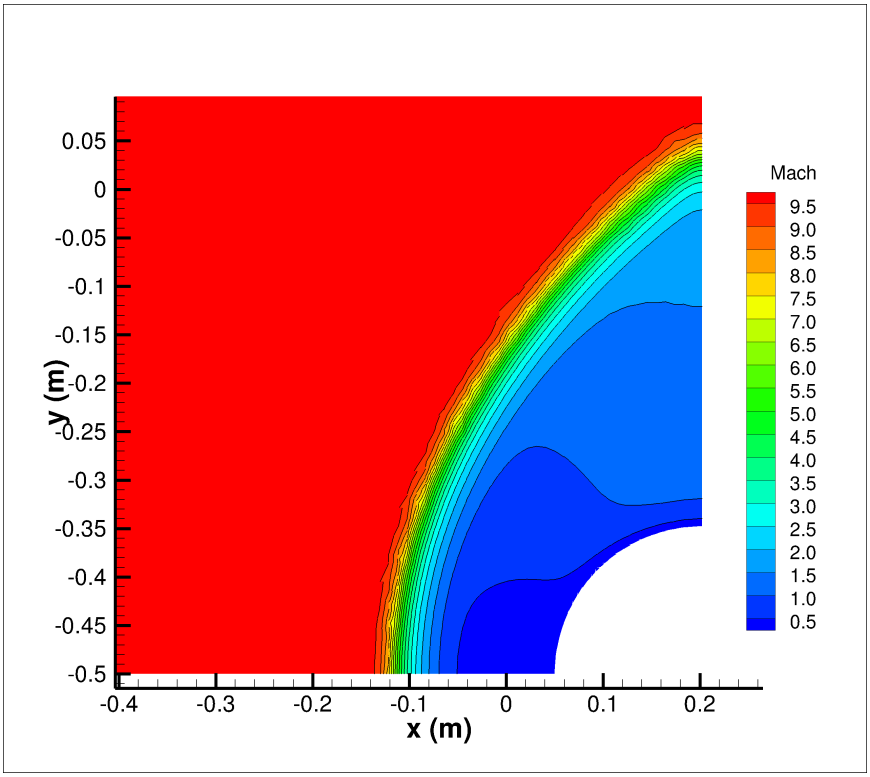

Figure 17: Mach 10, Re 289 flow: Mach contours: coarse grid

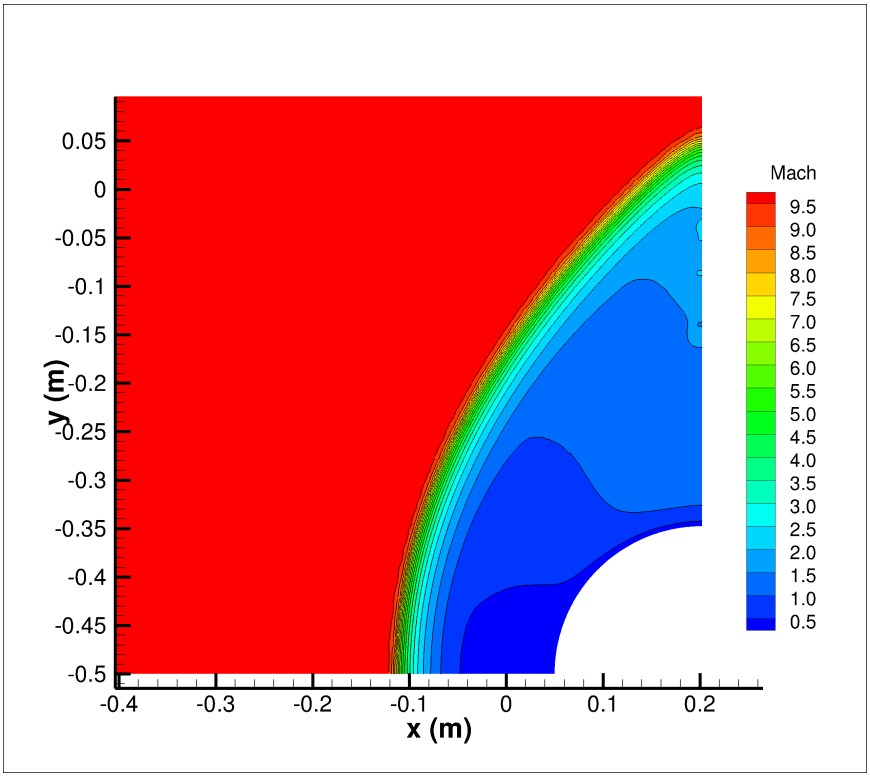

Figure 18: Mach 10, Re 289 flow: Mach contours: finer grid

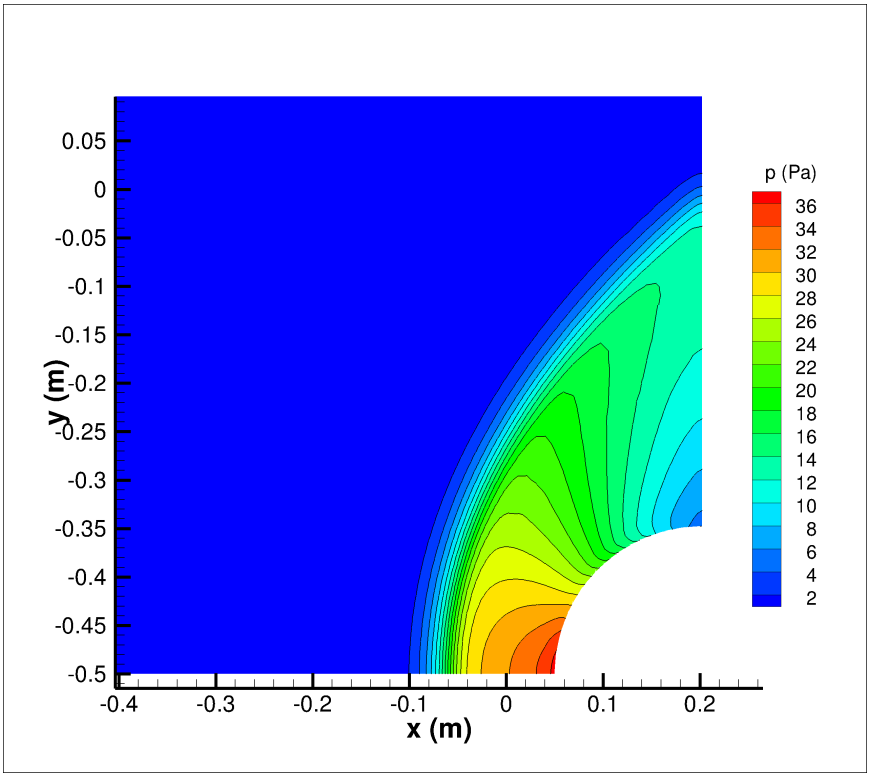

Figure 19: Mach 10, Re 289 flow: pressure contours: coarse grid

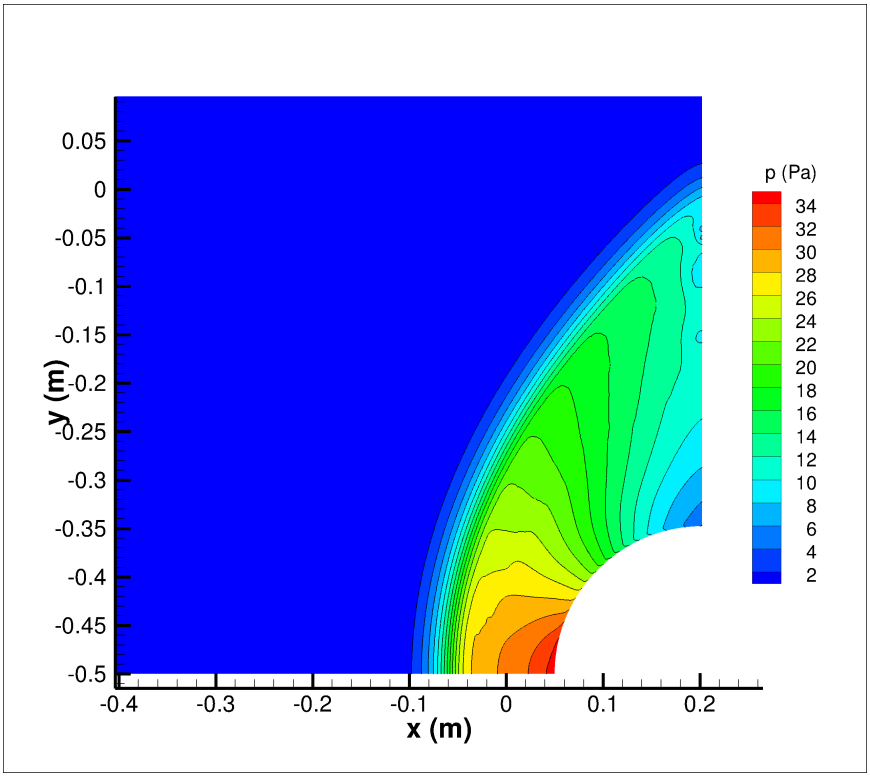

Figure 20: Mach 10, Re 289 flow: pressure contours: finer grid

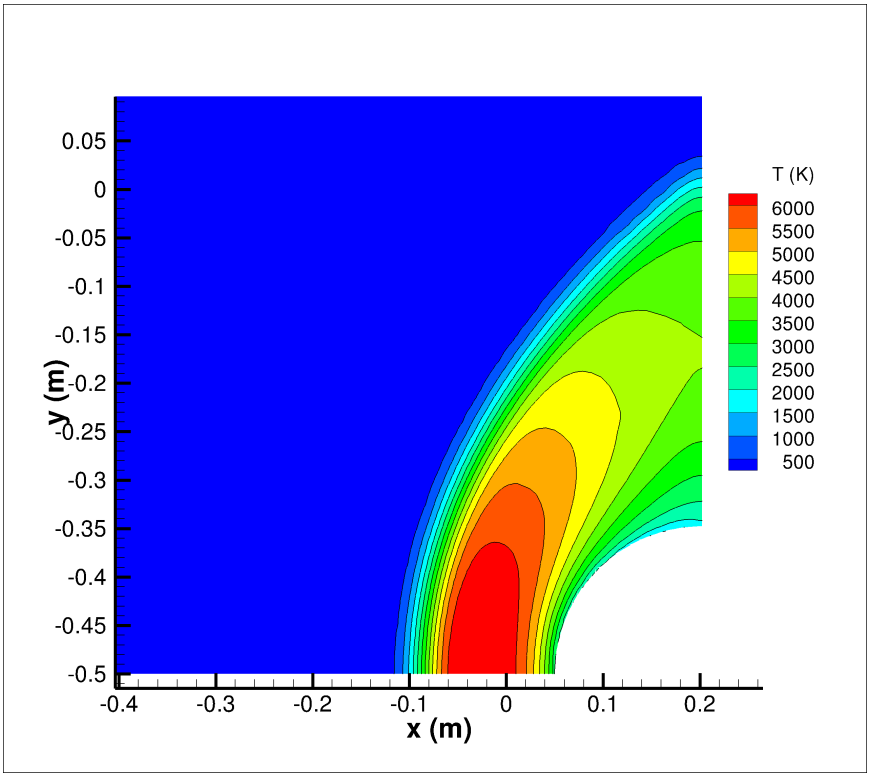

Figure 21: Mach 10, Re 289 flow: temperature contours: coarse grid

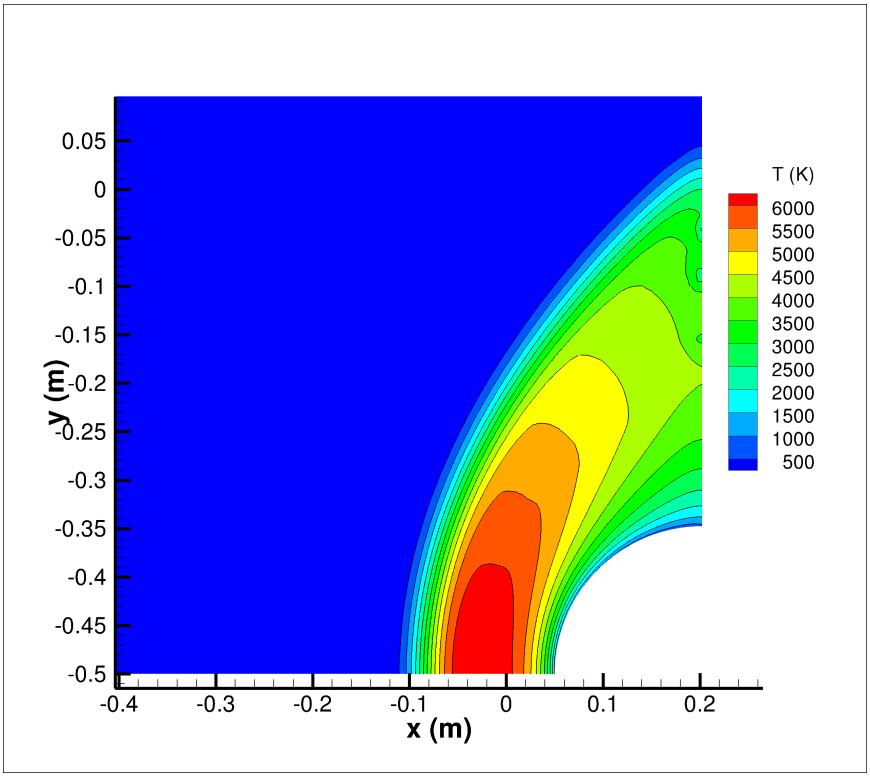

Figure 22: Mach 10, Re 289 flow: temperature contours: finer grid

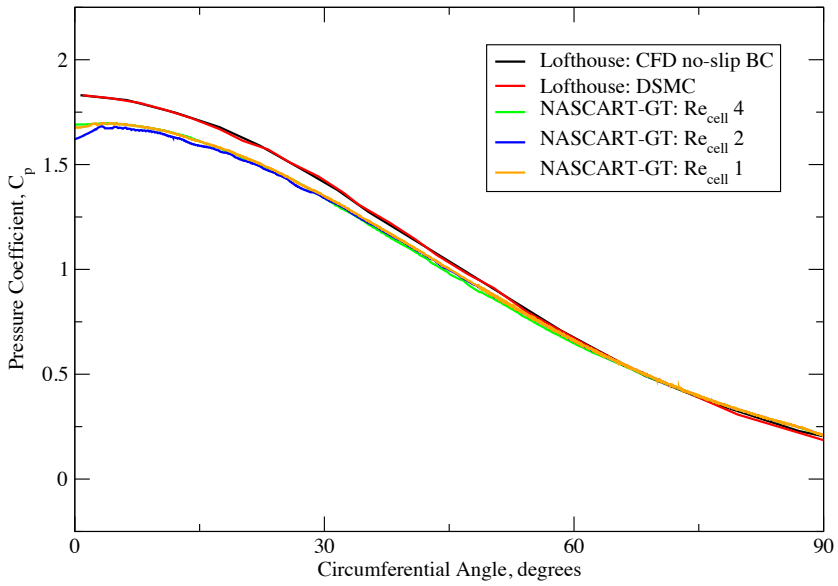

Figure 23: C_p distribution: Mach 10, Re 289

panel varies depending on how and where each panel cuts the Cartesian grid. This leads to some small fluctuations in the surface properties.

Further, interpolation at the reference point depends on the its distance to 3 closest surrounding cell centers. For curved surface, these distances can vary significantly, causing further fluctuations in the reference point values.

The noisiness in the C_f and $\dot{q}_w$ predictions is evidence of such issues facing the immersed boundary ghost cell approach. The magnitudes of the predictions, on the other hand, compare very well with the reference values, showing evidence of improvement as the surface cell size drops.

In the plots, the progression of the smallest cell size is presented in the form of the maximum Reynolds number based on the properties at the wall. This is defined as:

$$\mathrm{Re}_{\mathrm{wall}} = \rho_{\mathrm{wall}} \times a_{\mathrm{wall}} \times \Delta x_{\mathrm{wall}} / \mu_{\mathrm{wall}} \tag{96}$$

where, a_{wall} is the speed of sound at the wall temperature.

Previous studies [90, 6] have shown that this parameter plays a very important role in

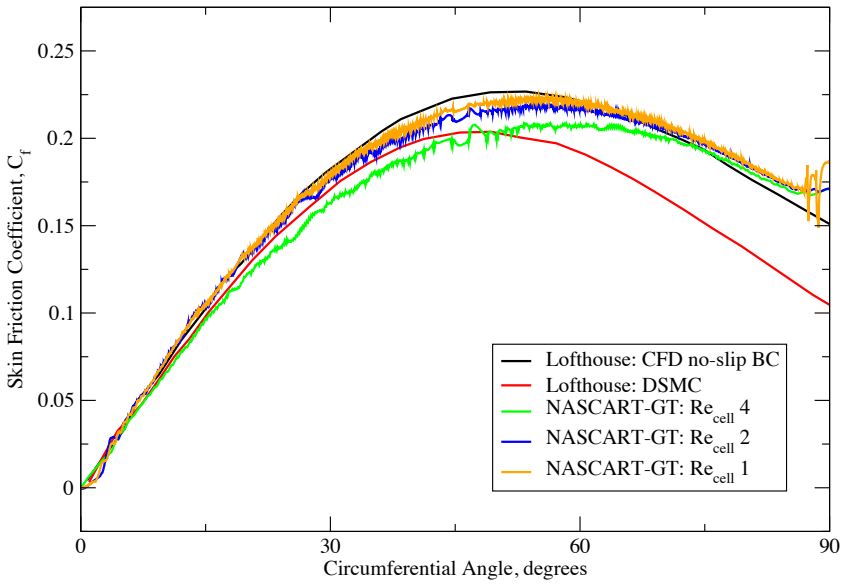

Figure 24: C_f distribution: Mach 10, Re 289

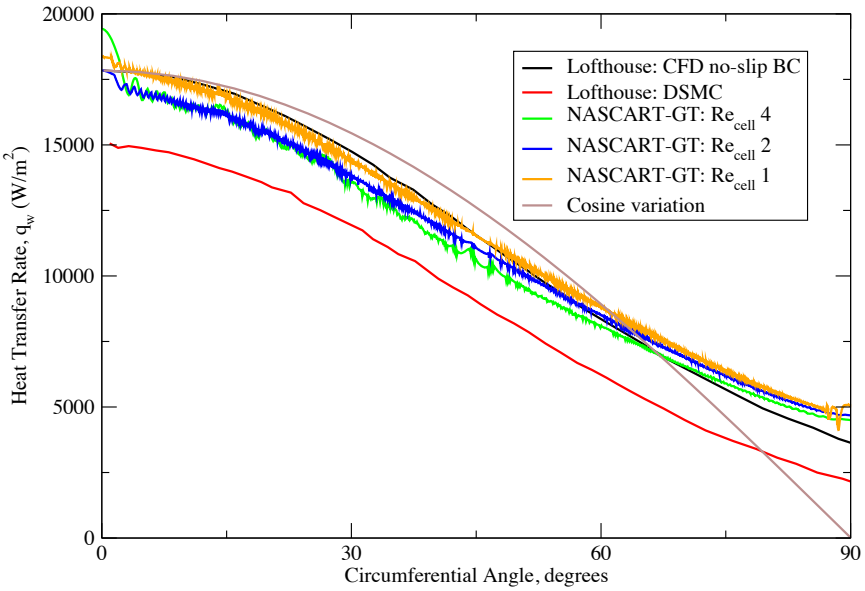

Figure 25: $\dot{q}_w$ distribution: Mach 10, Re 289

the accuracy of the surface gradients, in particular the convecting heating rate. As seen in the plots, the skin friction coefficient and the heat transfer rate tend to be more sensitive to the wall Reynolds number magnitude than the surface pressure variation. A very accurate definition of the velocity and thermal boundary layer is critical in the accurate prediction of the skin friction and the convective heat transfer, respectively. The impact of $\mathrm{Re}_{\mathrm{wall}}$ will be seen in more detail in the subsequent tests.

4.2.1.2 Re 1440, Kn 0.01

The next test case involved an intermediate Reynolds number of 1440, which is slightly higher than the previous setup; this resulted in a flow defined by a lower Knudsen number (0.01). Similar comparisons between simulations using the immersed boundary ghost cell framework of NASCART-GT were made with the results from LeMANS and MONACO [54]. At this higher Reynolds number, both the boundary layer and the shock wave thicknesses were significantly smaller than the previous test case as the effect of viscosity was being countered by the more forceful convection phenomena in the flow. The thinner boundary layer meant that smaller cells were required to accurately capture the temperature and velocity gradients here, once again resulting in a significantly large number of cells. Solutions were converged to on a coarse and fine grid using the solution adaption strategy explained earlier, as shown in Figs. 26 and 27, respectively. The coarse grid consisted of 7,400 cells, with the smallest size $\Delta x = 2.4 \times 10^{-3}$ m. The finest grid used in this test case consisted of 968,500 cells, with the minimum cell size being $\Delta x = 1.5 \times 10^{-4}$ m.

Similar to the previous case, the off-surface flow features were predicted very well by the Cartesian grid solver, with the finer grid simulation naturally capturing the gradients more effectively. The peak temperature once again compares very well with the reference values, as do the shock shape and stand-off distance. Similar contour plots of the Mach number, pressure and temperature variations are shown in Figs. 28-33.

The pressure distribution along the surface compares very well with the reference, falling on top of both the DSMC and the CFD solver predictions for the entire range of surface cell sizes. The skin friction and the heat transfer rates, on the other hand, show significant

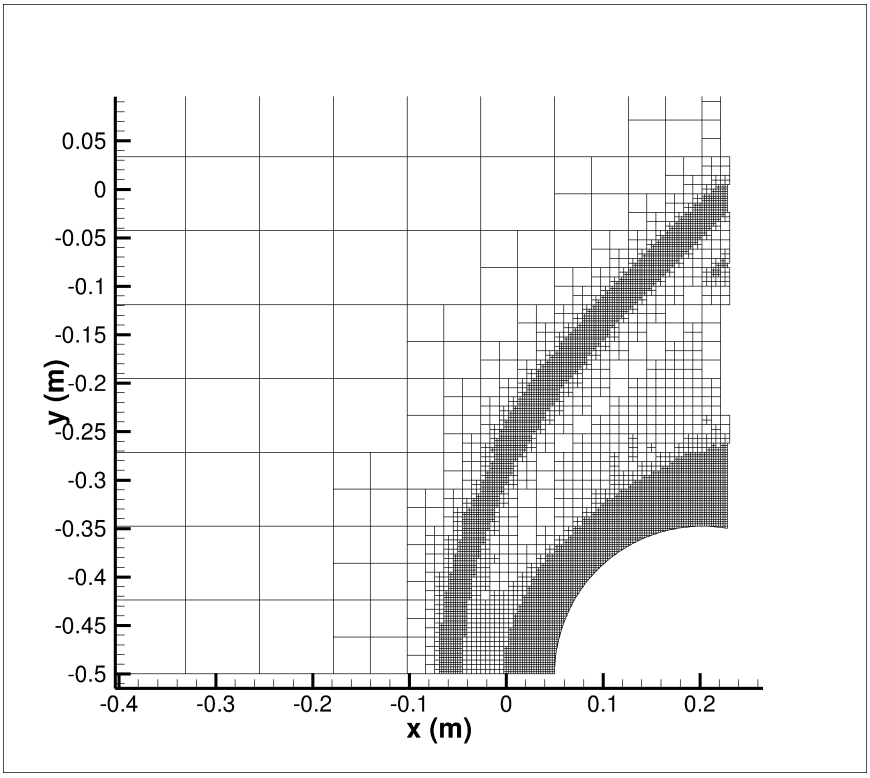

Figure 26: Mach 10, Re 1445 flow: coarse grid

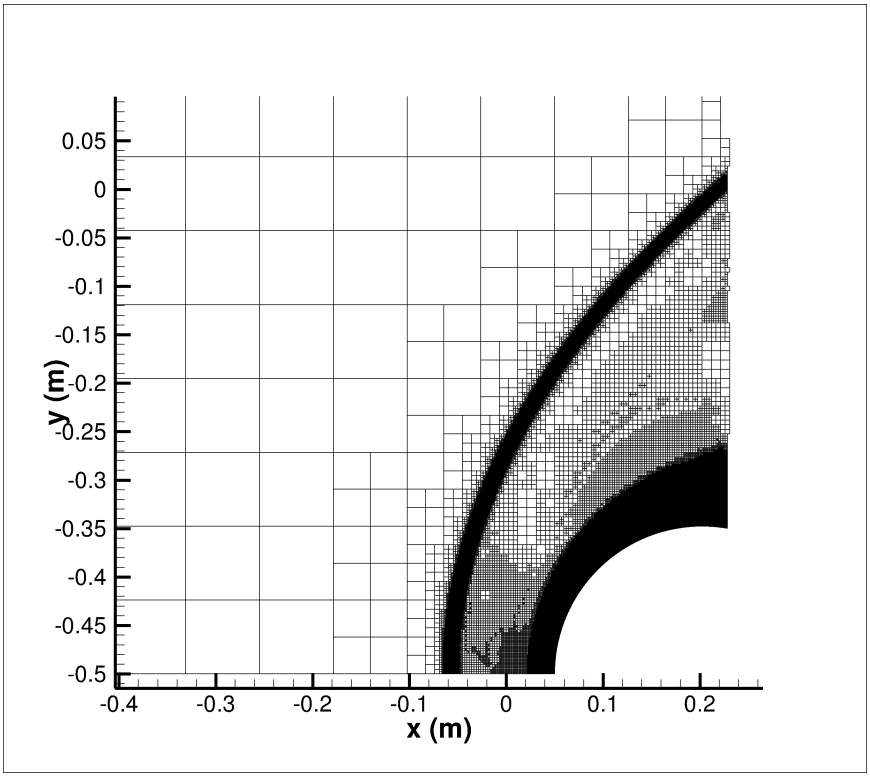

Figure 27: Mach 10, Re 1445 flow: finer grid

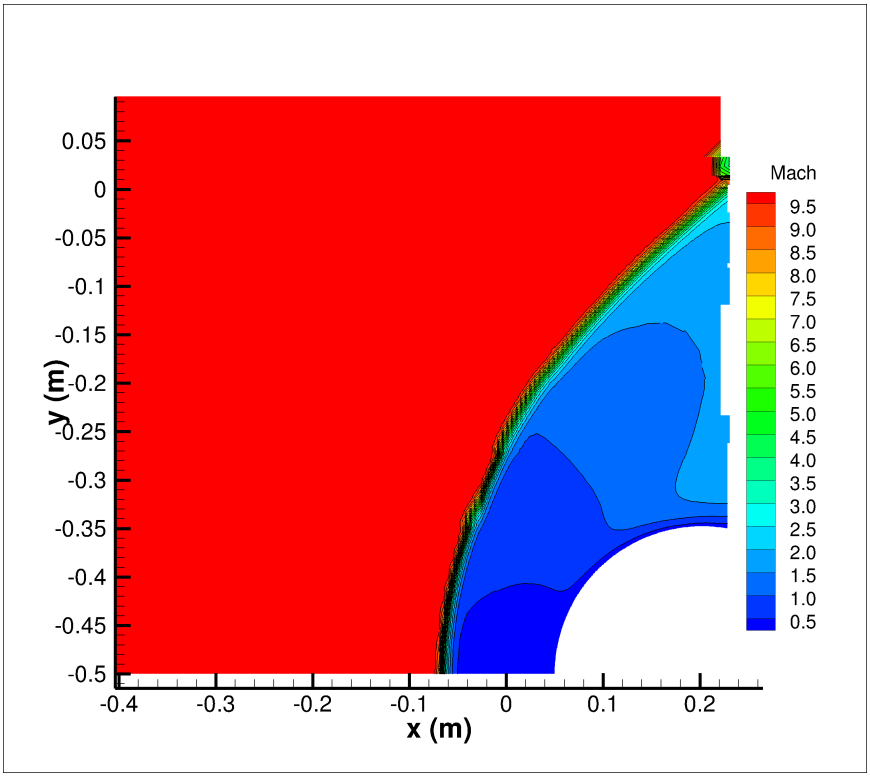

Figure 28: Mach 10, Re 1445 flow: Mach contours: coarse grid

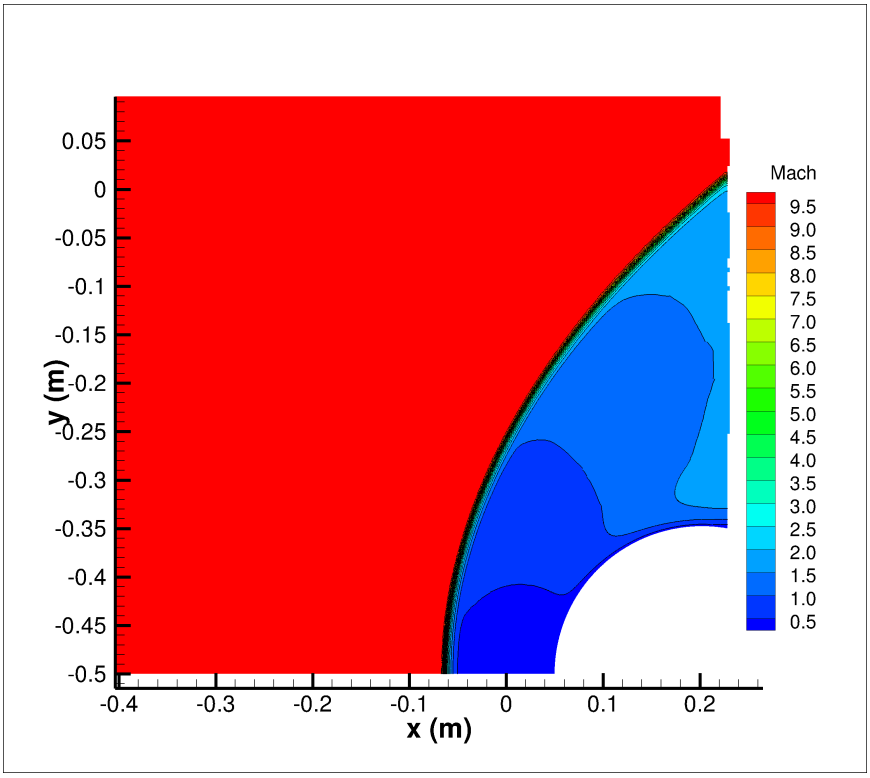

Figure 29: Mach 10, Re 1445 flow: Mach contours: finer grid

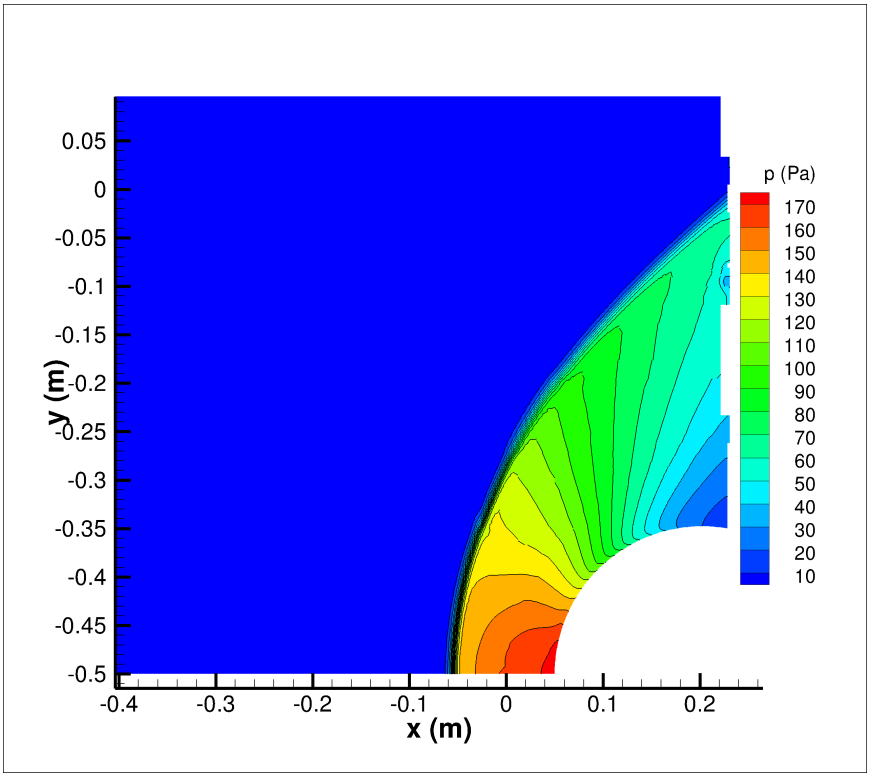

Figure 30: Mach 10, Re 1445 flow: pressure contours: coarse grid

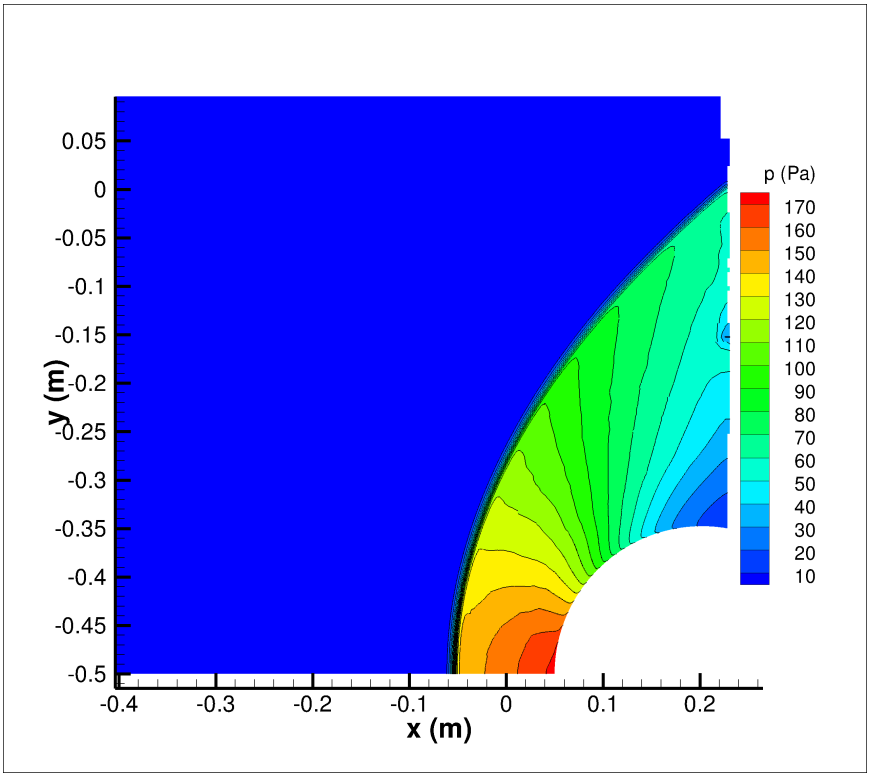

Figure 31: Mach 10, Re 1445 flow: pressure contours: finer grid

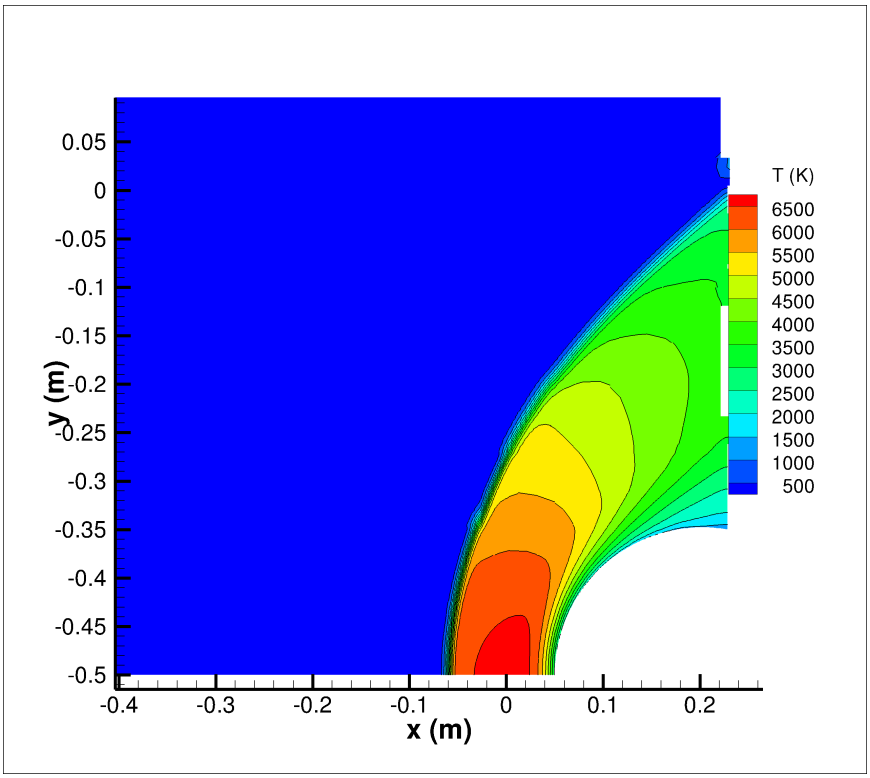

Figure 32: Mach 10, Re 1445 flow: temperature contours: coarse grid

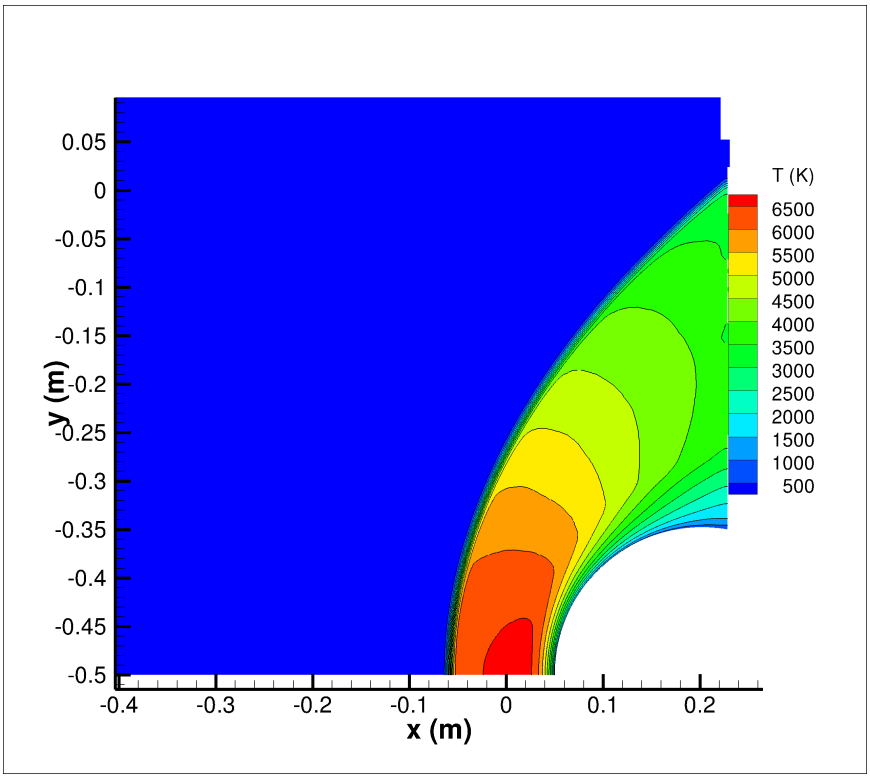

Figure 33: Mach 10, Re 1445 flow: temperature contours: finer grid

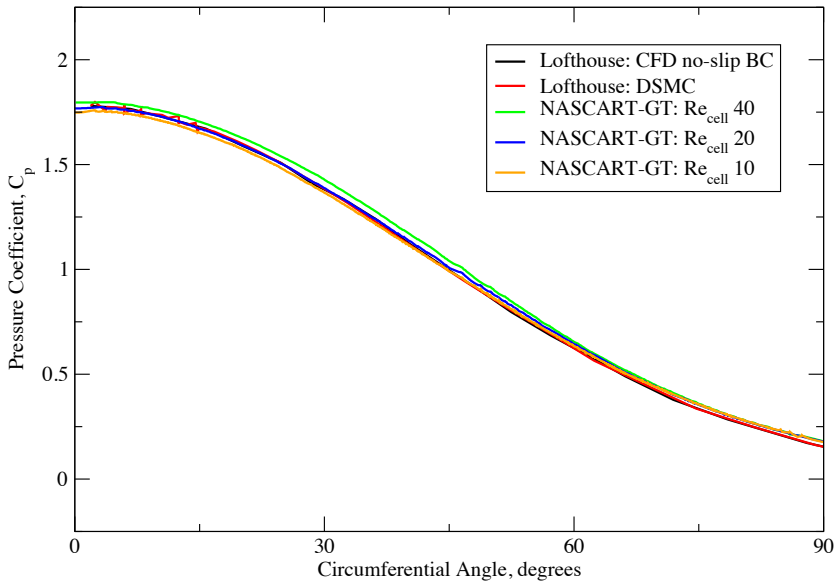

Figure 34: C_p distribution: Mach 10, Re 1445

deviations from the reference values for the entire range of cell sizes. In addition to being under-predicted, the shear stress at the surface is significantly noisier compared to the reference predictions. The heat transfer rate magnitude fares better, but here too the effects of the non-uniformity of surface panel sizes and orientations is evident. The peak heating rate predicted by NASCART-GT overshoots the reference peak, and the curve starts to deviate from the reference plots along the circumference of the cylinder. For both of these properties, it is encouraging that the trend shifts towards the reference data as the cell sizes in the computational domain drop. The impact of the the grid cell sizes and the grids used to predict these values are explained in detail later.

4.2.2 Impact of Grid Adaption Parameters: Temperature

During the preliminary investigation, solution adaption was performed based on velocity divergence and vorticity gradients in the computational domain. This strategy managed to capture the shock and the boundary layer very well (away from the stagnation region). In the stagnation region though, where there is a pocket of highly viscous slow moving

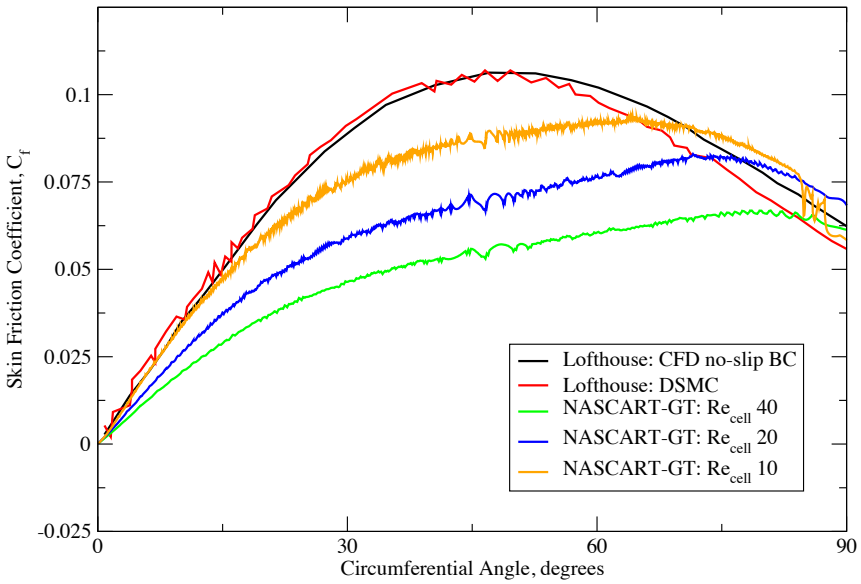

Figure 35: C_f distribution: Mach 10, Re 1445

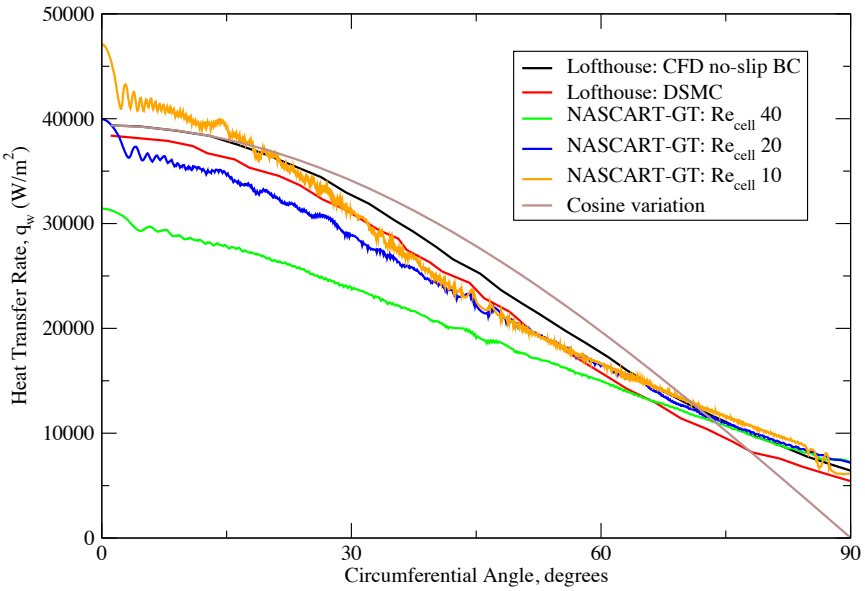

Figure 36: $\dot{q}_w$ distribution: Mach 10, Re 1445

fluid, any combination of the vorticity and divergence gradient parameters failed to adapt to the temperature gradients present there. Any reasonable prediction of convective heating requires good resolution of the thermal boundary layer and the temperature gradients in the stagnation region. The solution adaption strategy was appropriately modified to include the gradients of temperature (and stagnation enthalpy) amongst the list of adaption parameters. This improved the resolution of the thermal boundary layer, evidence of which is presented in Figs. 37 and 38.

Here, the grid adapted using velocity divergence and vorticity gradients is presented on top, and the grid that had temperature gradient inclusive adaption is presented below. The results presented in the previous sections, therefore, included temperature gradients in the list of adaption parameters.

4.2.3 Impact of $\mathbf{Re_{wall}}$

Prior studies have shown that the parameter $\mathrm{Re_{wall}}$ (defined in Eq. 96) plays a critical role in the accuracy of the predicted heating rates. Arslanbekov et al. [6] have shown using a different unstructured Cartesian grid based solver (UFS) that for the same flow conditions presented here, an $\mathrm{Re_{wall}}$ of unity is required to match the predictions of both LeMANS and MONACO. UFS uses a different set of wall boundary conditions (Maxwell's slip conditions [54]), and therefore the corresponding $\mathrm{Re_{wall}}$ requirements for NASCART-GT's no-slip immersed boundary approach could very well be different. In fact, the results presented here show that this solver is capable of reasonable levels of accuracy in predicting convecting heating rates even with higher than unity $\mathrm{Re_{wall}}$ values. For the $\mathrm{Re}_\infty = 289$ test case, the surface properties shown in Figs. 23-25 compare the results using grids corresponding to 3 different $\mathrm{Re_{wall}}$ values. The pressure, as seen before, is hardly affected by the variations in the grid cell sizes, whereas the shear stress and convective heat flux predictions are more sensitive to this parameter. Despite that, even for an $\mathrm{Re_{wall}}$ of 4, only a marginal difference in the skin friction and heating values are noticed ($< 5\%$). Of course, as $\mathrm{Re_{wall}}$ reaches unity, the thermal boundary layer is perfectly resolved, and the resulting heating prediction is the most accurate.

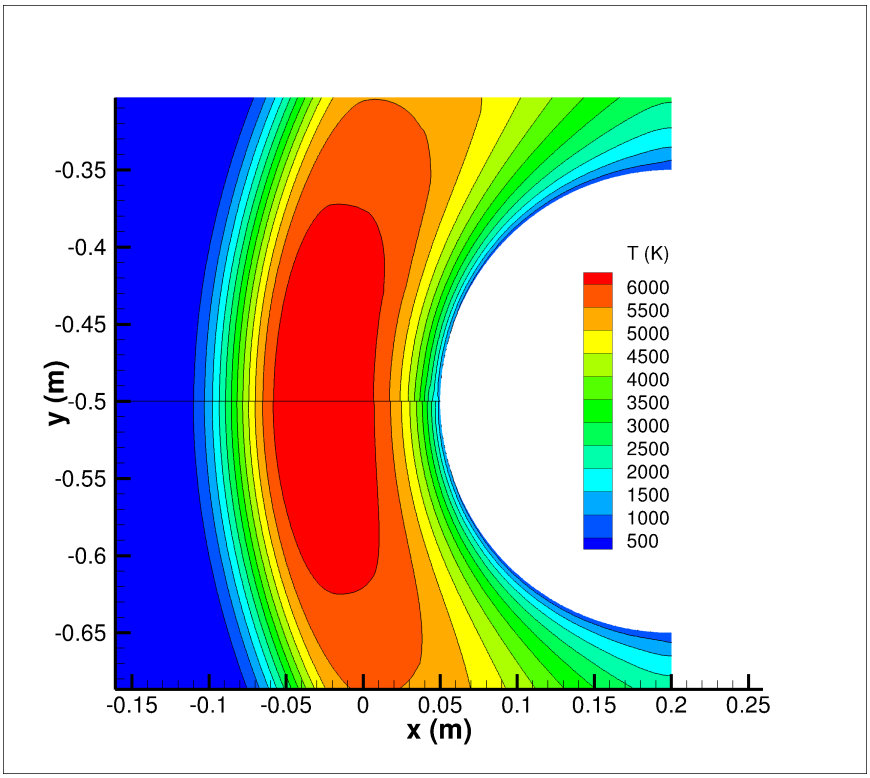

Figure 37: Mach 10, Re 289 flow: solution adaption without and with T gradients

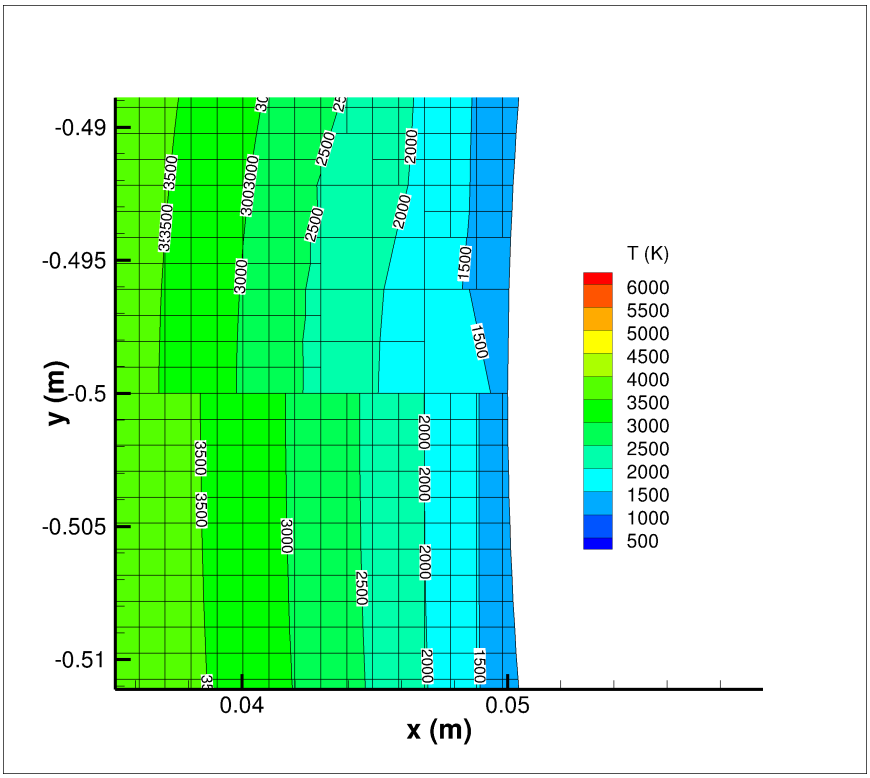

Figure 38: Mach 10, Re 289 flow: solution adaption without and with T gradients: close-up

For the $\mathrm{Re}_\infty = 1445$ case, results using $\mathrm{Re}_{\mathrm{wall}}$ values that are an order of magnitude higher were presented. This was largely because of the computational costs associated with such simulations, which required excessive number of small grid cells to adequately resolve the thermal boundary layer. By analyzing these coarse grid simulations, it also helps to establish a trend regarding the accuracy of the predictions for larger $\mathrm{Re}_{\mathrm{wall}}$ values. Unlike the $\mathrm{Re}_\infty = 289$ case, the $\mathrm{Re}_{\mathrm{wall}}$ values for the presented results ranged from 10-40. The pressure continued to be largely unaffected even for such coarse grid simulations. Deviations in the heating and skin friction predictions were more significant, given the magnitude of the $\mathrm{Re}_{\mathrm{wall}}$ values; for the case with $\mathrm{Re}_{\mathrm{wall}} = 40$, the C_f predictions were nearly 50% less than the expected values.

In addition to the accuracy of these predictions, variations in properties along the surface also differed for different grid setups. This aspect is analyzed next.

4.2.4 Impact of Surface Grid Width (XBL)

In the heating curves presented earlier, the theoretical cosine variation of the convective heating along the wall for the cylinder is overlaid for reference. A comparison of the predictions by NASCART-GT and the reference results shows an interesting trend in the estimation of the heating rates along the surface.

The $\mathrm{Re}_\infty = 289$ case compares very well with the reference curves throughout the surface of the cylinder. For the $\mathrm{Re}_\infty = 1445$ case, deviations from the reference values are evident to different extents for various $\mathrm{Re}_{\mathrm{wall}}$ values. For a more detailed insight into this, this case was run using 3 different grid with the same $\mathrm{Re}_{\mathrm{wall}}$ value of 40. The differences in the grids were in the width of the fine viscous grid cells used near the wall, and the extent to which these were extended into the flow.

Figures 39-44 show the grids generated for this study, and the corresponding plots of the temperature in the stagnation region. In the first setup (Figs. 39 and 40), the fine viscous cells are set to extend to a distance of 0.001 m normal from the wall. For the second setup (Figs. 41 and 42), this is increased to 0.005 m, and the third (Figs. 43 and 44 has this extend to 0.01 m.

With these settings, the extent to which these fine grid cells "dip" into the high temperature bubble behind the shock wave differ. The first setup hardly has any cells that extend into this high temperature region, whereas both the second and the third setups allow for cells to "dip" into this region to various extents.

A plot of the corresponding heating predictions for this case using each of these grid settings is shown in Fig. 45. There is a significant 20% spike in the peak heating rate predicted using the first grid, compared to the other two grids. The latter two curves fall right on top of each other.

It is postulated that the extent to which the fine band of viscous cells extends into the high temperature region has a significant impact on the accuracy and the overall variation of the surface heating predictions. In the former case, large portions of the high temperature bubble are resolved by very coarse cells, and the fine band of cells that encompass the geometry draw information from these grid cells. The unstructured nature of the Cartesian grid framework requires interpolation of state properties to populate the flux integration stencil in regions of varying refinement levels. Therefore, errors are propagated from the coarse grid region to the surface, adversely affecting the heating predictions at the wall.

Having a wider band of viscous surface cells allows for these fine grid cells to make more accurate interpolations. As seen from latter two setups, the extent to which these cells extend into the high temperature region does not have any impact on the surface predictions, so long as they have a significant number of cells that resolve this region.

4.3 Stagnation Point Heating Prediction Comparisons

In order to confirm NASCART-GT's prediction of convective heating rates over a range of hypersonic Mach numbers, test cases were set up for an axisymmetric hemisphere geometry. The computed stagnation point heat rates were compared with experimental results and empirical relations.

Yee et al. [107] conducted a series of ballistic range measurements of stagnation point heating in air and carbon dioxide for hypersonic velocities up to 18,000 ft/s (5.4864 km/s). The flow conditions for these experiments were at an ambient temperature of 540° R (300

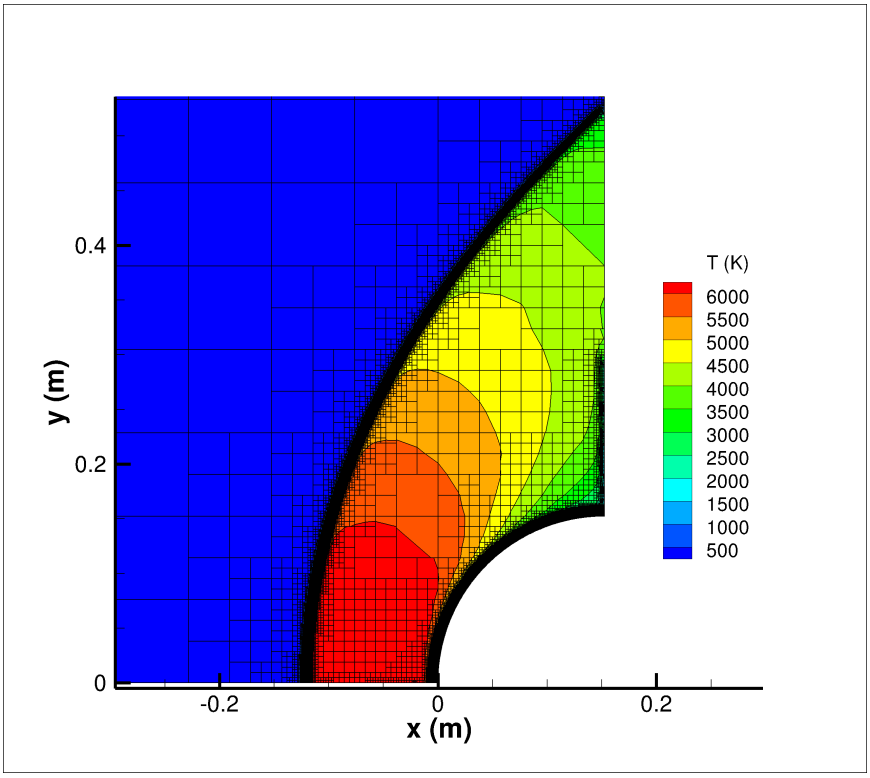

Figure 39: Mach 10, Re 1445 flow: XBL = 0.01 m - overlay

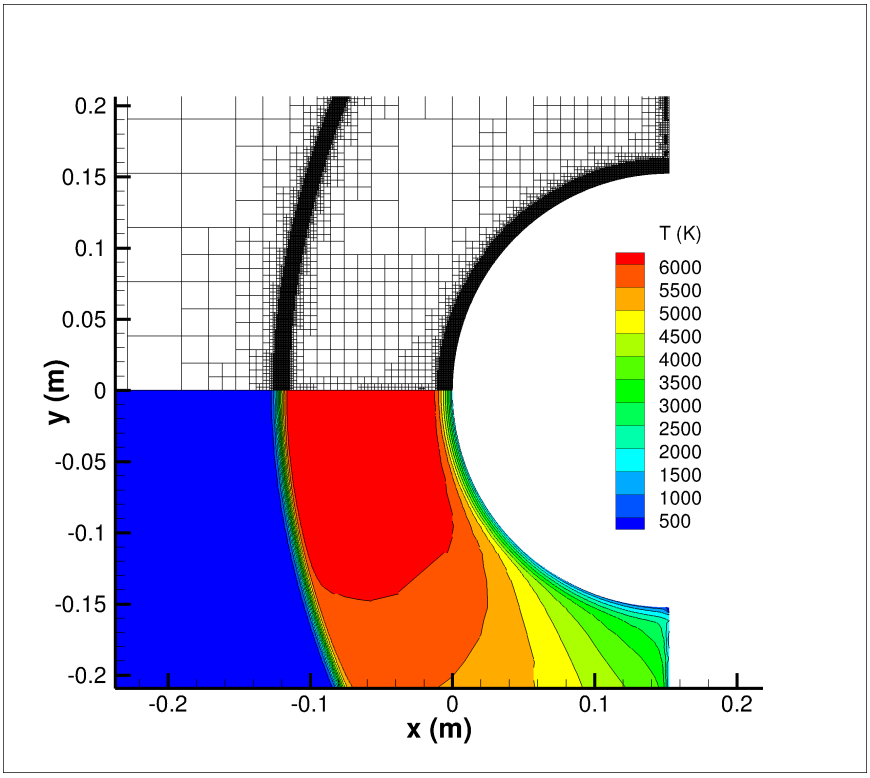

Figure 40: Mach 10, Re 1445 flow: XBL = 0.01 m - separate

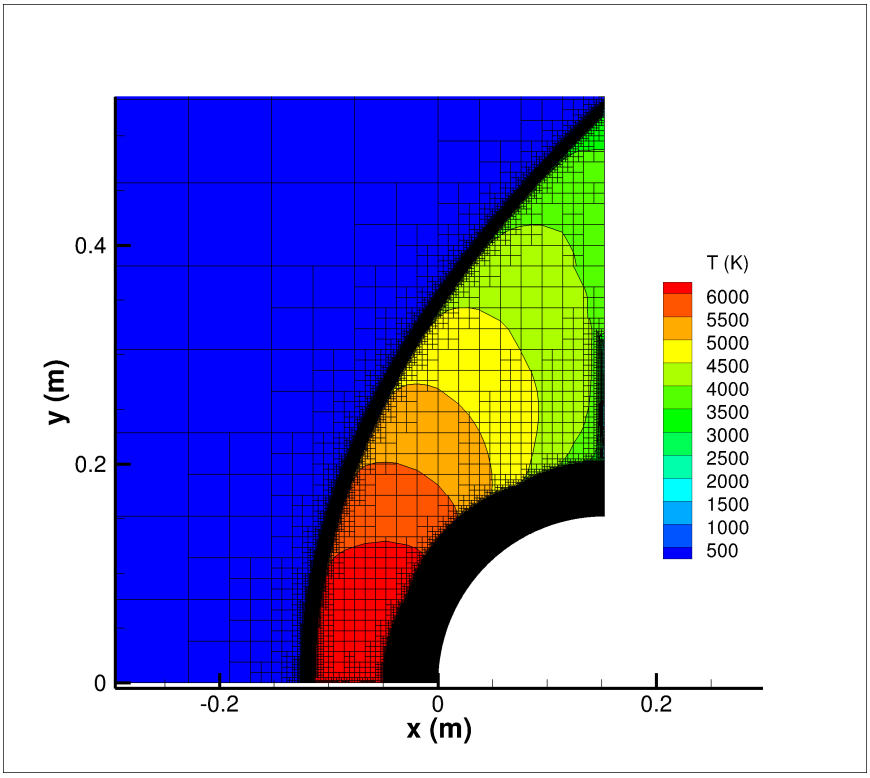

Figure 41: Mach 10, Re 1445 flow: XBL = 0.05 m - overlay

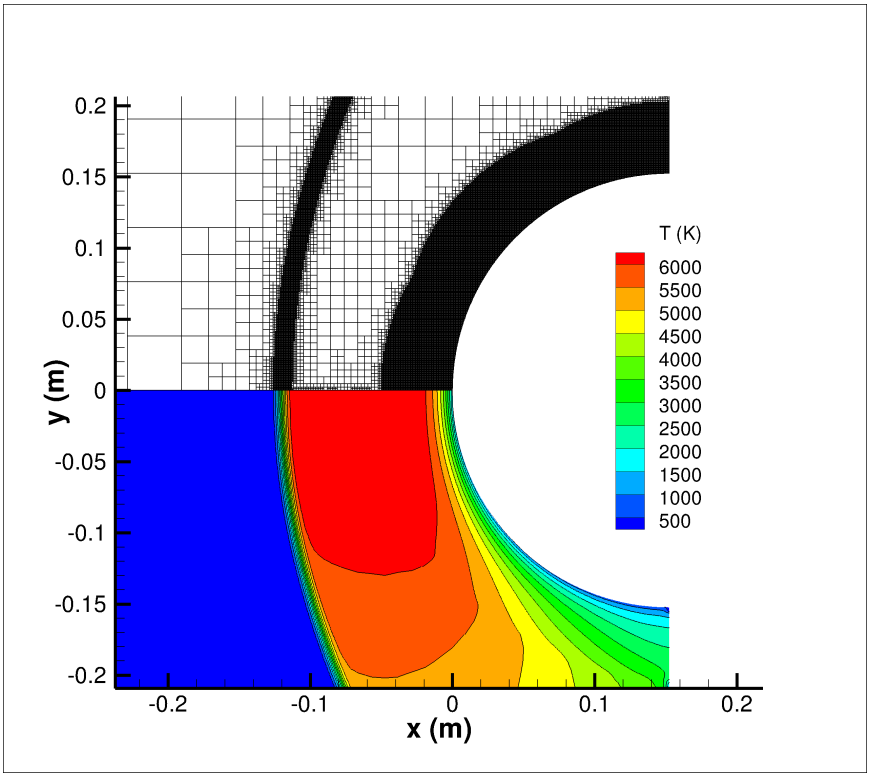

Figure 42: Mach 10, Re 1445 flow: XBL = 0.05 m - separate

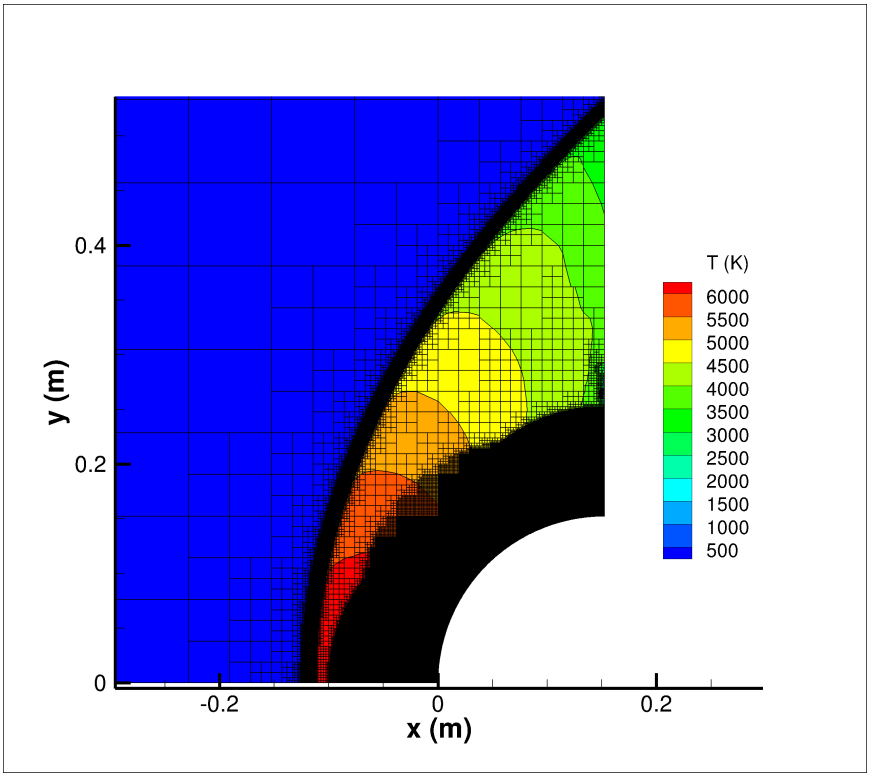

Figure 43: Mach 10, Re 1445 flow: XBL = 0.1 m - overlay

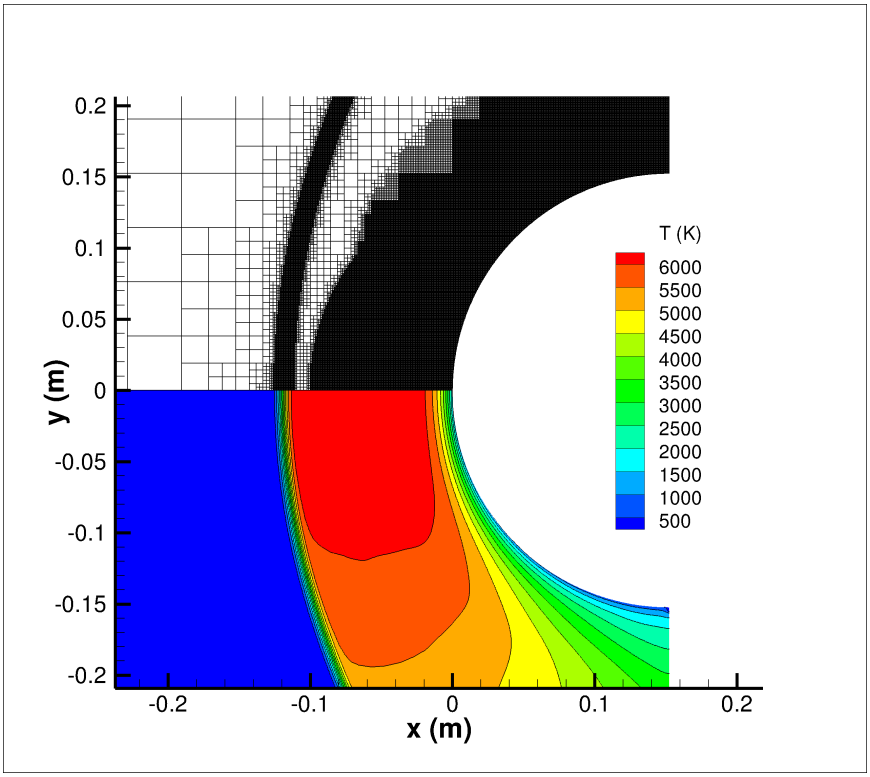

Figure 44: Mach 10, Re 1445 flow: XBL = 0.1 m - separate

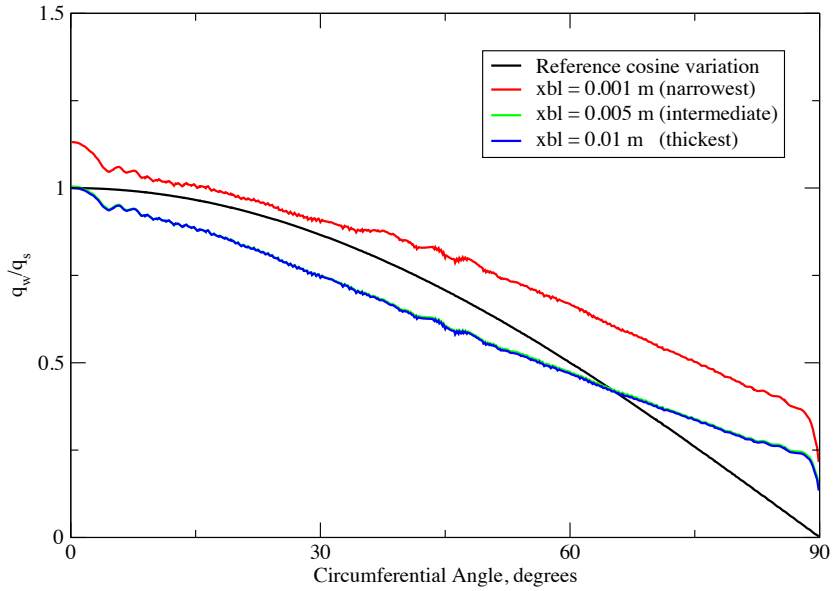

Figure 45: Mach 10, Re 1445 flow: Comparisons of XBL settings

K) and a pressure of 10132.5 Pa ($1/10^{\text{th}}$ of standard atmosphere). A spherical-nosed model (radius 0.11", 0.00274 m) was launched from a light-gas gun, and the ballistic range was instrumented with spark shadowgraphs and electronic chronographs, as well as pickup coils for measurements.

Comparisons were made with estimates using empirical relations in that reference. Fay and Riddell [26] developed the theory of stagnation point heating in their seminal paper by deriving the boundary layer equations for high speed external dissociated flow. The local heat transfer rate was determined by the sum of the conductive and diffusive terms, and was theoretically derived to be:

$$\dot{q} = \left(\mathrm{Nu}/\sqrt{\mathrm{Re}}\right) \sqrt{\rho_w \mu_w \left(du_e/dx\right)_s} \left[\left(h_s - h_w\right)/\mathrm{Pr}\right] \tag{97}$$

where, Nu, Re and Pr are the local Nusselt, Reynolds and Prandtl numbers. Subscript w refers to the wall conditions, and s denotes the stagnation point values. Based on empirical relations, this equation (Eq. 97) reduces to:

$$\dot{q}_s = 0.94 \left(\rho_w \mu_w\right)^{0.1} \left(\rho_s \mu_s\right)^{0.4} \left\{1 + \left(L^{0.52} - 1\right)\left(h_D/h_s\right)\right\} \left(h_s - h_w\right) \sqrt{\left(du_e/dx\right)_s} \tag{98}$$

Table 5: Stagnation point heating freestream velocities

V_∞ (kft/s)	M_∞
10	8.778
12	10.534
14	12.29

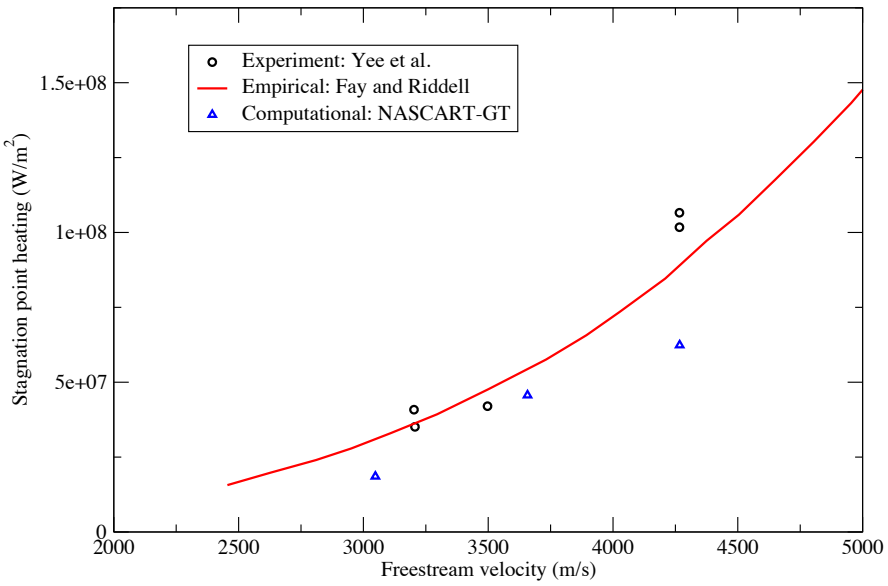

Figure 46: $\dot{q}_w$ stagnation point: hemisphere

NASCART-GT was setup to compute a series of these test conditions for a similar hemispherical geometry (axisymmetric test case). The density in the freestream was computed to be 0.1177 kg/m^3 and the velocities for these tests are listed in Table 5:

Figure 46 shows the comparison of the stagnation point heating predicted by NASCART-GT with the experimental and empirical results from Ref. [107].

These cases where run using the LU-SSOR implicit time integration scheme, with CFL numbers ramped from 0.1 to 100. As evident from Fig. 46, NASCART-GT under-predicts the stagnation point heating when compared to the experimental and empirical results. This is attributed to the coarse grids that were used for this series of test cases, and varies

for different Re_{wall} setups. For example, the $M_\infty = 8.778$ case shows a 15% under-prediction of the stagnation point heating, whereas the $M_\infty = 10.534$ shows an improved 5% under-prediction. The overall trend in the stagnation point convective heating rates compares reasonable well with the references.

CHAPTER V

FROZEN FLOW RESULTS - II

5.1 Frozen Flow Surface Prediction Comparisons - Complex Flows

One advantage in using an unstructured grid solver is its ability to adapt the grid based on the gradients in the computational domain as the solution develops. With this, regions with strong shock waves and vorticular structures can be well defined with a large number of grid points and very small cells, ensuring sharper resolution of such phenomena.

Following the 2-D cylinder simulations, an axisymmetric case that involves complicated flow physics was chosen. The adaptive mesh refinement strategy of NASCART-GT was evaluated for computing complex hypersonic flows. This case has a compression corner which results in the interaction of a hypersonic shock wave and boundary layer. As a results, the boundary layer separates generating a circulation bubble. The solution adaption capability in the solver is naturally catered to capturing such phenomena well.

The freestream Reynolds number for this case was higher than those used in the cylinder test cases ($\mathrm{Re}_\infty \approx 213,000$ for the hollow cylinder-flare geometry), which demanded extremely small cells in the boundary layer to reach an $\mathrm{Re}_{\mathrm{wall}}$ of unity. Considering the cost of such cell-intensive computations, this investigation is being treated as a demonstrative study to evaluate the immersed boundary ghost cell approach in predicting surface physics in the presence of a separation bubble. As a means of keeping the cell count within reasonable limits, relatively coarser grids were used to compute this flow.

This case involves hypersonic nitrogen gas flow. Assuming the gas to be frozen, Sutherland's equation was used to determine the transport properties ($C_1 = 1.401 \times 10^{-6}$, $C_2 = 107$ K). The ratio of the specific heats (γ) was taken to 1.4, and the Prandtl number was set at 0.73439.

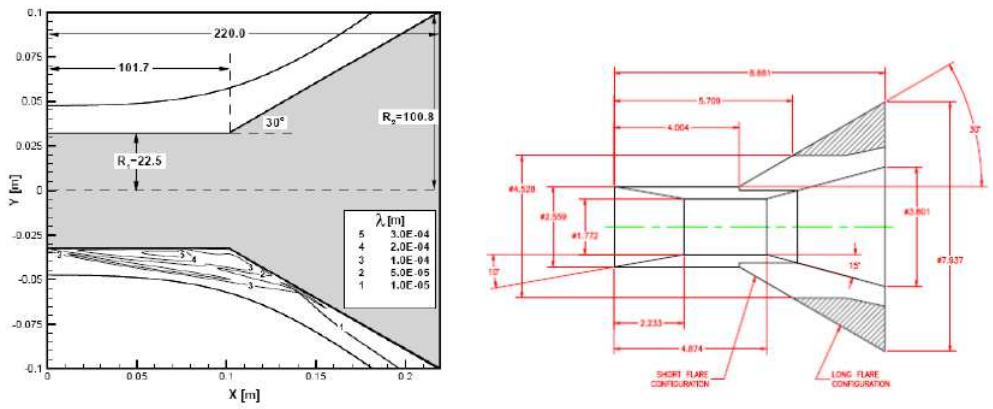

Figure 47: Schematic of the hollow cylinder flare geometry

5.1.1 Hollow Cylinder Flare in Mach 12.4 Nitrogen Flow

Hypersonic flow over a hollow cylinder flare (CUBRC Run 11 of the benchmark cases developed by the NATO Research Technology Organization [39, 43, 38]) was the complex flow test case considered. This axisymmetric model consists of a hollow cylinder followed by a surface sloped at 30° (Fig. 47). The two surfaces result in a boundary layer which separates at the surface junction due to the flow turning and the shock wave generated by the flare. The complexity of the flow physics of the hypersonic shock wave-boundary layer interaction and the prediction of the heat transfer in such a region make this a difficult but realistic validation test case. This configuration has been extensively studied numerically [63, 89], and experimental measurements have provided reference surface pressure, surface heat transfer and Schlieren photographs. The resulting shock intersects the flare, producing a spot of high density, pressure and heat transfer. The freestream flow conditions for the CUBRC Run 11 are given in Table 6.

Preliminary analysis of this case showed a separation bubble that was very sensitive to the temperature clipping strategy used in the immersed boundary ghost cell methodology. Therefore, 2 settings for this strategy were analyzed, where the ghost cell temperatures were not allowed to fall below 1/2 and 1/4 of the reference point value.

Each of these cases was run using the implicit LU-SSOR scheme with the CFL number ramped from 0.1 to 10,000. Initially, solution adaption of the flow cells was carried out

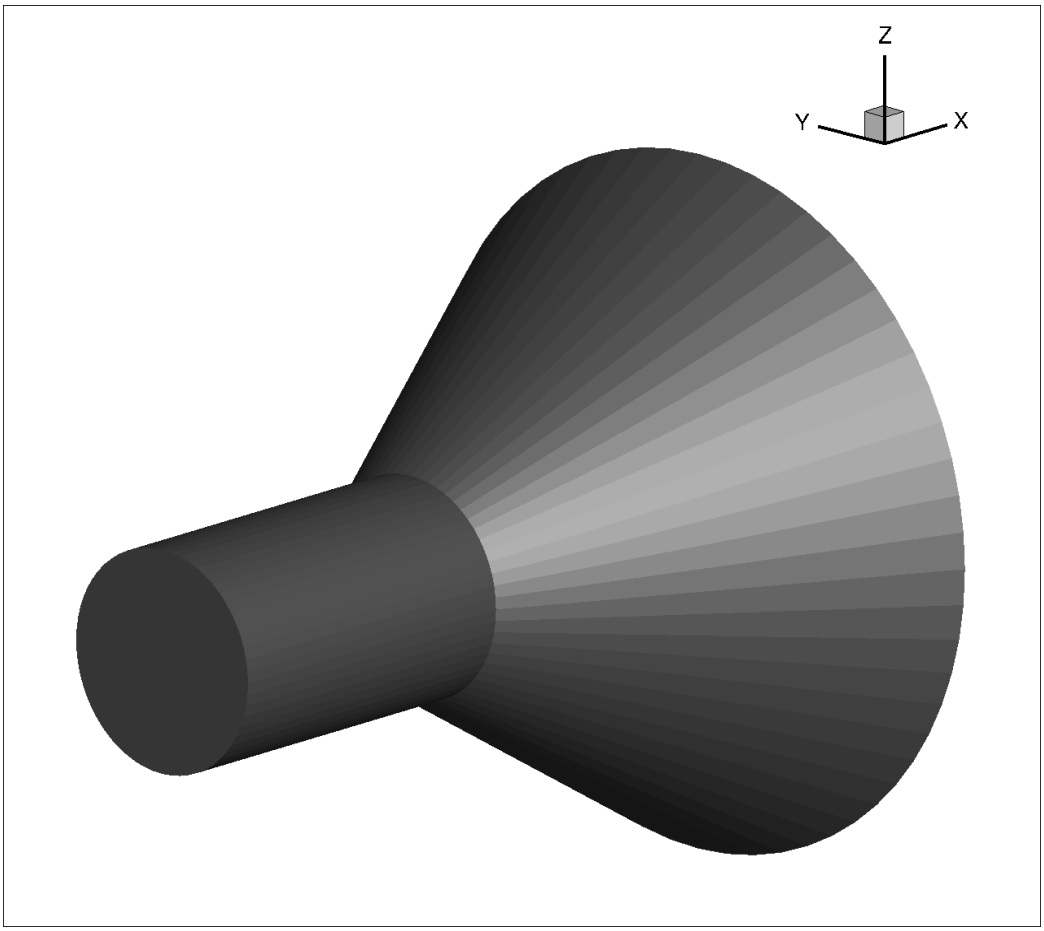

Figure 48: Original surface of the hollow cylinder flare geometry

Table 6: CUBRC Run 11 test conditions

Freestream parameter	Value
M_∞	12.4
V_∞	2471.4 m/s
ρ_∞	5.566×10^{-4} kg/m^3
T_∞	95.6 K
T_{wall}	297.2 K

based on velocity divergence and gradients of the stagnation enthalpy. Further, adaption of the surface cells was turned on and the simulations were continued for 3 additional cycles of refinement, which reduced the minimum cell size in the computational domain by an order of magnitude. Thus, $\mathrm{Re}_{\mathrm{wall}}$ for this case dropped from a peak value of ≈ 500 to 55. The coarse and fine converged grids for both temperature clipping strategies are shown in Figs. 49-52.

These axisymmetric simulations resulted in approximately 55,000 cells for the coarse grid and 1.35 million cells for the fine grid setups, with the smallest cell sizes being of the order of 10^{-4} and 10^{-5} m, respectively. It should be noted here that a viscous-band of cells along the surface was exempted from coarsening, to make sure that the boundary layer was resolved adequately. The width of this viscous band was set to the theoretical Blasius boundary layer thickness.

The results of the simulations are presented in the form of contour plots of the Mach number (Figs. 53-56), pressure (Figs. 57-60) and temperature (Figs. 61-64) in the computational domain. Two sets of results each for both temperature clipping strategies are shown, converged for both the coarse and finer grid simulations.

The most striking observation from each of these plots is that the location of the shock wave-boundary layer interaction is consistent with both temperature settings, and for both coarse and finer grids. This compares very well with experimental observations, where the point of interaction lies approximately 0.14 m along the X-axis (Fig. 47).

The size and the location of the separation bubble also compares well qualitatively with experiments, and is consistently predicted in each case. Given the unsteady nature of this setup, it was observed that when solution adaption was performed at a lower frequency, the prediction of the location of the shock wave-boundary layer interaction and the size of the separation bubble compared poorly with experiment. The unsteady nature of this test case prevented the residuals from continuing to drop, setting the residual history up for a limit cycle. Frequent adaptive refinement is therefore essential in capturing the complex flow phenomena in simulations such as this, especially when using reasonably large CFL numbers in the implicit time integration scheme. For this case, adaption was performed

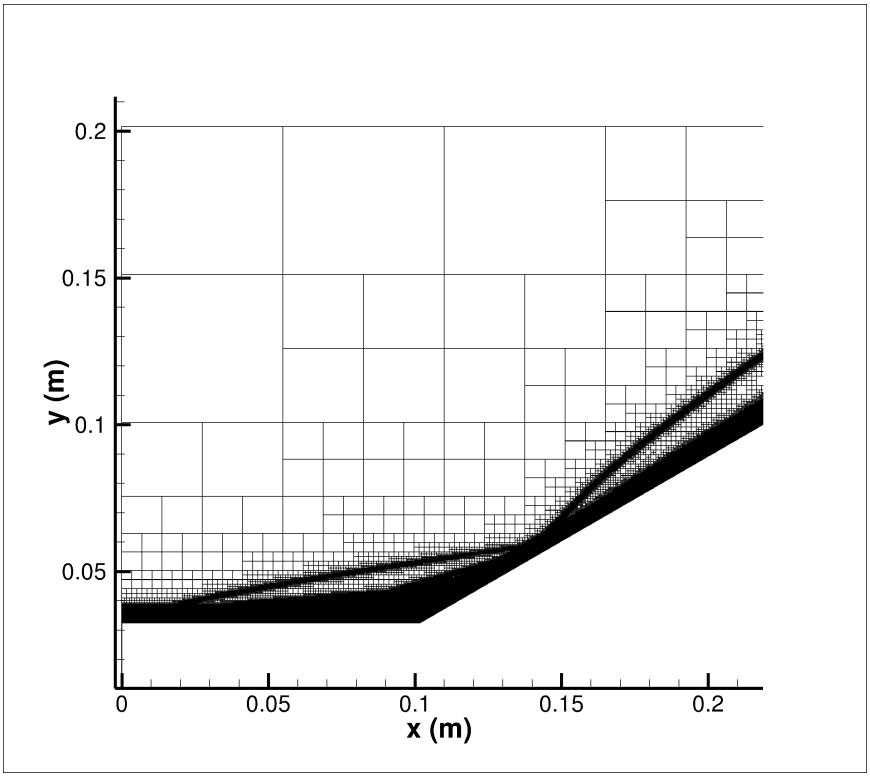

Figure 49: CUBRC Run 11: coarse grid [$T_{ghost} \geq 0.5T_{reference}$]

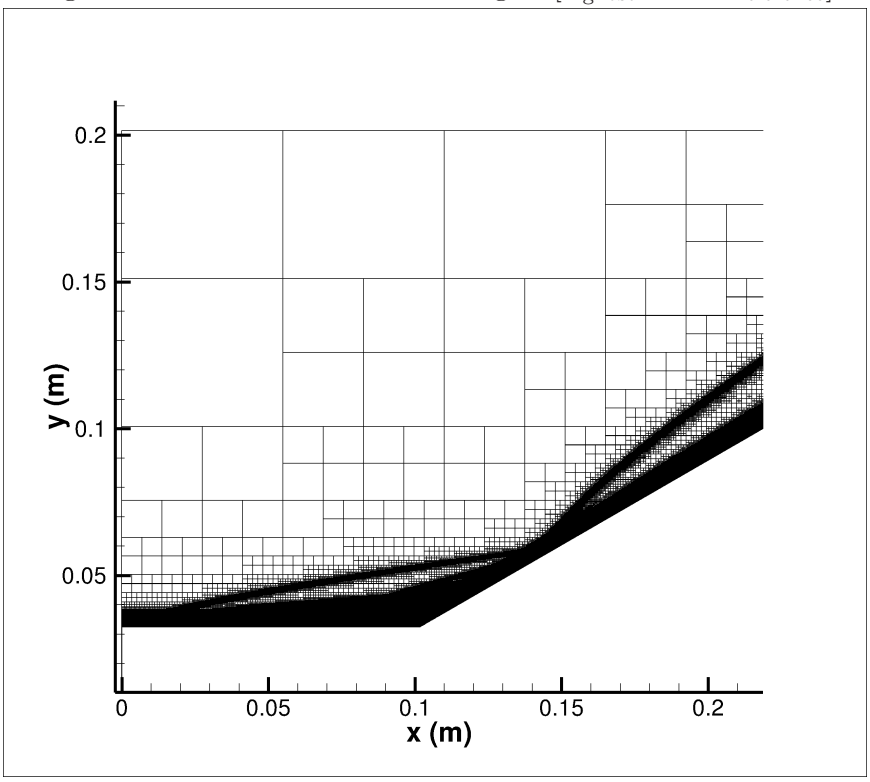

Figure 50: CUBRC Run 11: finer grid [$T_{ghost} \geq 0.5T_{reference}$]

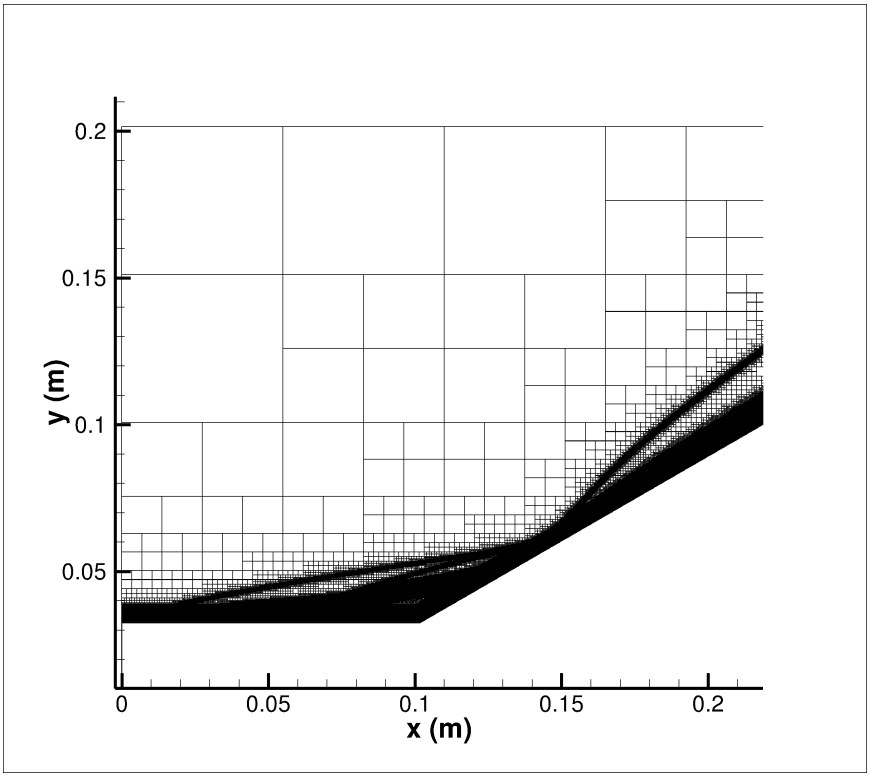

Figure 51: CUBRC Run 11: coarse grid [$T_{ghost} \geq 0.25 T_{reference}$]

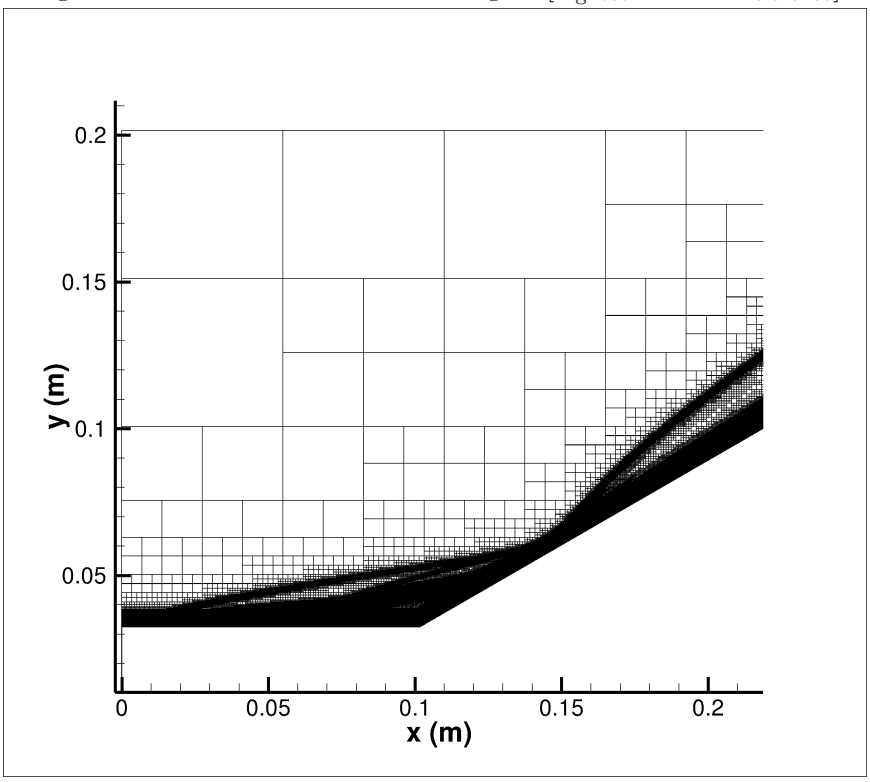

Figure 52: CUBRC Run 11: finer grid [$T_{ghost} \geq 0.25 T_{reference}$]

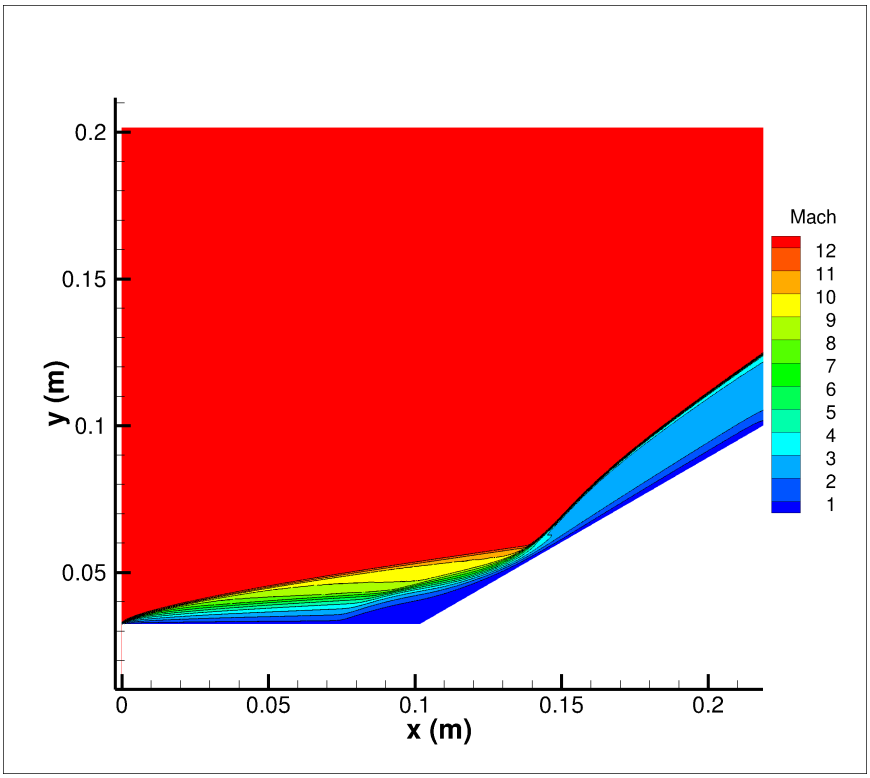

Figure 53: CUBRC Run 11: Mach contours, coarse [$T_{ghost} \geq 0.5T_{reference}$]

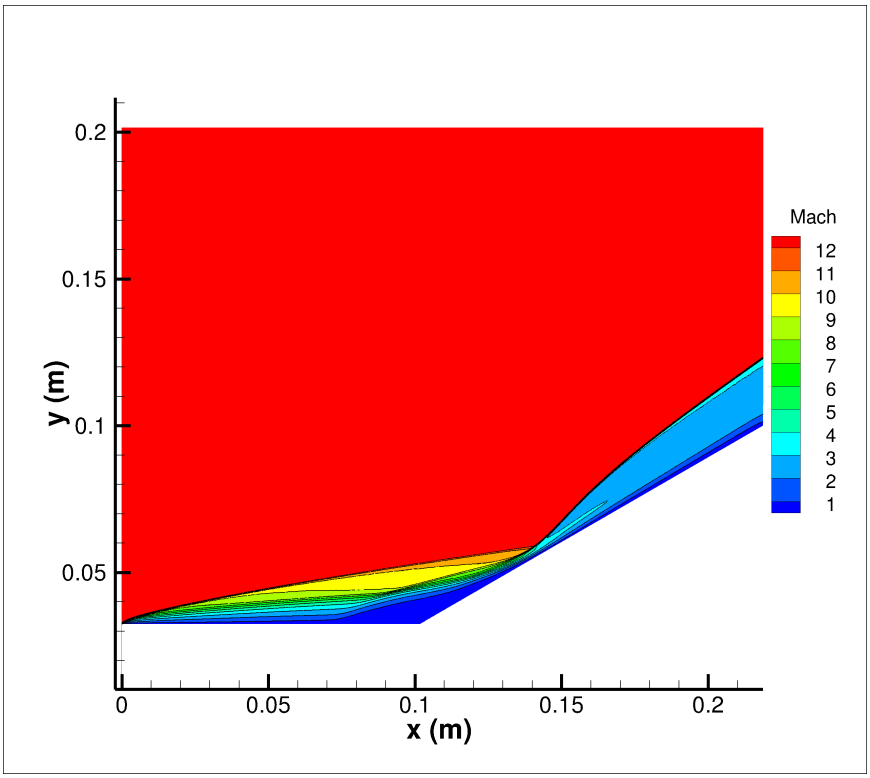

Figure 54: CUBRC Run 11: Mach contours, finer [$T_{ghost} \geq 0.5T_{reference}$]

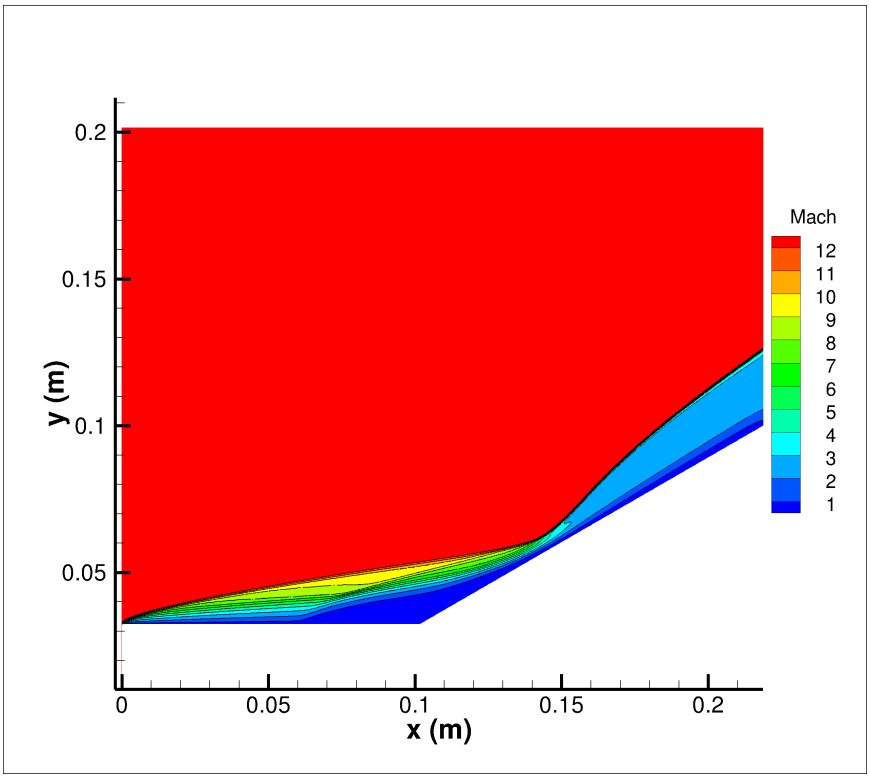

Figure 55: CUBRC Run 11: Mach contours, coarse [$T_{ghost} \geq 0.25T_{reference}$]

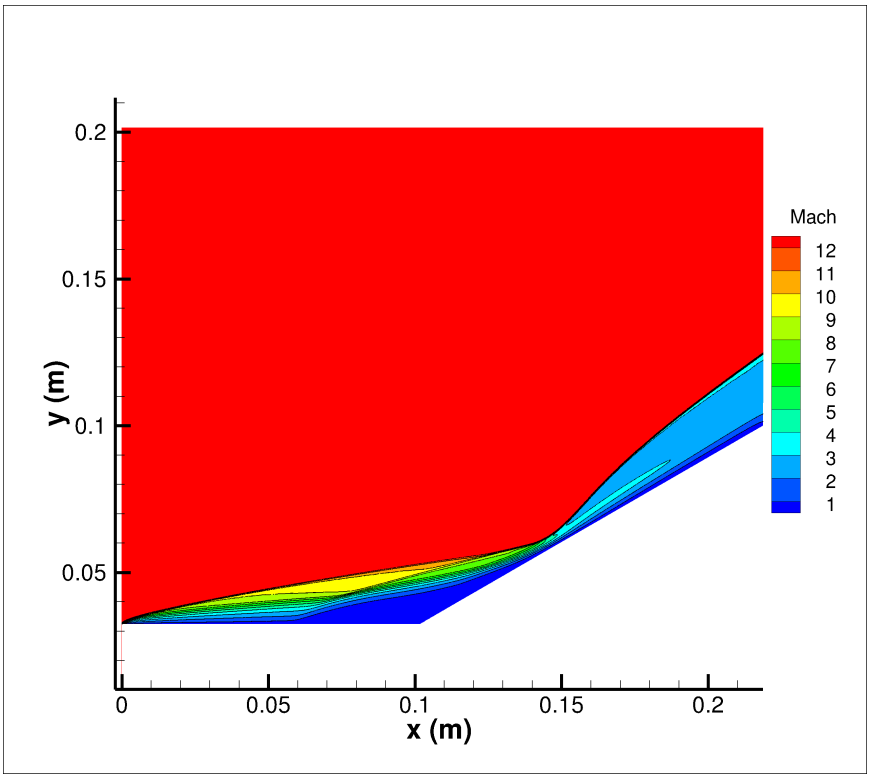

Figure 56: CUBRC Run 11: Mach contours, finer [$T_{ghost} \geq 0.25T_{reference}$]

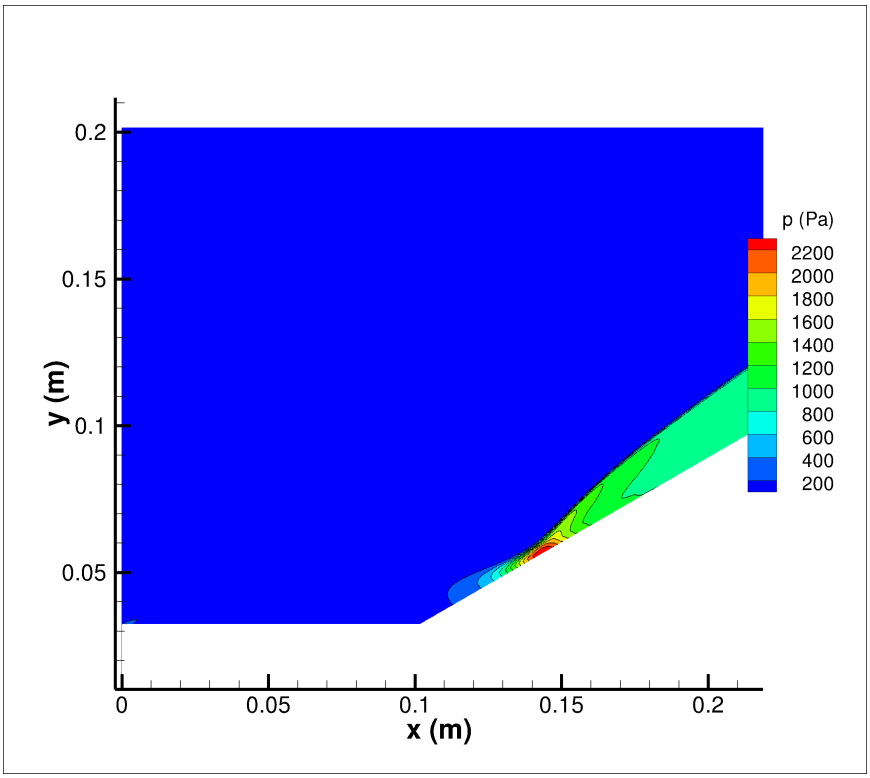

Figure 57: CUBRC Run 11: pressure contours, coarse [$T_{ghost} \geq 0.5T_{reference}$]

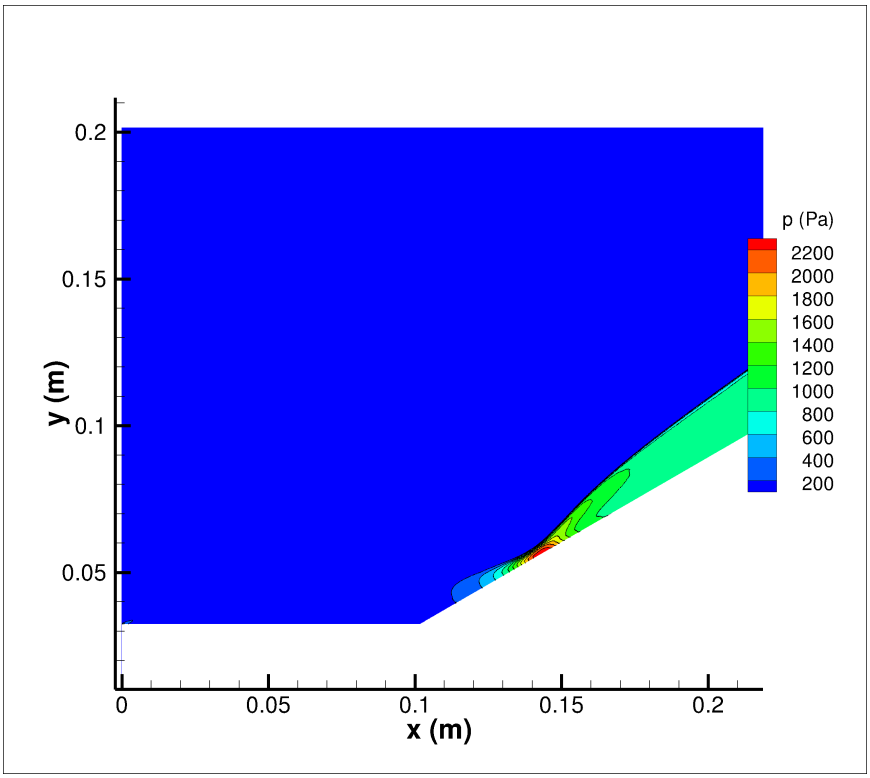

Figure 58: CUBRC Run 11: pressure contours, finer [$T_{ghost} \geq 0.5T_{reference}$]

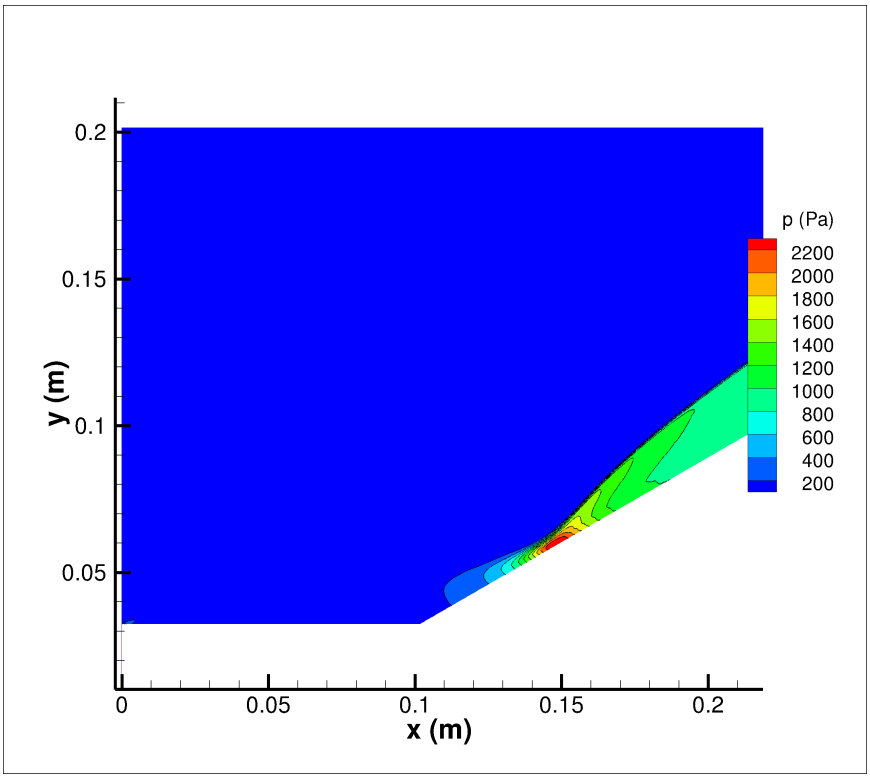

Figure 59: CUBRC Run 11: pressure contours, coarse [$T_{ghost} \geq 0.25T_{reference}$]

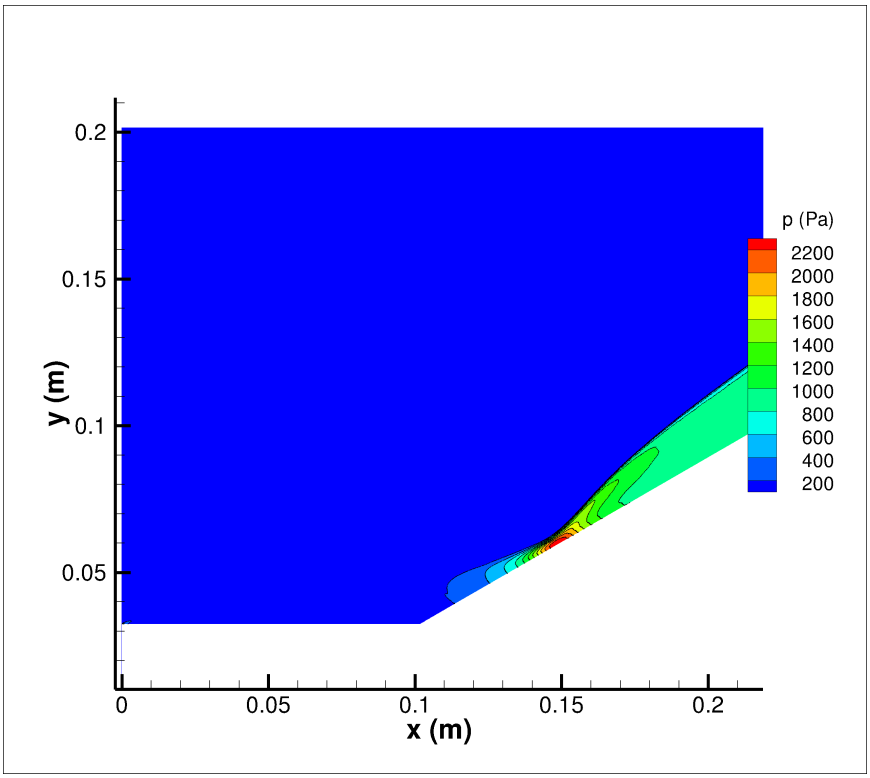

Figure 60: CUBRC Run 11: pressure contours, finer [$T_{ghost} \geq 0.25T_{reference}$]

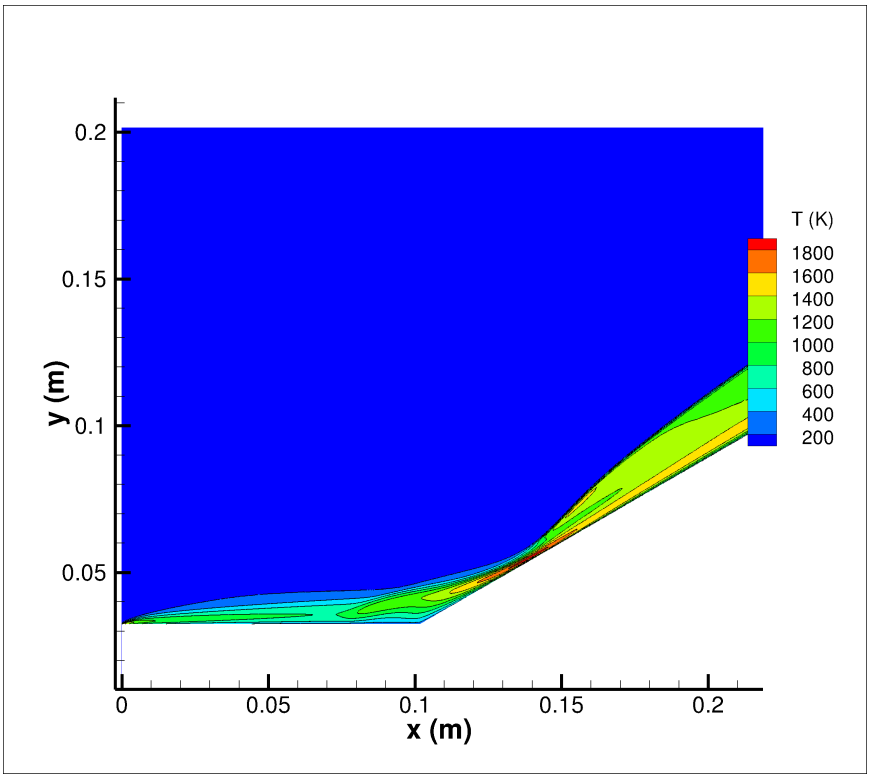

Figure 61: CUBRC Run 11: temperature contours, coarse [$T_{ghost} \geq 0.5T_{reference}$]

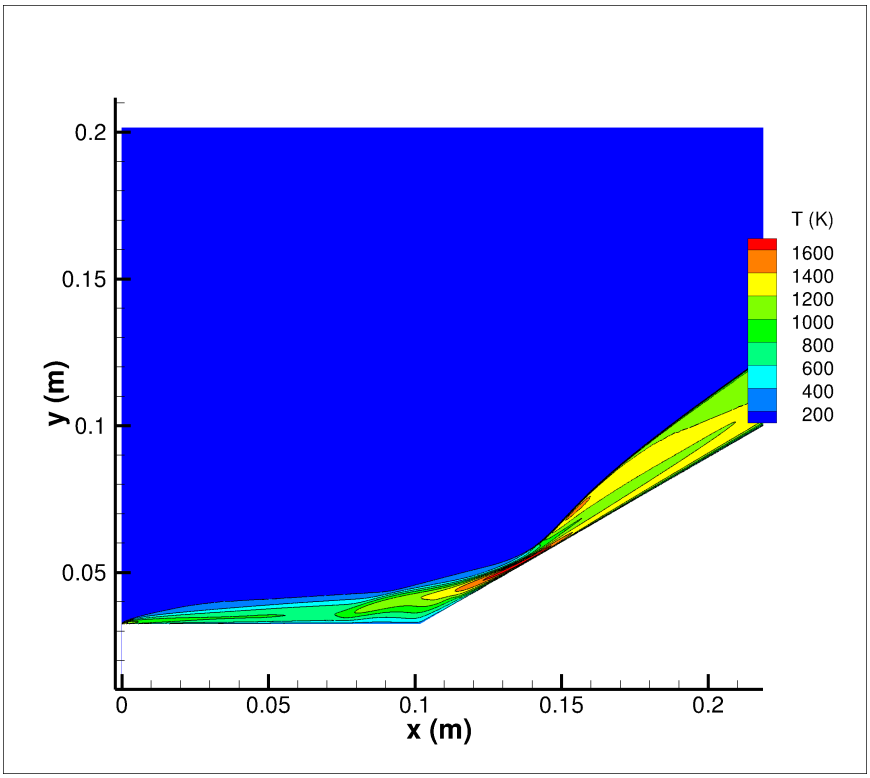

Figure 62: CUBRC Run 11: temperature contours, finer [$T_{ghost} \geq 0.5T_{reference}$]

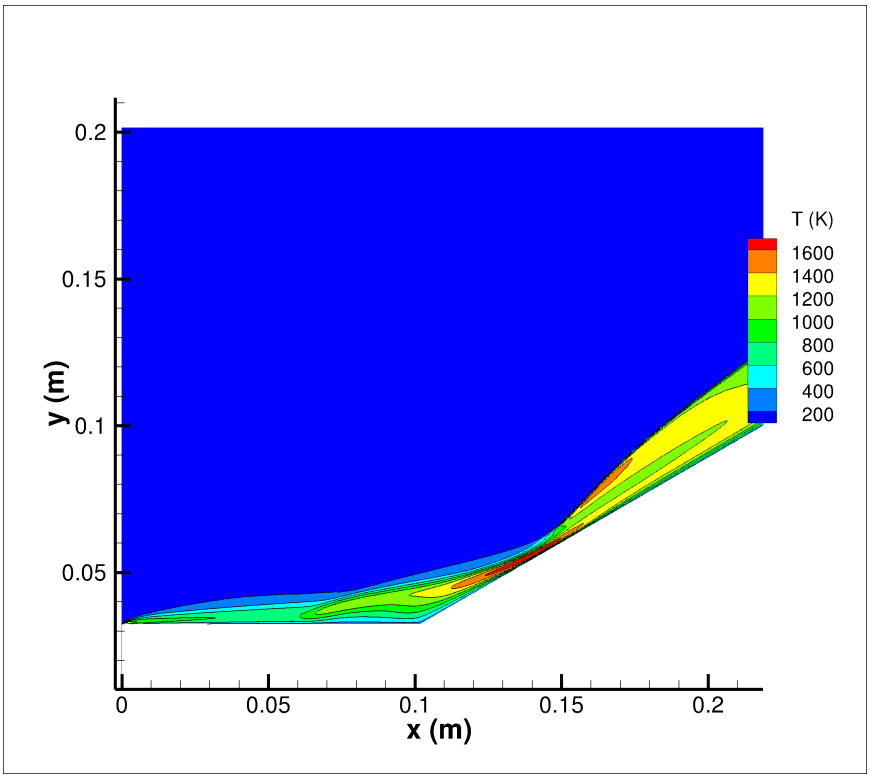

Figure 63: CUBRC Run 11: temperature contours, coarse [$T_{ghost} \geq 0.25T_{reference}$]

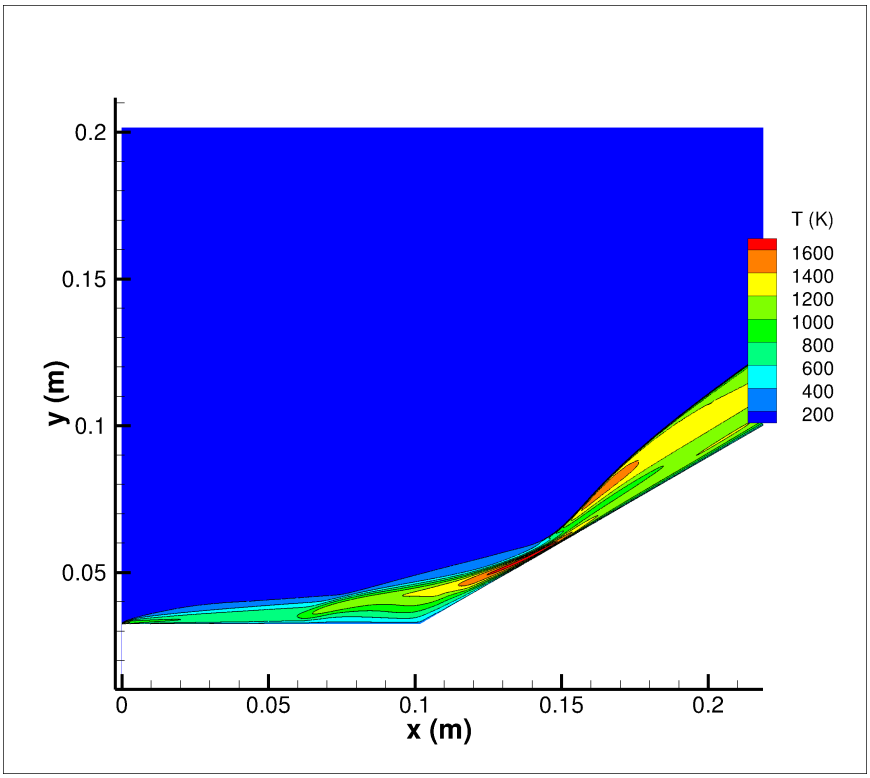

Figure 64: CUBRC Run 11: temperature contours, finer [$T_{ghost} \geq 0.25T_{reference}$]

every 1000 iterations for a total of 25,000 iterations.

The predicted variations of the surface pressure coefficient for both simulation are shown in Figs. 65 and 66. Experimental results are overlaid on these plots for comparing the trends, magnitudes and the locations of the peak pressures.

NASCART-GT shows reasonable agreement for the magnitude of the peak pressure along the surface, which occurs at the point of the shock wave-boundary layer interaction. Both temperature clipping strategies over-predict the peak value by about 10%, though the major features of the pressure variation along the surface are captured well. The adaptive mesh refinement strategy that includes the surface cells shows the right trend as the cell sizes become smaller. The downstream pressure is somewhat over-predicted by the Cartesian grid solver. Prior studies have shown that this magnitude is very sensitive to the numerical scheme used to compute the flow, and the extent of dissipation in the scheme.

It should be re-emphasized here that the $\mathrm{Re}_{\mathrm{wall}}$ associated with the coarse grids is significantly large ≈ 60, but similar to the cylinder cases previously shown, prediction of the variation in pressure along the surface does not require very small surface cells. Overall, reasonable agreement with the experimental data is seen here, with very good comparison of the location of the peak C_p. The more lenient temperature clipping strategy ($T_{\mathrm{ghost}} \geq 0.25 \times T_{\mathrm{reference}}$) makes marginally better estimates of the peak surface pressure.

The convective heat transfer rate variations along the surface of the hollow cylinder flare for these simulations are shown in Figs. 67 and 68. Unlike the C_p variations, the comparison of heating rates fares much worse for both temperature clipping strategies, with the setup that allows for lower surface temperatures significantly under-predicting the peak convective heat transfer rate (by $\approx 50\%$). The impact of the high $\mathrm{Re}_{\mathrm{wall}}$ values is felt more here than the pressure curves, similar to the cylinder cases. It is once again encouraging that as the cell sizes decrease, the magnitude of the peak heating rates do indeed march towards the experimental value, to a more significant extent for the stricter temperature clipping strategy ($T_{\mathrm{ghost}} \geq 0.5 \times T_{\mathrm{reference}}$).

The separation location, as seen in the pressure curves, is marginally shifted to the right of the experimental values, but the overall location of the peak convective heating rate

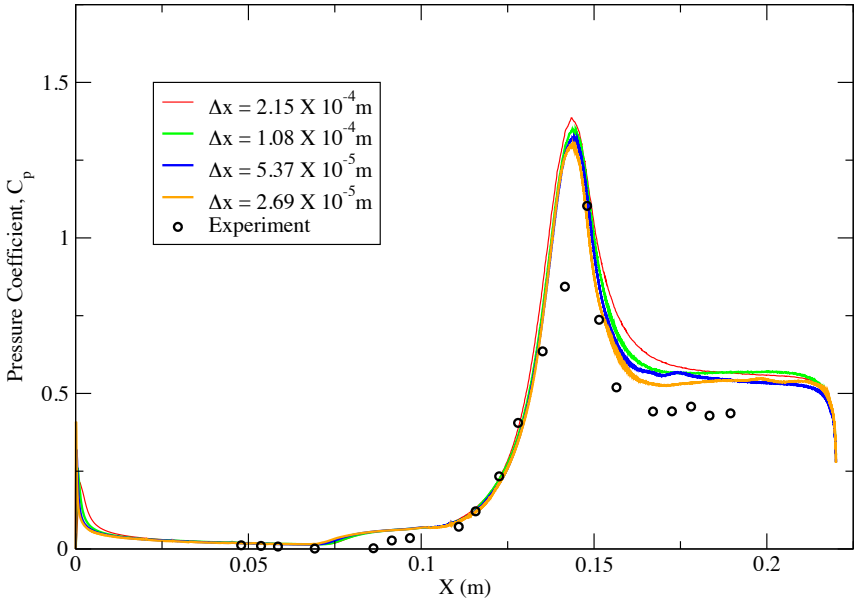

Figure 65: C_p distribution (CUBRC Run 11): [$T_{ghost} \geq 0.5T_{reference}$]

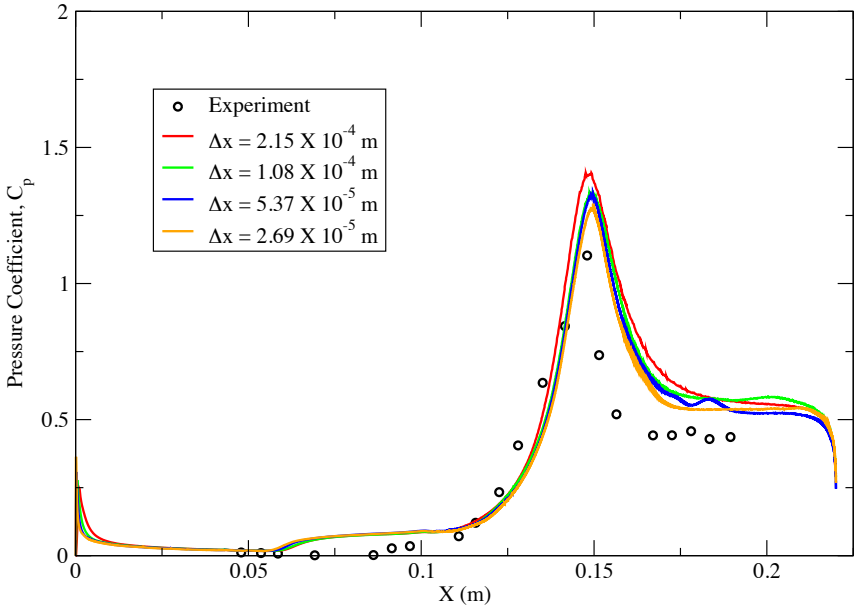

Figure 66: C_p distribution (CUBRC Run 11): [$T_{ghost} \geq 0.25T_{reference}$]

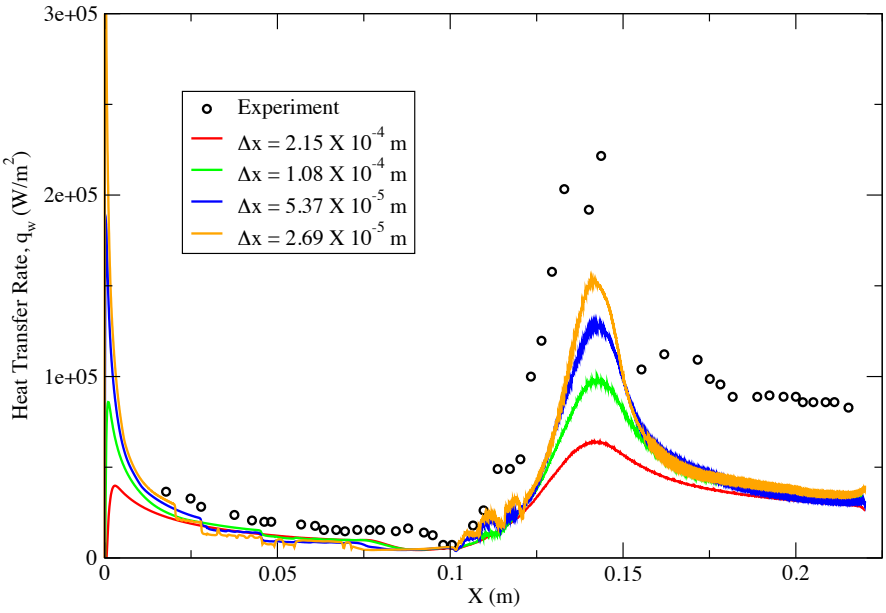

Figure 67: $\dot{q}_w$ distribution (CUBRC Run 11): [$T_{ghost} \geq 0.5T_{reference}$]

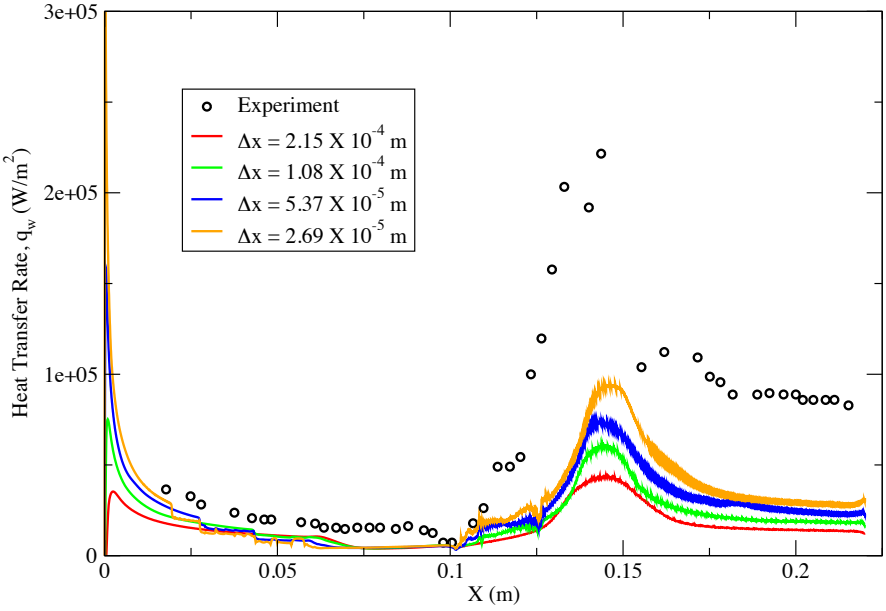

Figure 68: $\dot{q}_w$ distribution (CUBRC Run 11): [$T_{ghost} \geq 0.25T_{reference}$]

compares very well with experiments.

5.2 Inferences: Frozen Simulations

The take-away from this study is that the strategy used to improve the surface predictions of the heat transfer rate and the pressure coefficients has to be specific for each test case analyzed. In this case, as well as the cylinder cases presented in the previous chapter, the immersed boundary method has been shown to be capable of predicting reasonable convective heating trends even with significantly coarse grids (high $\mathrm{Re}_{\mathrm{wall}}$). Also, the clipping strategy that allows for a stricter lower ghost cell temperature limit results in a more stable solution that leads to a smoother variation of the surface properties, compared to the setting that allows for a lower ghost cell temperature.

Even though the stricter clipping strategy ($T_{\mathrm{ghost}} \geq 0.5 \times T_{\mathrm{reference}}$) seems to improve the heating predictions with finer grids, adequate care must be taken to make sure that this does not result in a non-physical representation of the surface temperature. The temperature perceived by the fluid at the boundary is altered in this methodology, and the isothermal wall temperature that is initially set is overridden with the clipped value. Though this strategy lends a certain level of stability to the simulation, it should be noted that the heat transfer rate predicted at the wall would be based on the clipped temperature. Of course, as the surface cells start to refine, the impact of the clipping strategy wanes. Ideally, surface cells should be refined until the temperatures at the ghost cells do not get clipped anywhere at the surface, yielding the most accurate representation of the isothermal surface temperature. Unfortunately, the computational costs associated with successive refinements can be significant. Therefore, it is important to balance the two in deciding upon a simulation strategy. A dynamic adaption strategy mixed with a more robust temperature clipping setting is generally required for good predictions of hypersonic viscous flows.

CHAPTER VI

REACTING FLOW RESULTS

Finally, test cases were setup to evaluate the immersed boundary ghost cell methodology for predicting hypersonic convective heat transfer rates in a reacting environment. These tests serve as preliminary investigations to evaluate the strengths and weaknesses of the immersed boundary ghost cell approach for such a setup.

6.1 Reacting Flow Adiabatic Wall Predictions

6.1.1 Cylinder in Mach 12.7 Air Flow

The off-surface flow physics prediction capability of the Cartesian grid framework in a chemically reacting thermal nonequilibrium environment was first verified using an adiabatic wall boundary condition. A Mach 12.7 air flow test case past a cylinder of radius 0.1 m was considered with the freestream conditions listed in Table 7. In this reacting environment, Re_∞ per unit length was computed to be 355,000 (based on 79% N_2, 21% O_2 at T_∞ 195.96 K). Lee [51] used this test case to evaluate the inviscid thermochemical nonequilibrium capability of the solver. This case has been extended to include viscous effects. Comparisons of the flow predictions were made with the solutions from DPLR. The grids used in both solvers are shown in Figs. 69 and 70.

The inviscid fluxes were computed using the AUSMPW+ scheme, and were set to first

Table 7: Cylinder in Mach 12.7 air flow test conditions

Freestream parameter	Value
M_∞	12.7
ρ_∞	1.6×10^{-3} kg/m^3
P_∞	90 Pa
Re_∞	355,000 /m

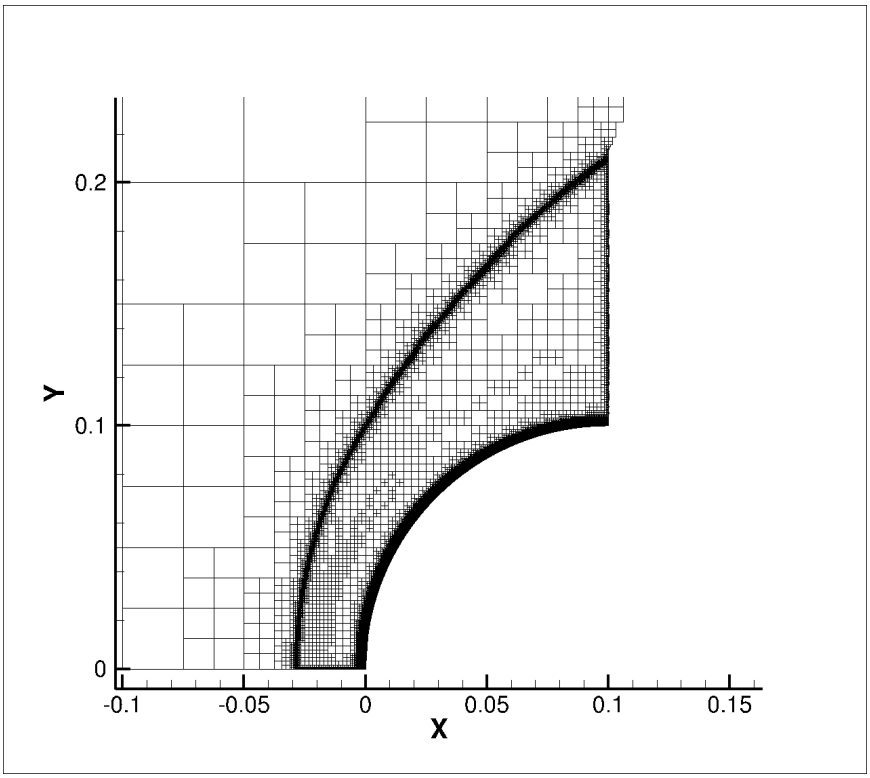

Figure 69: Cylinder in Mach 12.7 air, adiabatic wall: NASCART-GT grid

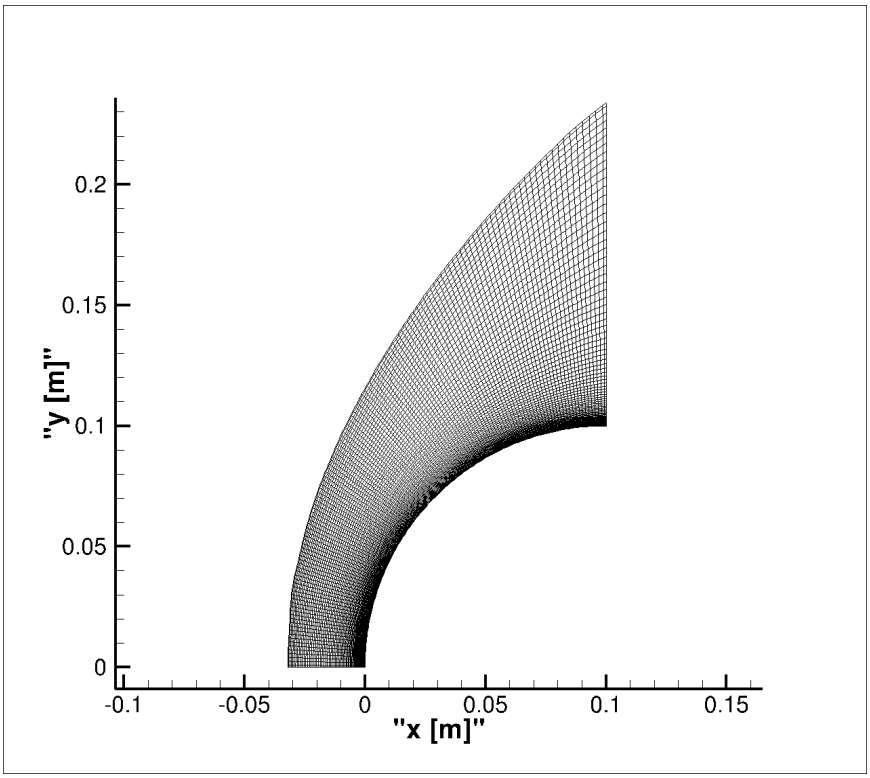

Figure 70: Cylinder in Mach 12.7 air, adiabatic wall: DPLR grid

order accuracy throughout for stability purposes. NASCART-GT automatically sets the order of accuracy of the inviscid fluxes in regions of sharp gradients to first order by use of the flux limiter. Commencing the simulation with a higher order of accuracy led to instabilities in the progression of the solution, as well as fluctuations in the shock region where adjacent cells would compute inviscid fluxes to different orders of accuracy.

This case was run in parallel on 8 cores. The final converged grid had a total of 96,000 cells with the smallest cell size being of the order of 10^{-4} m. Solution adaptation was carried out at regular intervals (every 500 iterations) to ensure that the sharp gradients computed were sufficiently resolved. Gradients of the velocity divergence and the species concentrations were used for the refinement routine for this case. The threshold values for unrefinement based on velocity divergence gradients was set to 30% and for species concentration gradients, it was set to 50% of the average. For refinement, the threshold for both velocity divergence and species concentration gradients were set to the overall average of the respective parameters in the computational domain. The highly refined post-shock region is evidence of the refinement based on concentration gradients, where temperatures of the order of 6000 K result in the chemically reacting air mixture. The air chemistry model was composed of 5-species and 17-reactions, and the forward reaction rates were identical to those used in Ref. [51]. Further, a CFL number-ramping technique was followed to ensure smooth progression of the solution, considering that the chemistry associated with hypersonic flows generally amounts to a stiff problem. The resulting variations in the Mach number, pressure, translational-rotational temperature and vibrational temperature are compared in the form of contours plots with DPLR. These are shown in Figs. 71-78.

The variations in the Mach number and pressure match very well with the results from DPLR, with almost identical contours levels through the computational domain. The shock wave shape and the stand-off distance (0.03 m) also agrees with the body-fitted solver. The marginal variations in the contours near the 90° circumferential angle are attributed to the coarseness of the Cartesian grid in this region. The overall variations of the temperatures also match for this test case, with the vibrational temperature contours differing in thickness in the stagnation region.

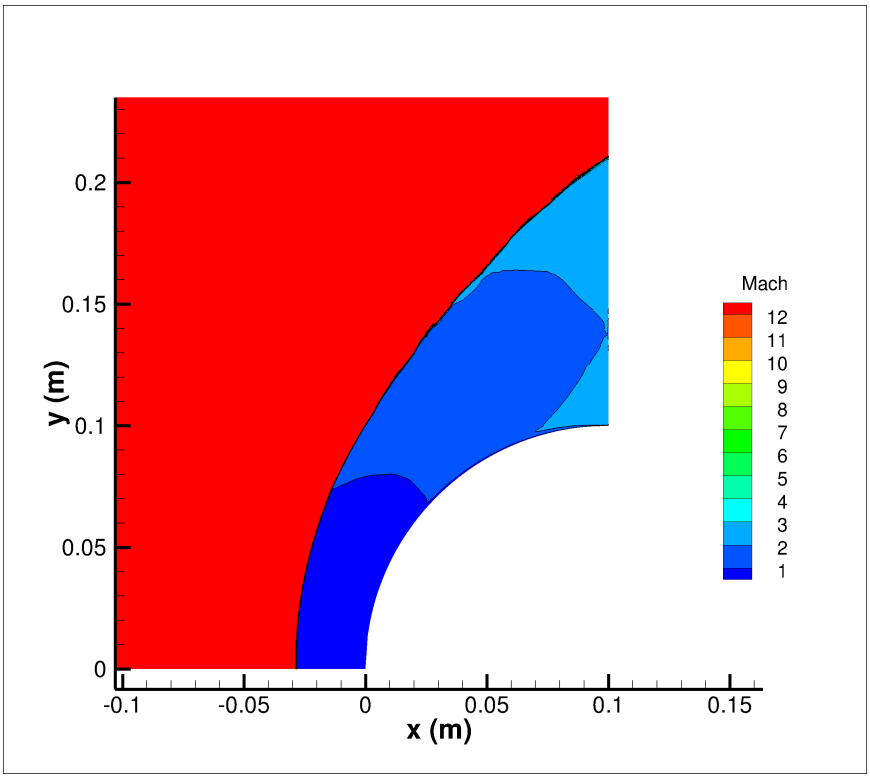

Figure 71: Cylinder in Mach 12.7 air, adiabatic wall: NASCART-GT Mach contours

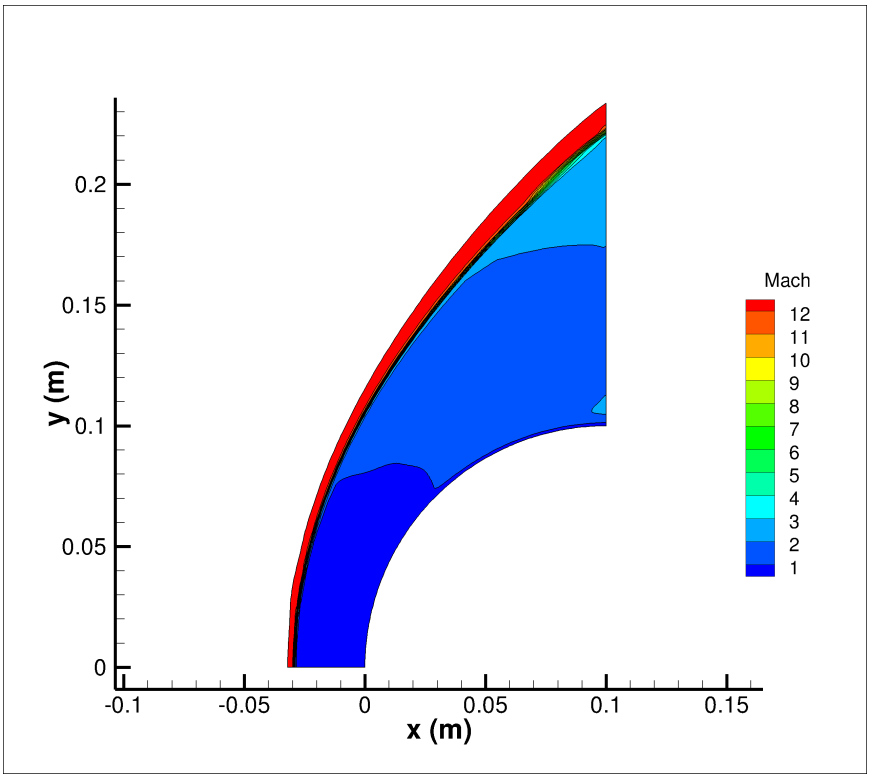

Figure 72: Cylinder in Mach 12.7 air, adiabatic wall: DPLR Mach contours

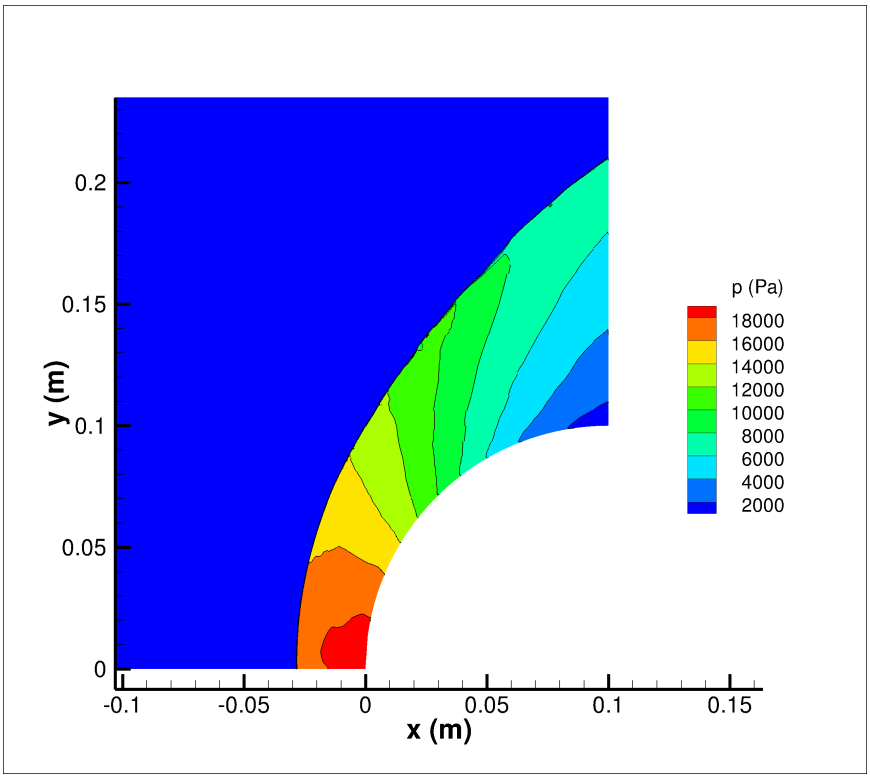

Figure 73: Cylinder in Mach 12.7 air, adiabatic wall: NASCART-GT pressure contours

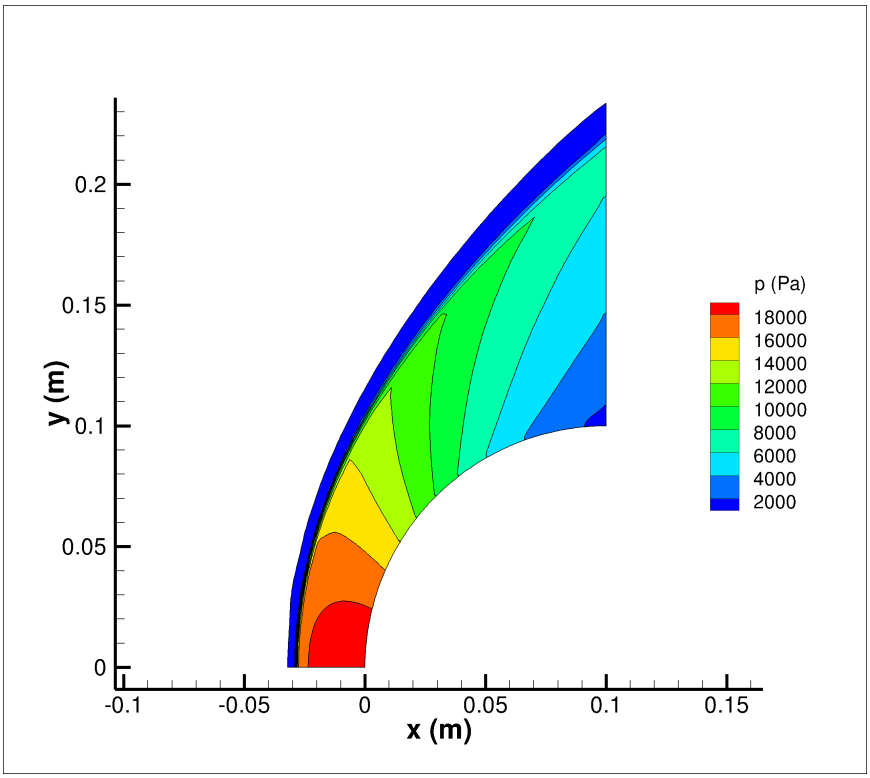

Figure 74: Cylinder in Mach 12.7 air, adiabatic wall: DPLR pressure contours

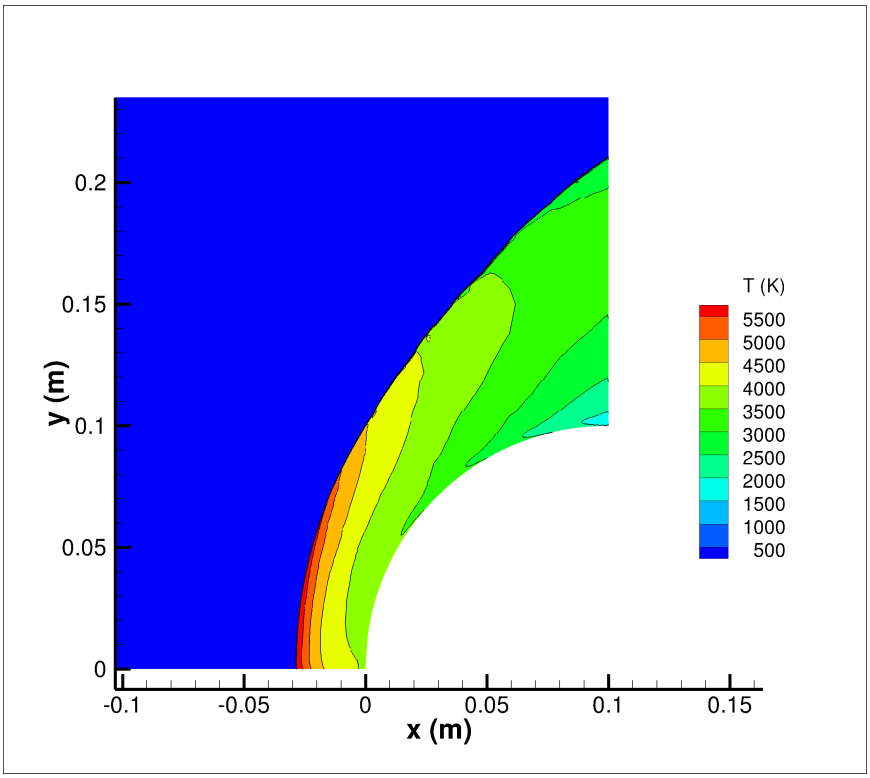

Figure 75: Cylinder in Mach 12.7 air, adiabatic wall: NASCART-GT T_{tr} contours

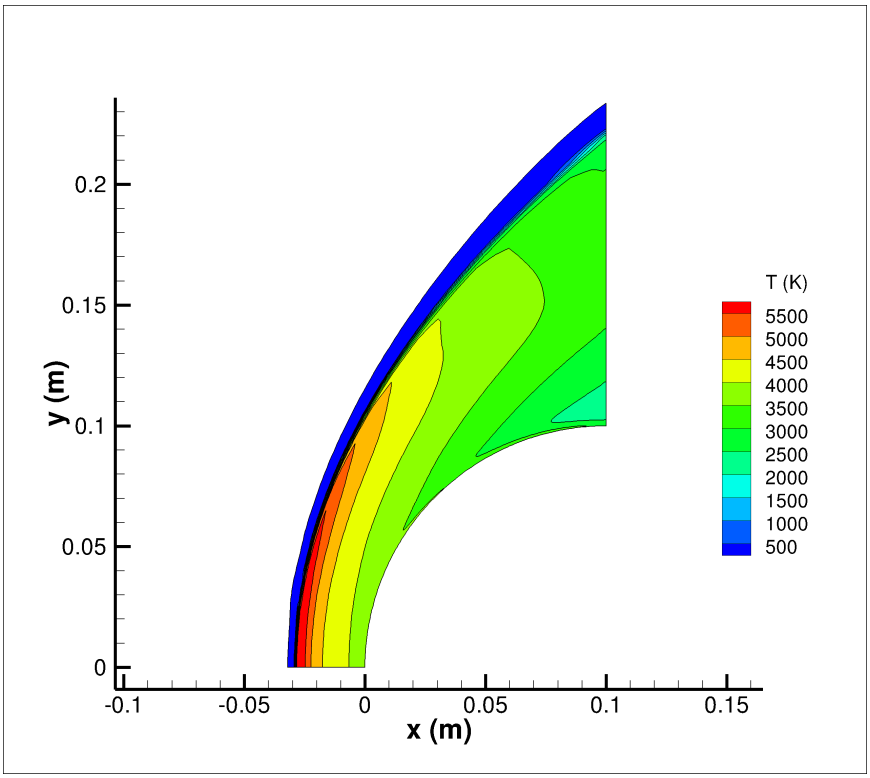

Figure 76: Cylinder in Mach 12.7 air, adiabatic wall: DPLR T_{tr} contours

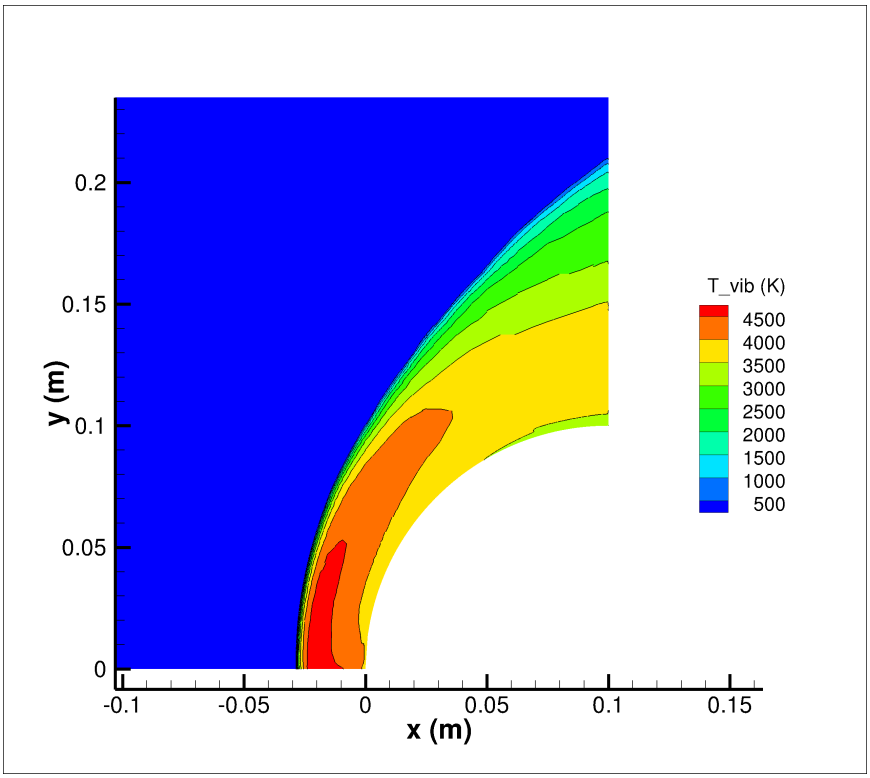

Figure 77: Cylinder in Mach 12.7 air, adiabatic wall: NASCART-GT T_v contours

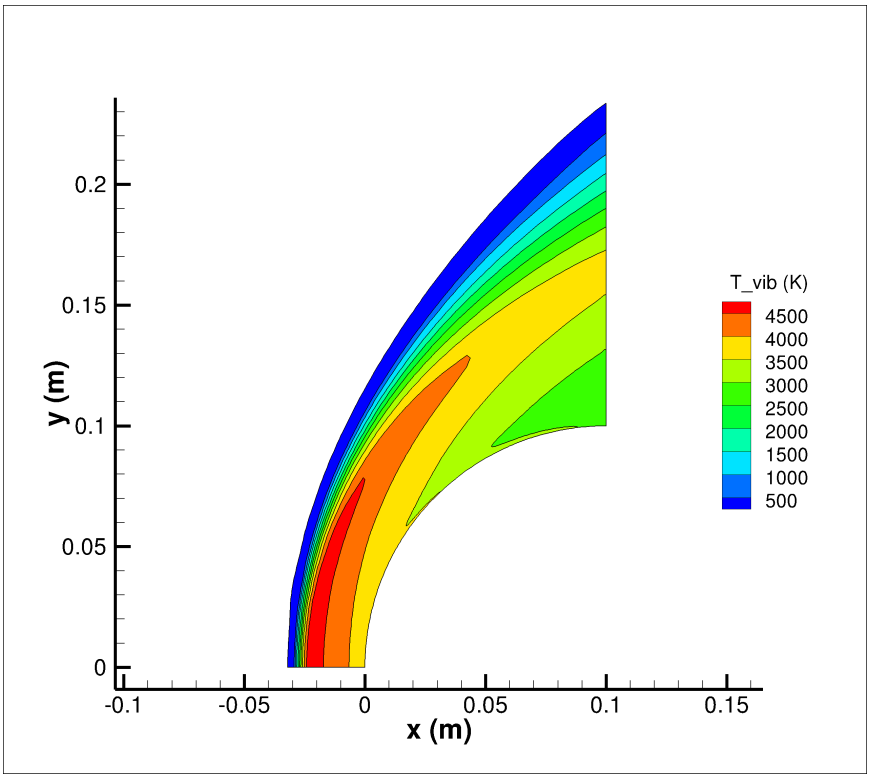

Figure 78: Cylinder in Mach 12.7 air, adiabatic wall: DPLR T_v contours

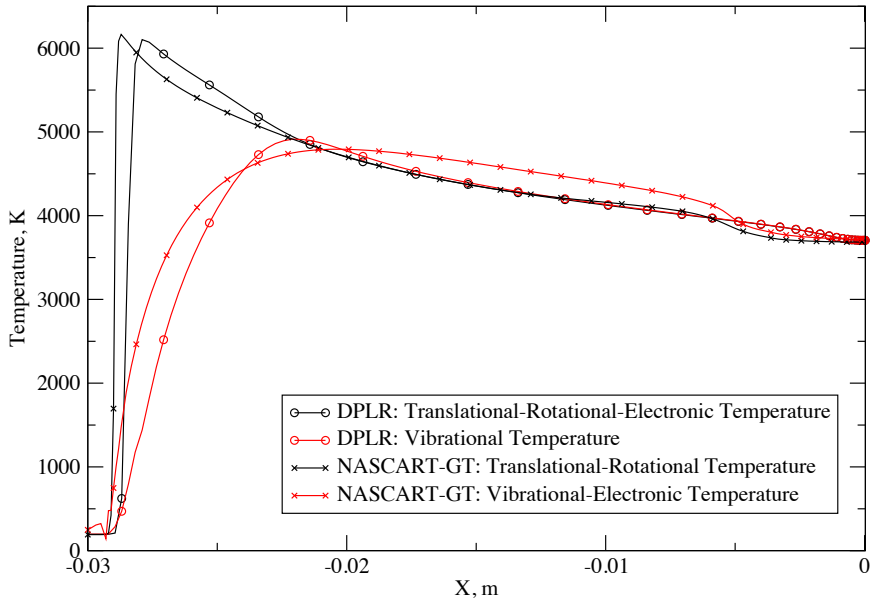

Figure 79: Cylinder in Mach 12.7 air, adiabatic wall: Stagnation line temperatures

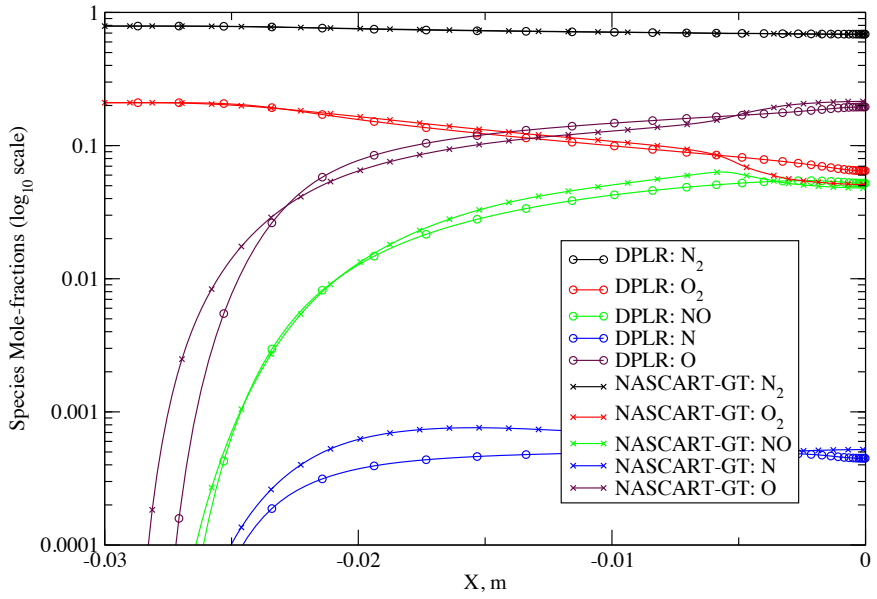

Figure 80: Cylinder in Mach 12.7 air, adiabatic wall: Stagnation line mole-fractions

Table 8: Cylinder in Mach 12.7 air flow test conditions

Freestream parameter	Value
M_∞	12.7
ρ_∞	1.6×10^{-3} kg/m^3
P_∞	90 Pa
T_{wall}	500 K
Re_∞	355,000 /m

Figures 79 and 80 show the variations of the temperatures and the species mole fractions along the stagnation line for this reacting flow test case. The peak translational-rotational temperature from both the solvers is in the vicinity of 6000 K, and the vibrational peak temperature is approximately 4800 K for NASCART-GT, whereas it is around 5000 K for DPLR. This discrepancy is attributed to the difference in the representation of the internal energy modes in each solver. NASCART-GT considers the translational and rotational modes, and the vibrational and electronic modes to be in equilibrium with each other, whereas DPLR assumes a single temperature for the translational-rotational-electronic modes, and a separate temperature for the vibrational mode. Variations of the species mole-fractions along the stagnation line also compare very well (Fig. 80).

6.2 Reacting Flow Isothermal Wall Predictions

6.2.1 Cylinder in Mach 12.7 Air Flow

Having shown excellent prediction capability of the off-surface flow physics for hypersonic chemically reacting flows, the ability to make surface physics predictions was next investigated for an isothermal wall boundary condition. A similar Mach 12.7 air flow test case past a cylinder of radius 0.1 m was considered with the freestream conditions listed in Table 8. This reacting environment had the same Re_∞ per unit length of 355,000 (based on 79% N_2, 21% O_2 at T_∞ 195.96 K). Comparisons of the flow predictions were once again made with the solutions from DPLR. The grids used in both solvers are shown in Figs. 81 and 82.

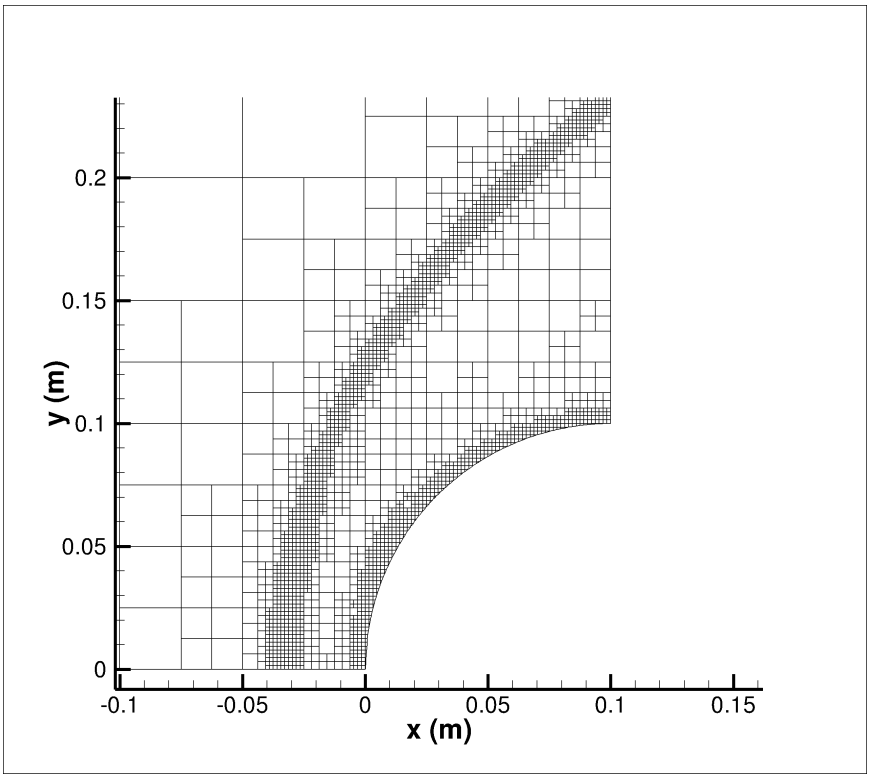

Figure 81: Cylinder in Mach 12.7 air, isothermal wall: NASCART-GT grid

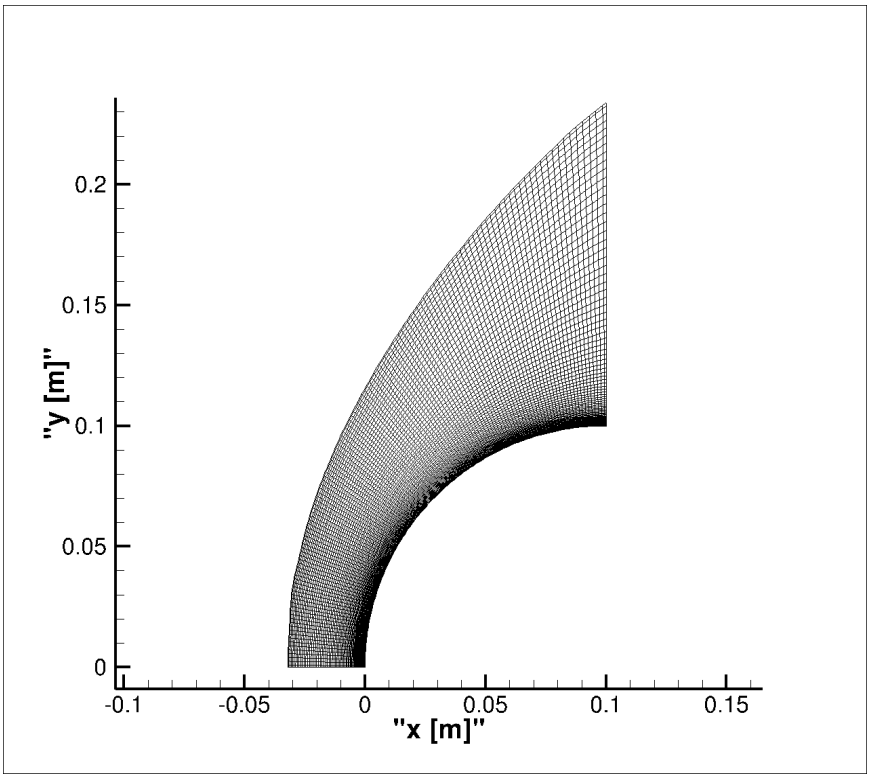

Figure 82: Cylinder in Mach 12.7 air, isothermal wall: DPLR grid

AUSMPW+ scheme was used to compute the inviscid fluxes to second order accuracy. This case was also run in parallel on 8 cores. The final coarse converged grid had a total of 18,000 cells with the smallest cell size being of the order of 10^{-4} m. Gradients of the velocity divergence, species concentrations and temperature were used for the refinement routine for this case. The air chemistry model was composed of 5-species and 17-reactions, and the forward reaction rates were used Park's 1993 model. The resulting variations in the Mach number, pressure, translational-rotational temperature and vibrational temperature are compared in the form of contours plots with DPLR. These are shown in Figs. 83-90.

Variations in the Mach number and pressure match well with the results from DPLR, with almost identical contours levels through the domain. The shock wave shape agrees well with the body-fitted solver, but the shock stand-off distance is over-predicted by approximately 15%. The overall variations of the temperatures also match well for this test case. For example, the peak translation-rotational temperature from both solvers is around 5500 K. However, the smallest grid cell size used in the Cartesian grid solver was 2 orders of magnitude larger than that body-fitted grid solver (10^{-4} m vs 10^{-6} m). The corresponding wall Reynolds number ($\mathrm{Re}_{\mathrm{wall}}$) computed was around 4,000. This is significantly larger than the prescribed value of $\mathcal{O}(1)$. Therefore, the thermal boundary layer was poorly resolved, which lead to a significant under-prediction of the stagnation point heating rate (7.3×10^4 W/m^2 vs 6.3×10^5 W/m^2). Finer meshes are definitely required to make good heating predictions with a well resolved thermal boundary layer.

Overall, the immersed boundary method in the unstructured Cartesian grid framework has been shown to compute viscous chemically reacting hypersonic flows. However, for reasonable accuracy, the grid cell spacing in the normal direction must be similar to the requirements for body-fitted grids. Since the Cartesian formulation uses cell aspect ratios of unity (unlike body-fitted grids), achieving grid densities suitable for adequate heat transfer for high Reynolds number problems such as this case make the pure Cartesian formulation less attractive.

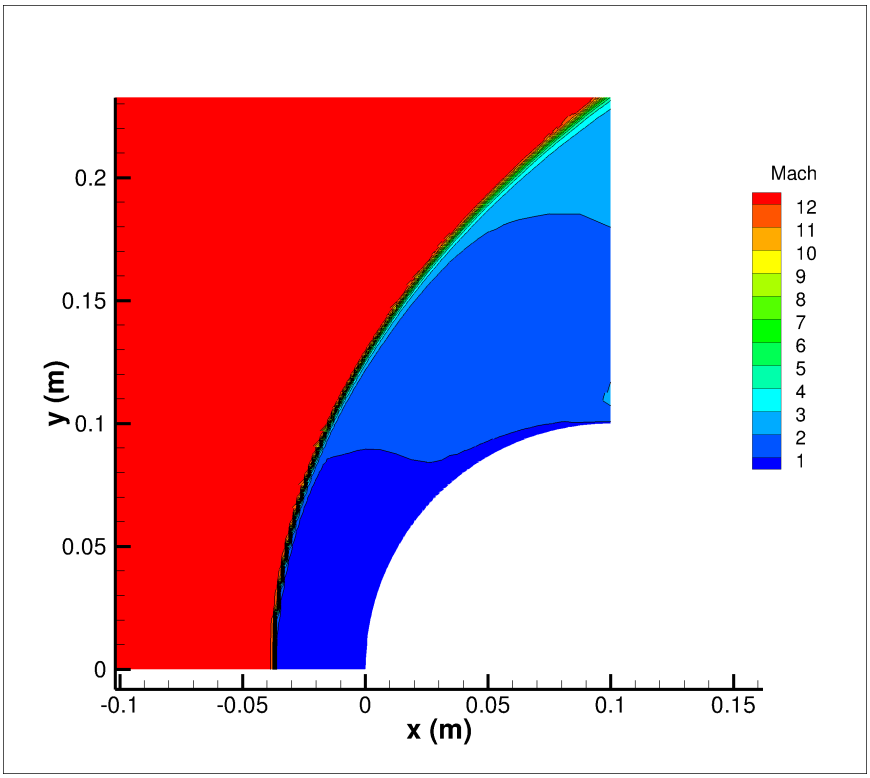

Figure 83: Cylinder in Mach 12.7 air, isothermal wall: NASCART-GT Mach contours

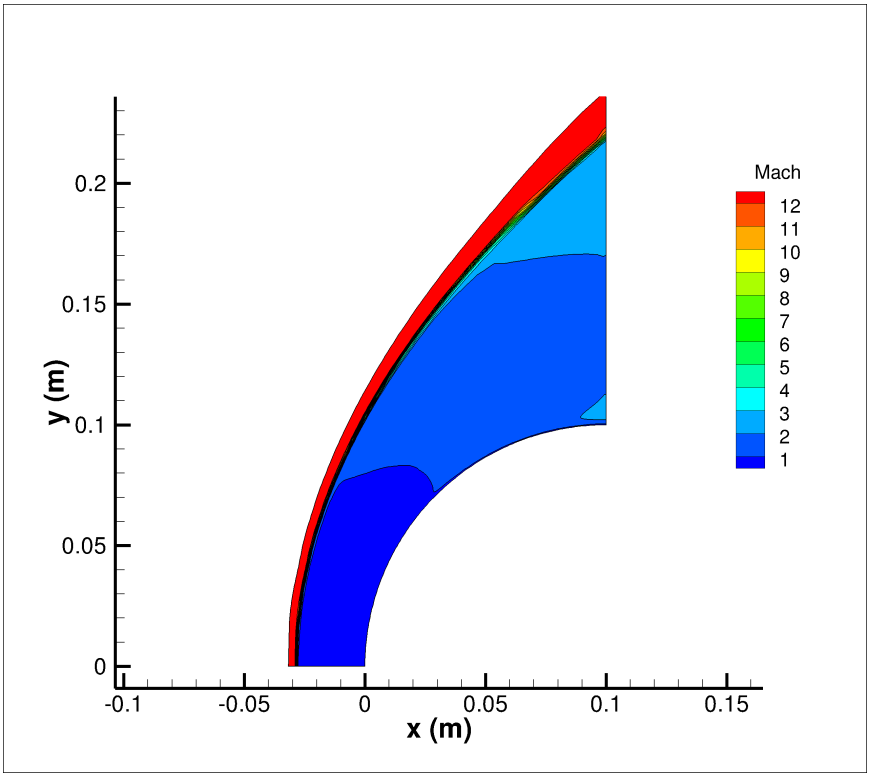

Figure 84: Cylinder in Mach 12.7 air, isothermal wall: DPLR Mach contours

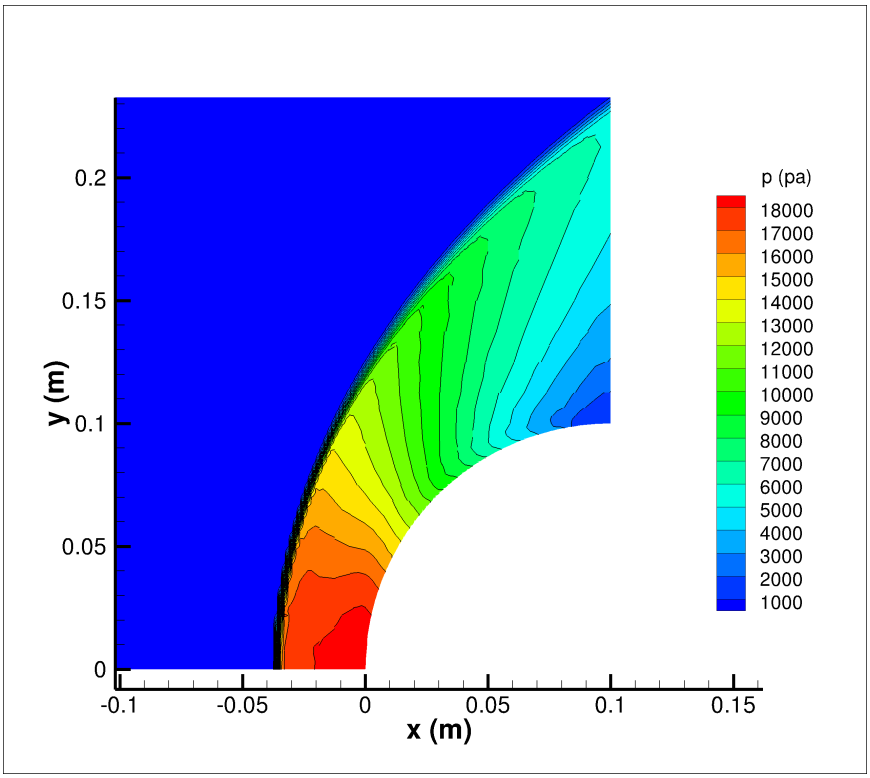

Figure 85: Cylinder in Mach 12.7 air, isothermal wall: NASCART-GT pressure contours

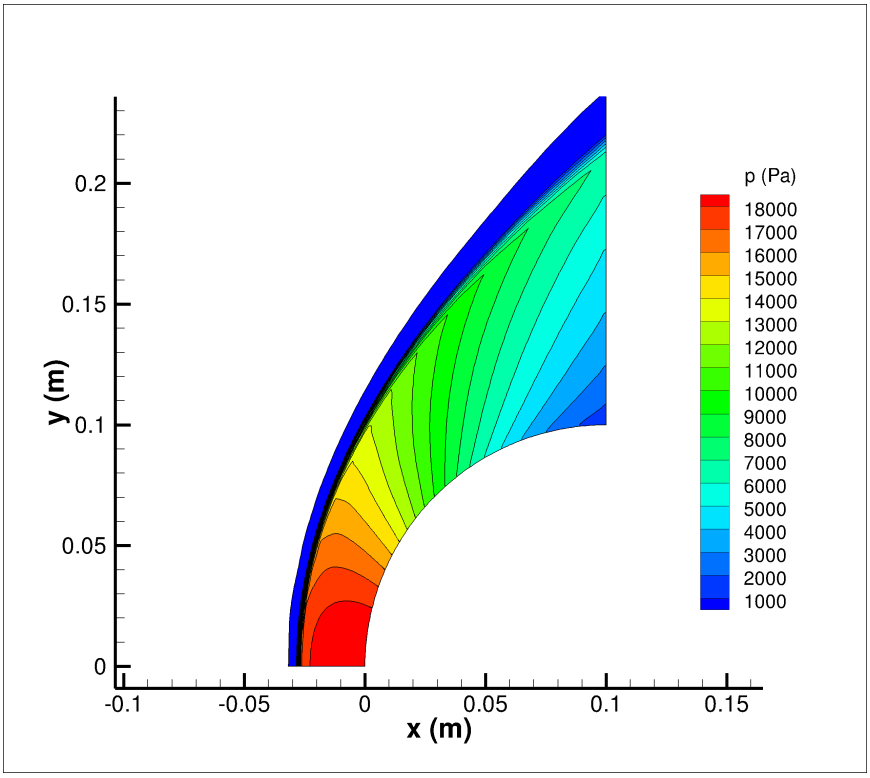

Figure 86: Cylinder in Mach 12.7 air, isothermal wall: DPLR pressure contours

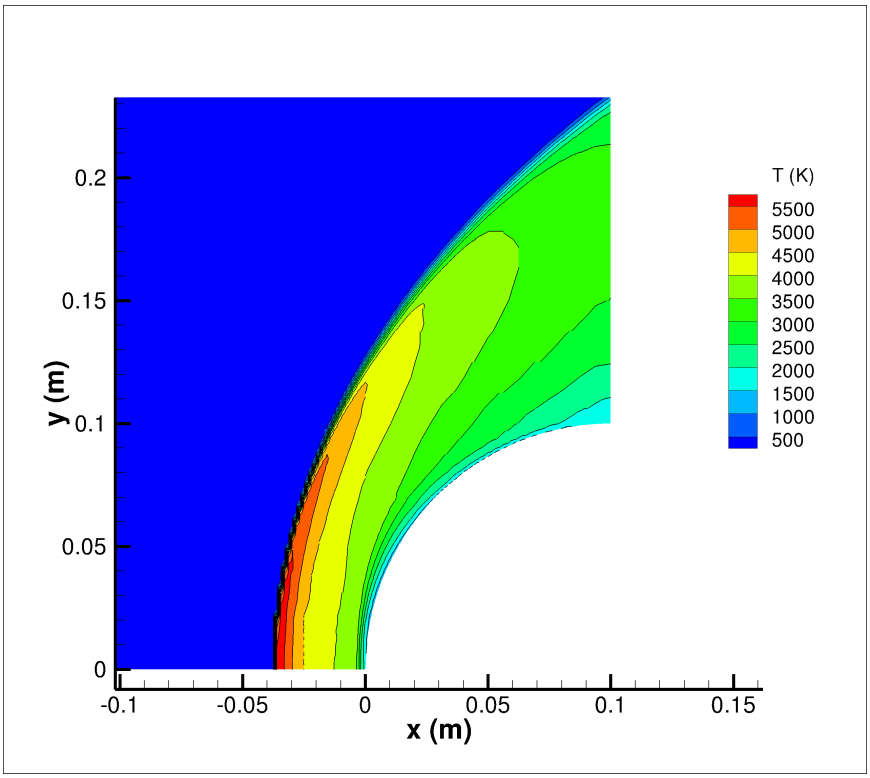

Figure 87: Cylinder in Mach 12.7 air, isothermal wall: NASCART-GT T_{tr} contours

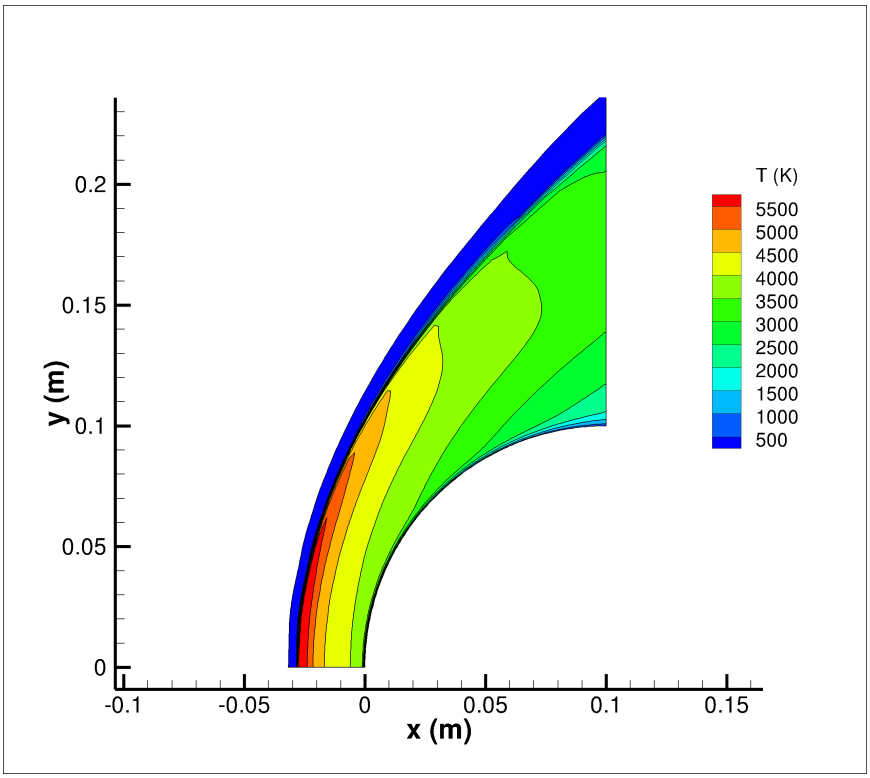

Figure 88: Cylinder in Mach 12.7 air, isothermal wall: DPLR T_{tr} contours

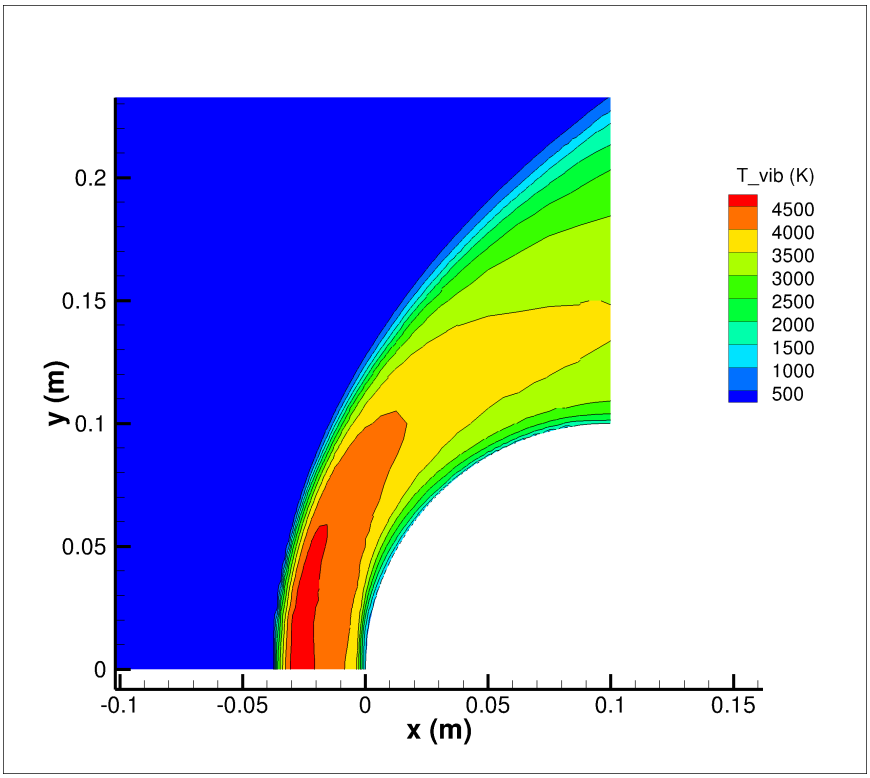

Figure 89: Cylinder in Mach 12.7 air, isothermal wall: NASCART-GT T_v contours

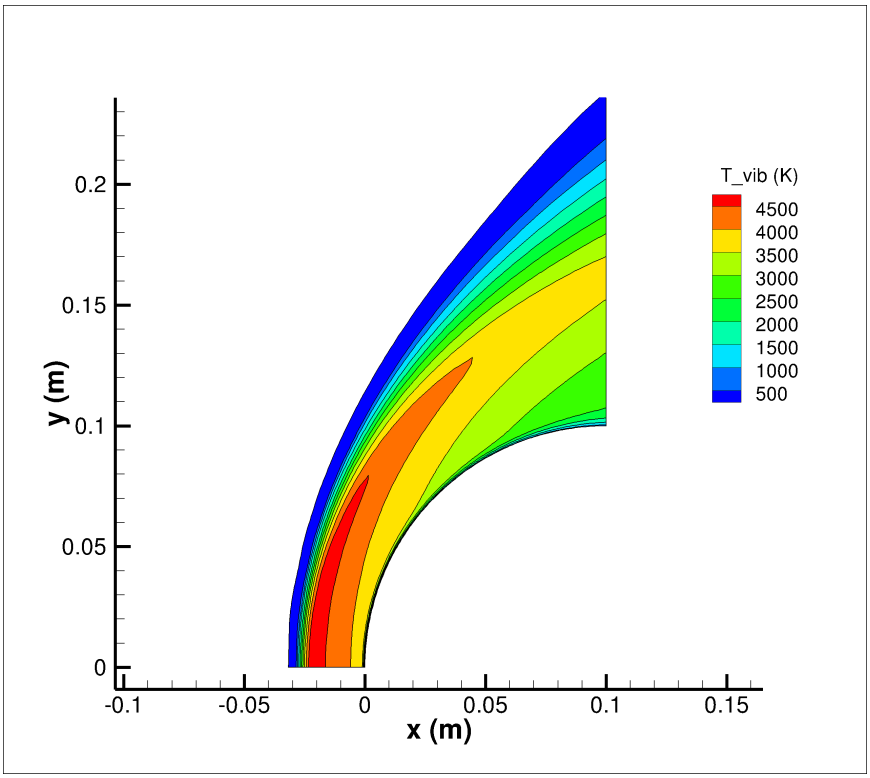

Figure 90: Cylinder in Mach 12.7 air, isothermal wall: DPLR T_v contours

CHAPTER VII

CONCLUSIONS AND RECOMMENDATIONS

7.1 Conclusions

This research study has advanced and demonstrated the ability of the unstructured Cartesian grid based formulations to model hypersonic viscous flows. A solution adaptive solver that utilizes the immersed boundary ghost cell approach was used as the base, and various aspects of this Cartesian grid framework were parameterized for good flow prediction capability. These include the grid cell size, which has been defined based on the $\mathrm{Re}_{\mathrm{wall}}$ magnitudes. The appropriate levels of this parameter for adequate heating predictions has been quantified. The criteria used in the adaptive mesh refinement process were extended to included appropriate parameters for good heating predictions. The impact of a viscous-band of surface cells on the quality of the predictions was also demonstrated.

Additionally, thermochemical nonequilibrium capability was integrated to the immersed boundary Cartesian framework, allowing for the computation of hypersonic, reacting flows. The strengths and shortcomings of this technique in predicting off-surface and surface flow properties have been recorded, and this first-of-a-kind implementation extends the state-of-the-art in unstructured Cartesian grid techniques, laying the groundwork for further research in this field. The specific outcomes of the research effort are detailed below.

Comparisons of the variations of surface pressure, shear stress and convective heat flux predicted for a Mach 10 flow of argon past a 12" cylinder for a set of Reynolds numbers were made with results from a DSMC code (MONACO) and a body-fitted grid CFD simulation (LeMANS). The overall trends in all the parameters compared well, and the accuracy of the predictions were evaluated at various grid refinement levels. The sensitivity of the accuracy of these predictions to $\mathrm{Re}_{\mathrm{wall}}$ was documented for this series of test cases. The pressure coefficient variation along the surface was largely unaffected by the relative coarseness of the grid cells in the preliminary test runs, and compared well with the results from the

reference for all $\mathrm{Re}_{\mathrm{wall}}$ values. The skin friction coefficient and the convective heat transfer rate were more sensitive to the size of the surface cells in each case. $\mathrm{Re}_{\mathrm{wall}}$ magnitudes of $\mathcal{O}(1)$ showed very good agreement with the reference distributions, whereas cell sizes of $\mathcal{O}(10)$ fared much worse in comparison. The magnitude of the peak heating was reasonably predicted in each case, whereas for coarse grids the trends of the shear stress and the heat flux across the surface showed significant deviations from the reference values. Further, a correlation between the conformity of the surface property variations to the references values and the grids used in these simulations was made. The extent to which the band of viscous grid cells spread into the high temperature bubble in the stagnation region tended to have a significant impact on the accuracy and the trend of the properties along the surface.

The noise associated with the skin friction and convective heating curves is attributed to the variations in the orientation and location of the surface panels along the body, which results in a non-uniform distribution of the ghost cell center distances from the surface panels. Additionally, the reference point locations with respect to 3 closest surrounding cell centers also affected the interpolated values there, further increasing the noise associated with these distributions.

To demonstrate the advantages of the unstructured Cartesian grids in adapting themselves to capture complex flow physics, a hypersonic test case that involved interactions between a shock wave and a boundary layer, and a separation bubble was computed. Comparisons of the surface pressure coefficient and the heating rates for an axisymmetric hollow cylinder-flare configuration was made with experimental results, and the effects of the temperature clipping strategy used in the immersed boundary ghost cell approach was analyzed for 2 different clipping limits. Overall, the formulation made good predictions of the major flow features with very good agreement in the locations of the shock wave/boundary layer interaction and the re-circulation bubble. Also, given the high freestream Reynolds numbers and taking into account the costs of such simulations (with excessive number of cells), only reasonably coarse grids were tested in this research effort. Despite this restriction, the overall trend of the surface property predictions agreed well with the experimental results, and showed significant improvement in the heating predictions with successively refined

grids. Additionally, the clipping strategy that restricted the ghost cell temperatures from falling below 1/2 the reference cell temperatures made much better predictions compared to the setup that allowed the minimum ghost cell temperature to 1/4 the reference cell value.

Further, to confirm the immersed boundary method's convective heating prediction capability, a range of freestream Mach numbers were chosen and the overall trend of the stagnation point heating was compared with results from a ballistic range experimental setup and tried-and-tested empirical relations for an axisymmetric hemisphere.

Finally, the existing inviscid thermochemical nonequilibrium solver in NASCART-GT was extended to compute viscous flows by installing diffusion terms in the species and energy conservation equations. Collision cross-section based transport coefficients were also included to compute viscosity, thermal conductivity and the species diffusion coefficients. Appropriate modifications were made to the immersed boundary ghost cell approach for a reacting environment.

The unstructured Cartesian grid framework was first tested for an adiabatic wall boundary condition to evaluate its ability to make good estimates of the off-surface flow properties. A 2-D cylinder test case for hypersonic reacting air flow was computed, and the results were compared with those from a body-fitted grid solver (DPLR). Very good agreement of the flow properties in the computational domain were seen, with identical shock wave stand-off distances predicted by both solvers. The temperatures and species mole-fractions variations along the stagnation line also compared very well for this test case.

Next, a similar 2-D cylinder test case for hypersonic reacting flow was computed using an isothermal wall boundary condition to evaluate the surface properties prediction capability of the immersed boundary method. Comparisons of the results were once again made with results from DPLR. The grid cells used in this analysis were coarse due to the associated computational costs. Even with such a grid, the shock stand-off distance, the peak temperatures in the computational domain and the shock shape compared reasonably well with the reference. The stagnation point heating rate in this thermochemical nonequilibrium environment was significantly under-predicted by the solver when compared to the reference value. The combination of a higher order flux-integration scheme with finer grid

cells should allow for better agreement with experiment.

Based on the results of this research study, it was found that to make accurate predictions of convective heating using the immersed boundary method, cell sizes that correspond to a $\mathrm{Re}_{\mathrm{wall}}$ of $\mathcal{O}(1)$ are required. This results in a very large number of cells in the computational domain even for 2-D cases, increasing the cost of such test runs. For higher freestream Reynolds numbers, this number gets even higher, and could become prohibitively large for 3-D geometries.

7.2 Recommendations

Considering that this is the first such research study into the prediction capability of the immersed boundary ghost cell methodology in an unstructured Cartesian framework for viscous thermochemical nonequilibrium flows, a number of strengths and shortcomings of the formulation were observed. For instance, the prediction of the pressure distribution along the surface of the geometry could be made with coarse grid cells, whereas the skin friction and heating rates required much finer cells to make accurate predictions. Additionally, the unstructured Cartesian framework makes very good predictions of the off-surface properties even in a thermochemical nonequilibrium environment. Based on these observations, a series of recommendations are made to improve the accuracy and smoothness of the surface properties, keeping in mind the cost associated with these simulations.

Alternative gridding strategies

With the stringent $\mathrm{Re}_{\mathrm{wall}}$ requirement for accurate heating predictions for hypersonic flows, the use of the immersed boundary ghost cell approach in the unstructured Cartesian methodology has been shown to require a very large number of cells to make good predictions of surface properties. Given the cost of such simulations, the practical application of this technique in a high Reynolds number reacting flow environment using the current framework requires significant modifications. Alternative discretization strategies must be investigated. The combination of a body-fitted mesh at the surface and an unstructured Cartesian mesh in the far-stream is one such strategy. This will alleviate the need for a prohibitively large number of Cartesian unstructured

grid cells at the surface, and still allow for the accurate capture of the off-surface flow physics with the adaptive mesh refinement capability. Additional strategies, such as the normal ray refinement technique [82], could also be used in reducing the number of surface cells, thereby the costs of such computations.

Immersed boundary ghost cell - temperature BC

Preliminary analyses of various temperature boundary conditions were carried out at the beginning of this investigation, and the most stable from a series of implementations was chosen for the presented results. Further research into other temperature boundary conditions could relax the stringent $\mathrm{Re}_{\mathrm{wall}}$ restriction that this implementation imposes. For example, a setup where the ghost cell temperature is split into viscous and inviscid components was tested, and showed reasonably accurate predictions of the heating rates even for coarser surface cells. Here, the inviscid flux terms used an adiabatic wall temperature boundary condition ($\mathrm{T}_{\mathrm{ghost}} = \mathrm{T}_{\mathrm{reference}}$), whereas the viscous flux terms used an unclipped ghost cell center temperature. Since the viscous flux calculations only require temperature gradients at the cell faces, this viscous temperature was allowed to take even negative values, ensuring the correct gradient at the wall. Though the magnitude of the stagnation point heating was computed well, this strategy was not considered in this study because the variation of the convective heating rate along the surface of the geometry was found to be very noisy. Such an alternative implementation of the temperature setting in the immersed boundary method could very well be used to reduce the number of surface cells, allowing for less expensive simulations.

Parallel setup, finer grid simulations

To further improve the simulation cost for such computationally intensive test cases, it is critical to have a parallelized solver that allows for very efficient scalability. Even though NASCART-GT is capable of parallel test runs, the efficiency of its parallel implementation must be investigated.

Unify implicit formulation

Currently, NASCART-GT separates the LU-SSOR scheme that integrates the initial five terms of the state vector from the chemistry terms, which are computed using the point-implicit solver. Further investigation into the efficiency of such a setup is required, and the chemistry terms of the Jacobian formulation of the LU-SSOR scheme must be installed.

Thermo-chemistry implementation

The thermal nonequilibrium model in NASCART-GT allows for the presence of 2 separate temperatures in the flow. This should be extended to allow for multiple vibrational temperature, as well as ionization. Of course, appropriate empirical curve fits must also be included in the available database. Additionally, wall boundary conditions that allow for various levels of catalycity must be included.

APPENDIX A

CONSERVATION EQUATIONS: VECTOR FORM

The conservation equations presented Chapter 2 are organized in the form of an equation of vectors to distinguish the inviscid and viscous terms, as well as the source terms. In Chapter 3, the flux terms along the Cartesian **X**- direction alone were presented. For the sake of completeness, the terms along all three dimensions are presented here.

Once again, the vector form of the governing equations are:

$$\frac{\partial \mathbf{U}}{\partial t} + \frac{\partial \left(\mathbf{F} - \mathbf{F_v}\right)}{\partial x} + \frac{\partial \left(\mathbf{G} - \mathbf{G_v}\right)}{\partial y} + \frac{\partial \left(\mathbf{H} - \mathbf{H_v}\right)}{\partial z} = \mathbf{S} \tag{99}$$

U is the vector of conserved state variables, **F**, **G** and **H** are the inviscid flux vectors along the Cartesian **X**-, **Y**- and **Z**- directions respectively, $\mathbf{F_v}$, $\mathbf{G_v}$ and $\mathbf{H_v}$ are their viscous counterparts, and **S** is the vector of source terms due to chemical reactions. Each of these vectors can be expanded as:

$$\mathbf{U} = \begin{bmatrix} \rho \\ \rho u \\ \rho v \\ \rho w \\ \rho e \\ \rho_1 \\ \vdots \\ \rho_{N_s} \\ \rho e_V \end{bmatrix} \qquad \mathbf{S} = \begin{bmatrix} 0 \\ 0 \\ 0 \\ 0 \\ 0 \\ \dot{\omega}_s \\ \vdots \\ \dot{\omega}_{N_s} \\ \dot{\omega}_V \end{bmatrix} \tag{100}$$

The flux vectors are expanded as

$$\mathbf{F} = \begin{bmatrix} \rho u \\ \rho u^2 + p \\ \rho v u \\ \rho w u \\ \rho \left(e + p\right) u \\ \rho_1 u \\ \vdots \\ \rho_{N_s} u \\ \rho e_V u \end{bmatrix} \qquad \mathbf{F_v} = \begin{bmatrix} 0 \\ \tau_{xx} \\ \tau_{xy} \\ \tau_{xz} \\ \tau_{xx} u + \tau_{xy} v + \tau_{xz} w - \left(q_{TR,x} + q_{V,x}\right) - \sum \rho_s h_s u_{D,s} \\ \rho_1 u_{D,1} \\ \vdots \\ \rho_{N_s} u_{D,N_s} \\ -q_{V,x} - \sum \rho_s e_V u_{D,s} \end{bmatrix}$$

$$\mathbf{G} = \begin{bmatrix} \rho v \\ \rho u v \\ \rho v^2 + p \\ \rho w v \\ \rho \left(e + p\right) v \\ \rho_1 v \\ \vdots \\ \rho_{N_s} v \\ \rho e_V v \end{bmatrix} \qquad \mathbf{G_v} = \begin{bmatrix} 0 \\ \tau_{yx} \\ \tau_{yy} \\ \tau_{yz} \\ \tau_{yx} u + \tau_{yy} v + \tau_{yz} w - \left(q_{TR,y} + q_{V,y}\right) - \sum \rho_s h_s v_{D,s} \\ \rho_1 v_{D,1} \\ \vdots \\ \rho_{N_s} v_{D,N_s} \\ -q_{V,y} - \sum \rho_s e_V v_{D,s} \end{bmatrix} \tag{101}$$

$$\mathbf{H} = \begin{bmatrix} \rho w \\ \rho u w \\ \rho v w \\ \rho w^2 + p \\ \rho \left(e + p \right) w \\ \rho_1 w \\ \vdots \\ \rho_{N_s} w \\ \rho e_V w \end{bmatrix} \qquad \mathbf{G_v} = \begin{bmatrix} 0 \\ \tau_{zx} \\ \tau_{zy} \\ \tau_{zz} \\ \tau_{zx} u + \tau_{zy} v + \tau_{zz} w - \left(q_{TR,z} + q_{V,z} \right) - \sum \rho_s h_s w_{D,s} \\ \rho_1 w_{D,1} \\ \vdots \\ \rho_{N_s} w_{D,N_s} \\ -q_{V,z} - \sum \rho_s e_V w_{D,s} \end{bmatrix}$$

APPENDIX B

NON-DIMENSIONALIZED EQUATIONS

NASCART-GT computes the Navier-Stokes equations in their non-dimensional form. In light of the viscous diffusion terms being added to the energy and species density equations, the non-dimensionalization of the entire set of equations is revisited here. This follows the factorization presented in Ref. [92].

The nomenclature used here is the same as in Chapter 2 of this thesis. Terms with superscript "*" denote non-dimensional terms, and subscript "$_\infty$" represents freestream conditions.

From Ref. [92], the primitive variables are non-dimensionalized as:

$$x^{*i} = \frac{x^i}{L} \qquad u^{*i} = \frac{u^i}{V_\infty} \qquad t^* = \frac{t}{L/V_\infty} \tag{102}$$

$$\rho^* = \frac{\rho}{\rho_\infty} \qquad T^* = \frac{T}{T_\infty} \qquad p^* = \frac{p}{\rho_\infty V_\infty^2} \tag{103}$$

$$e^* = \frac{e}{V_\infty^2} \qquad h^* = \frac{h}{V_\infty^2} \qquad \mu^* = \frac{\mu}{\mu_\infty} \tag{104}$$

The non-dimensionalization setup shown above is for the basic Navier-Stokes equations. For flows in thermochemical nonequilibrium, additional diffusion terms due to chemical reactions and multi-temperature environments require the extension of these to accommodate for more complex physics and chemistry terms. Since the non-dimensionalization factors for thermal conductivities (K_{tr} and K_v) and the species diffusion coefficients (D_s) are not explicitly given in the reference, these (K_{ND} and D_{ND}) are derived in terms of the remaining freestream values here. Thus, the equations presented in Chapter 2 can be rewritten in terms of the non-dimensional and freestream terms as:

$$\frac{\partial \rho^*}{\partial t^*}\left\{\frac{\rho_\infty}{L/V_\infty}\right\} + \frac{\partial}{\partial x^{*i}}\rho^* u^{*i}\left\{\frac{1}{L}\rho_\infty V_\infty\right\} = 0 \tag{105}$$

$$\frac{\partial}{\partial t^*}\rho^* u^{*j}\left\{\frac{1}{L/V_\infty}\rho_\infty V_\infty\right\} + \frac{\partial}{\partial x^{*i}}\rho^* u^{*j} u^{*i}\left\{\frac{1}{L}\rho_\infty V_\infty^2\right\} + \frac{\partial p^*}{\partial x^{*j}}\left\{\frac{\rho_\infty V_\infty^2}{L}\right\} = \frac{\partial}{\partial x^{*i}}\left[\mu^*\left(\frac{\partial u^{*j}}{\partial x^{*i}} + \frac{\partial u^{*i}}{\partial x^{*j}}\right) - \frac{2}{3}\mu^*\frac{\partial u^{*k}}{\partial x^{*k}}\delta^{ij}\right]\left\{\frac{1}{L}\mu_\infty\frac{V_\infty}{L}\right\} \tag{106}$$

$$\frac{\partial}{\partial t^*}\rho^* e^*\left\{\frac{1}{L/V_\infty}\rho_\infty V_\infty^2\right\} + \frac{\partial}{\partial x^{*i}}\rho^*\left(e^* + \frac{p^*}{\rho^*}\right)u^{*i}\left\{\frac{1}{L}\rho_\infty V_\infty^2 V_\infty\right\} = \frac{\partial}{\partial x^{*i}}\left(K_{tr}^*\frac{\partial T_{tr}^*}{\partial x^{*i}} + K_v^*\frac{\partial T_v^*}{\partial x^{*i}}\right)\left\{\frac{1}{L}K_{\mathrm{ND}}\frac{T_\infty}{L}\right\} + \frac{\partial}{\partial x^{*i}}\left(\rho^*\sum h_s^* D_s^*\frac{\partial \chi_s}{\partial x^{*i}}\right)\left\{\frac{1}{L}\rho_\infty V_\infty^2 D_{\mathrm{ND}}\frac{1}{L}\right\} + \frac{\partial}{\partial x^{*i}}\left[u^{*j}\mu^*\left(\frac{\partial u^{*j}}{\partial x^{*i}} + \frac{\partial u^{*i}}{\partial x^{*j}}\right) - u^{*j}\frac{2}{3}\mu^*\frac{\partial u^{*k}}{\partial x^{*k}}\delta^{ij}\right]\left\{\frac{1}{L}V_\infty\mu_\infty\frac{V_\infty}{L}\right\} \tag{107}$$

$$\frac{\partial \rho_s^*}{\partial t^*}\left\{\frac{\rho_\infty}{L/V_\infty}\right\} + \frac{\partial}{\partial x^{*i}}\rho_s^* u^{*i}\left\{\frac{1}{L}\rho_\infty V_\infty\right\} = \frac{\partial}{\partial x^{*i}}\left(\rho^* D_s^*\frac{\partial \chi_s}{\partial x^{*i}}\right)\left\{\frac{1}{L}\rho_\infty D_{\mathrm{ND}}\frac{1}{L}\right\} + \{\dot{\omega}_s\}^* \tag{108}$$

$$\frac{\partial}{\partial t^*}\rho e_v^*\left\{\frac{1}{L/V_\infty}\rho_\infty V_\infty^2\right\} + \frac{\partial}{\partial x^{*i}}\rho^* e_v^* u^{*i}\left\{\frac{1}{L}\rho_\infty V_\infty^2 V_\infty\right\} = \frac{\partial}{\partial x^{*i}}\left(K_v^*\frac{\partial T_v^*}{\partial x^{*i}}\right)\left\{\frac{1}{L}K_{\mathrm{ND}}\frac{T_\infty}{L}\right\} + \frac{\partial}{\partial x^{*i}}\left(\rho^*\sum h_{v,s}^* D_s^*\frac{\partial \chi_s}{\partial x^{*i}}\right)\left\{\frac{1}{L}\rho_\infty V_\infty^2 D_{\mathrm{ND}}\frac{1}{L}\right\} + \sum\left\{\rho_s\frac{e_{v,s}^* - e_{v,s}}{\langle\tau_s\rangle}\right\}^* + \sum\{\dot{\omega}_s\hat{e}_{v,s}\}^* \tag{109}$$

In the above equations, χ_s represents the species mole fractions, which are non-dimensional. The source terms in the equations are separately handled in the point-implicit solver, and their non-dimensionalization is not been included here.

After rearranging and combining the factors on each side, these equations look like:

$$\left\{\frac{\rho_\infty V_\infty}{L}\right\}\left\{\frac{\partial \rho^*}{\partial t^*} + \frac{\partial}{\partial x^{*i}}\rho^* u^{*i}\right\} = 0 \tag{110}$$

$$\left\{\frac{\rho_\infty V_\infty^2}{L}\right\}\left\{\frac{\partial}{\partial t^*}\rho^* u^{*j}+\frac{\partial}{\partial x^{*i}}\rho^* u^{*j}u^{*i}+\frac{\partial p^*}{\partial x^{*j}}\right\}= \left\{\frac{\partial}{\partial x^{*i}}\left[\mu^*\left(\frac{\partial u^{*j}}{\partial x^{*i}}+\frac{\partial u^{*i}}{\partial x^{*j}}\right)-\frac{2}{3}\mu^*\frac{\partial u^{*k}}{\partial x^{*k}}\delta^{ij}\right]\right\}\left\{\frac{\mu_\infty V_\infty}{L^2}\right\} \quad (111)$$

$$\left\{\frac{\rho_\infty V_\infty^3}{L}\right\}\left\{\frac{\partial}{\partial t^*}\rho^* e^*+\frac{\partial}{\partial x^{*i}}\rho^*\left(e^*+\frac{p^*}{\rho^*}\right)u^{*i}\right\}=\frac{\partial}{\partial x^{*i}}\left(K_{tr}^*\frac{\partial T_{tr}^*}{\partial x^{*i}}+K_v^*\frac{\partial T_v^*}{\partial x^{*i}}\right)\left\{\frac{K_{\mathrm{ND}}T_\infty}{L^2}\right\}+ \frac{\partial}{\partial x^{*i}}\left(\rho^*\sum h_s^* D_s^*\frac{\partial \chi_s}{\partial x^{*i}}\right)\left\{\frac{\rho_\infty V_\infty^2 D_{\mathrm{ND}}}{L^2}\right\}+ \frac{\partial}{\partial x^{*i}}\left[u^{*j}\mu^*\left(\frac{\partial u^{*j}}{\partial x^{*i}}+\frac{\partial u^{*i}}{\partial x^{*j}}\right)-u^{*j}\frac{2}{3}\mu^*\frac{\partial u^{*k}}{\partial x^{*k}}\delta^{ij}\right]\left\{\frac{\mu_\infty V_\infty^2}{L^2}\right\} \quad (112)$$

$$\left\{\frac{\rho_\infty V_\infty}{L}\right\}\left\{\frac{\partial \rho_s^*}{\partial t^*}+\frac{\partial}{\partial x^{*i}}\rho_s^* u^{*i}\right\}=\frac{\partial}{\partial x^{*i}}\left(\rho^* D_s^*\frac{\partial \chi_s}{\partial x^{*i}}\right)\left\{\frac{\rho_\infty D_{\mathrm{ND}}}{L^2}\right\}+\{\dot{\omega}_s\}^* \quad (113)$$

$$\left\{\frac{\rho_\infty V_\infty^3}{L}\right\}\left\{\frac{\partial}{\partial t^*}\rho e_v^*+\frac{\partial}{\partial x^{*i}}\rho^* e_v^* u^{*i}\right\}=\frac{\partial}{\partial x^{*i}}\left(K_v^*\frac{\partial T_v^*}{\partial x^{*i}}\right)\left\{\frac{K_{\mathrm{ND}}T_\infty}{L^2}\right\}+ \frac{\partial}{\partial x^{*i}}\left(\rho^*\sum h_{v,s}^* D_s^*\frac{\partial \chi_s}{\partial x^{*i}}\right)\left\{\frac{\rho_\infty V_\infty^2 D_{\mathrm{ND}}}{L^2}\right\}+ \sum\left\{\rho_s\frac{e_{v,s}^*-e_{v,s}}{\langle\tau_s\rangle}\right\}^*+\sum\{\dot{\omega}_s\hat{e}_{v,s}\}^* \quad (114)$$

Canceling out the non-zero terms, these equations further simplify as follows:

$$\frac{\partial \rho^*}{\partial t^*}+\frac{\partial}{\partial x^{*i}}\rho^* u^{*i}=0 \quad (115)$$

$$\frac{\partial}{\partial t^*}\rho^* u^{*j}+\frac{\partial}{\partial x^{*i}}\rho^* u^{*j}u^{*i}+\frac{\partial p^*}{\partial x^{*j}}= \left\{\frac{\partial}{\partial x^{*i}}\left[\mu^*\left(\frac{\partial u^{*j}}{\partial x^{*i}}+\frac{\partial u^{*i}}{\partial x^{*j}}\right)-\frac{2}{3}\mu^*\frac{\partial u^{*k}}{\partial x^{*k}}\delta^{ij}\right]\right\}\left\{\frac{\mu_\infty}{\rho_\infty V_\infty L}\right\} \quad (116)$$

$$\frac{\partial}{\partial t^*}\rho^* e^*+\frac{\partial}{\partial x^{*i}}\rho^*\left(e^*+\frac{p^*}{\rho^*}\right)u^{*i}=\frac{\partial}{\partial x^{*i}}\left(K_{tr}^*\frac{\partial T_{tr}^*}{\partial x^{*i}}+K_v^*\frac{\partial T_v^*}{\partial x^{*i}}\right)\left\{\frac{K_{\mathrm{ND}}T_\infty}{\rho_\infty V_\infty^3 L}\right\}+ \frac{\partial}{\partial x^{*i}}\left(\rho^*\sum h_s^* D_s^*\frac{\partial \chi_s}{\partial x^{*i}}\right)\left\{\frac{D_{\mathrm{ND}}}{V_\infty L}\right\}+ \frac{\partial}{\partial x^{*i}}\left[u^{*j}\mu^*\left(\frac{\partial u^{*j}}{\partial x^{*i}}+\frac{\partial u^{*i}}{\partial x^{*j}}\right)-u^{*j}\frac{2}{3}\mu^*\frac{\partial u^{*k}}{\partial x^{*k}}\delta^{ij}\right]\left\{\frac{\mu_\infty}{\rho_\infty V_\infty L}\right\} \quad (117)$$

$$\frac{\partial \rho_s^*}{\partial t^*} + \frac{\partial}{\partial x^{*i}} \rho_s^* u^{*i} = \frac{\partial}{\partial x^{*i}} \left(\rho^* D_s^* \frac{\partial \chi_s}{\partial x^{*i}} \right) \left\{ \frac{D_{\mathrm{ND}}}{V_\infty L} \right\} + \{\dot{\omega}_s\}^* \tag{118}$$

$$\frac{\partial}{\partial t^*} \rho e_v^* + \frac{\partial}{\partial x^{*i}} \rho^* e_v^* u^{*i} = \frac{\partial}{\partial x^{*i}} \left(K_v^* \frac{\partial T_v^*}{\partial x^{*i}} \right) \left\{ \frac{K_{\mathrm{ND}} T_\infty}{\rho_\infty V_\infty^3 L} \right\} + \frac{\partial}{\partial x^{*i}} \left(\rho^* \sum h_{v,s}^* D_s^* \frac{\partial \chi_s}{\partial x^{*i}} \right) \left\{ \frac{D_{\mathrm{ND}}}{V_\infty L} \right\} + \sum \left\{ \rho_s \frac{e_{v,s}^* - e_{v,s}}{\langle \tau_s \rangle} \right\}^* + \sum \{\dot{\omega}_s \hat{e}_{v,s}\}^* \tag{119}$$

In the above form, $\mu_\infty / \rho_\infty V_\infty L$ in Eqs. 116 and 117 is the inverse of the freestream Reynolds number (Re_∞). In order to eliminate the non-dimensionalizing factors for the other transport terms, these must be unity. Therefore,

$$\frac{K_{\mathrm{ND}} T_\infty}{\rho_\infty V_\infty^3 L} = 1 \implies K_{\mathrm{ND}} = \frac{\rho_\infty V_\infty^3 L}{T_\infty} \tag{120}$$

and

$$\frac{D_{\mathrm{ND}}}{V_\infty L} = 1 \implies D_{\mathrm{ND}} = V_\infty L \tag{121}$$

Thus, the final form of the non-dimensionalized equations are:

$$\frac{\partial \rho^*}{\partial t^*} + \frac{\partial}{\partial x^{*i}} \rho^* u^{*i} = 0 \tag{122}$$

$$\frac{\partial}{\partial t^*} \rho^* u^{*j} + \frac{\partial}{\partial x^{*i}} \rho^* u^{*j} u^{*i} + \frac{\partial p^*}{\partial x^{*j}} = \frac{\partial}{\partial x^{*i}} \left[\mu^* \left(\frac{\partial u^{*j}}{\partial x^{*i}} + \frac{\partial u^{*i}}{\partial x^{*j}} \right) - \frac{2}{3} \mu^* \frac{\partial u^{*k}}{\partial x^{*k}} \delta^{ij} \right] \frac{1}{\mathrm{Re}_\infty} \tag{123}$$

$$\frac{\partial}{\partial t^*} \rho^* e^* + \frac{\partial}{\partial x^{*i}} \rho^* \left(e^* + \frac{p^*}{\rho^*} \right) u^{*i} = \frac{\partial}{\partial x^{*i}} \left(K_{tr}^* \frac{\partial T_{tr}^*}{\partial x^{*i}} + K_v^* \frac{\partial T_v^*}{\partial x^{*i}} \right) + \frac{\partial}{\partial x^{*i}} \left(\rho^* \sum h_s^* D_s^* \frac{\partial \chi_s}{\partial x^{*i}} \right) + \frac{\partial}{\partial x^{*i}} \left[u^{*j} \mu^* \left(\frac{\partial u^{*j}}{\partial x^{*i}} + \frac{\partial u^{*i}}{\partial x^{*j}} \right) - u^{*j} \frac{2}{3} \mu^* \frac{\partial u^{*k}}{\partial x^{*k}} \delta^{ij} \right] \frac{1}{\mathrm{Re}_\infty} \tag{124}$$

$$\frac{\partial \rho_s^*}{\partial t^*} + \frac{\partial}{\partial x^{*i}} \rho_s^* u^{*i} = \frac{\partial}{\partial x^{*i}} \left(\rho^* D_s^* \frac{\partial \chi_s}{\partial x^{*i}} \right) + \{\dot{\omega}_s\}^* \tag{125}$$

$$\frac{\partial}{\partial t^*}\rho e_v^* + \frac{\partial}{\partial x^{*i}}\rho^* e_v^* u^{*i} = \frac{\partial}{\partial x^{*i}}\left(K_v^* \frac{\partial T_v^*}{\partial x^{*i}}\right) + \frac{\partial}{\partial x^{*i}}\left(\rho^* \sum h_{v,s}^* D_s^* \frac{\partial \chi_s}{\partial x^{*i}}\right) + \sum\left\{\rho_s \frac{e_{v,s}^* - e_{v,s}}{\langle\tau_s\rangle}\right\}^* + \sum\{\dot{\omega}_s \hat{e}_{v,s}\}^* \quad (126)$$

where,

$$K_{tr}^* = \frac{K_{tr}}{\rho_\infty V_\infty^3 L/T_\infty} \qquad K_v^* = \frac{K_v}{\rho_\infty V_\infty^3 L/T_\infty} \quad (127)$$

and

$$D_s^* = \frac{D_s}{V_\infty L} \quad (128)$$

REFERENCES

[1] "Sun fact sheet."

[2] "Top 500 supercomputers."

[3] "Planetary Mission Entry Vehicles: Quick Reference Guide." NASA/SP-2006-3401, 2006.

[4] AeroSoft, *GASP Version 3 User's Manual*. AeroSoft Inc., 1872 Pratt Drive, Suite 1275, Blacksburg, VA 24060-6363, 1996.

[5] Anderson, W. K. and Bonhaus, D. L., "An implicit upwind algorithm for computing turbulent flows on unstructured grids," *Computers & Fluids*, vol. 23, no. 1, pp. 1–21, 1994.

[6] Arslanbekov, R. R., Kolobov, V. I., and Frolova, A. A., "Analysis of compressible viscous flow solvers with adaptive Cartesian mesh," in *20th AIAA Computational Fluid Dynamics Conference*, no. 11-3381, 2011.

[7] Berger, M., Aftosmis, M. J., and Allmaras, S. R., "Progress towards a Cartesian cut-cell method for viscous compressible flow," in *50th AIAA Aerospace Sciences Meeting Including the New Horizons Forum and Aerospace Exposition*, no. 12-1301, 2012.

[8] Bird, G., "Approach to translational equilibrium in a rigid sphere gas," *Physics of Fluids*, vol. 6, no. 10, pp. 1518–1519, 1963.

[9] Bird, G., *Molecular Gas Dynamics and the Direct Simulation of Gas Flows*. Clarendon Press, 1994.

[10] Bird, G., "The DS2V/3V program suite for DSMC calculations," *AIP Conference Proceedings*, vol. 762, pp. 541–546, 2004.

[11] Bose, D., "Hypersonic aerodynamics, aerothermodynamics and plasmadynamics research activities within nasa's fundamental aeronautics program hypersonic aerodynamics, aerothermodynamics and plasmadynamics research activities within NASA's Fundamental Aeronautics Program," in *16th AIAA/DLR/DGLR International Space Planes and Hypersonic Systems and Technologies Conference*, no. 09-7278, 2009.

[12] Boyd, I., "Modeling of plasma formation in rarefied hypersonic entry flows," in *45th AIAA Aerospace Sciences Meeting and Exhibit*, no. 07-0206, 2007.

[13] Boyd, I. and Wang, W.-L., "Monte carlo computations of hypersonic interacting flows," in *39th AIAA Aerospace Sciences Meeting and Exhibit*, no. 01-1029, 2001.

[14] Candler, G. V., *The Computation of Weakly Ionized Hypersonic Flows in Thermo-Chemical Nonequilibrium*. PhD thesis, Department of Aeronautics and Astronautics, Stanford University, 1988.

[15] Candler, G. V., Barnhardt, M. D., Drayna, T. W., Nompelis, I., Peterson, D. M., and Subbareddy, P., "Unstructured grid approaches for accurate aeroheating simulations," in *18th AIAA Computational Fluid Dynamics Conference*, no. 07-3959, 2007.

[16] Candler, G. V. and MacCormack, R. W., "The computation of hypersonic ionized flows in chemical and thermal nonequilibrium," *Journal of Thermophysics and Heat Transfer*, vol. 5, no. 3, pp. 266–273, 1991.

[17] Candler, G. V., Mavriplis, D. J., and no, L. T., "Current status and future prospects for the numerical simulation of hypersonic flows," in *47th AIAA Aerospace Sciences Meeting including The New Horizons Forum and Aerospace Exposition*, no. 09-0153, 2009.

[18] Chen, Y.-N., Yang, S.-C., and Yang, J.-Y., "Implicit weighted essentially non-oscillatory schemes for the incompressible Navier-Stokes equations," *International Journal of Numerical Methods in Fluids*, vol. 31, no. 4, 1999.

[19] Clarke, D., Hassan, H., and Salas, M., "Euler calculations for multi-element airfoils using Cartesian grids," *AIAA Journal*, vol. 24, no. 3, pp. 353–358, 1986.

[20] Coakley, T., "Implicit upwind methods for the compressible Navier-Stokes equations," in *6th AIAA Computational Fluid Dynamics Conference*, no. 83-1958, 1983.

[21] Dietrich, S. and Boyd, I., "Scalar and parallel optimized implementation of the direct simulation Monte Carlo method," *Journal of Computational Physics*, vol. 126, no. 2, pp. 328–342, 1996.

[22] Dunn, M. G. and Kang, S.-W., "Theoretical and experimental studies of reentry plasmas," Tech. Rep. 2232, NASA CR, 1973.

[23] Edquist, K. T. and Alter, S. J., "Computational aeroheating predictions for Mars lander configurations," in *36th AIAA Thermophysics Conference*, no. 03-3639, 2003.

[24] Edquist, K., Dyakonov, A., Wright, M., and Tang, C.-Y., "Aerothermodynamic design of the Mars Science Laboratory heatshield," in *41st AIAA Thermophysics Conference*, no. 09-4075, 2009.

[25] Edquist, K., Hollis, B., Dyakonov, A., Laub, B., Wright, M., Rivellini, T. P., Slimko, E., and Willcockson, W., "Mars Science Laboratory entry capsule aerothermodynamics and thermal protection system," in *IEEE Aerospace Conference*, no. 1423, 2007.

[26] Fay, J. and Riddell, F., "Theory of stagnation point heat transfer in dissociated air," *Journal of the Aeronautical Sciences*, vol. 25, no. 2, pp. 73–85, 1958.

[27] Gnoffo, P., Braun, R., Weilmuenster, K., Micheltree, R., Engelund, W., and Powell, R., "Prediction and validation of the Mars Pathfinder hypersonic aerodynamic database," *Journal of Spacecraft and Rockets*, vol. 36, no. 3, pp. 367–373, 1999.

[28] Gnoffo, P., Weilmuenster, K., Braun, R., and Cruz, C., "Influence of sonic line location on Mars Pathfinder probe aerothermodynamics," *Journal of Spacecraft and Rockets*, vol. 33, no. 2, pp. 169–177, 1996.

[29] Gnoffo, P. A., "An upwind-biased point-implicit relaxation algorithm for viscous, compressible perfect-gas flows," Tech. Rep. 2953, NASA TP, 1990.

[30] Gnoffo, P. A., Gupta, R. N., and Shinn, J. L., "Conservation equations and physical models for hypersonic air flows in thermal and chemical nonequilibrium," Tech. Rep. 2867, NASA TP, 1989.

[31] Gnoffo, P. A., Weilmuenster, K. J., Hamilton II, H. H., Olynick, D. R., and Venkatapathy, E., "Computational aerothermodynamic design issues for hypersonic vehicles," in *32nd AIAA Thermophysics Conference Proceedings*, no. 97-2473, 1997.

[32] Gnoffo, P. A. and White, J. A., "Computational aerothermodynamic simulation issues on unstructured grids," in *37th AIAA Thermophysics Conference*, no. 04-2371, 2004.

[33] Gorshkov, A. B., *Aerodynamic Heating at Hypersonic Speed*, pp. 233–252. InTech, 2011.

[34] Gupta, R. N., Yos, J. M., Thompson, R. A., and Lee, K.-P., "A review of reaction rates and thermodynamic and transport properties for an 11-species air model for chemical and thermal nonequilibrium calculations to 30 000K," Tech. Rep. 1232, NASA RP, 1990.

[35] Hamilton, H. H., Weilmuenster, K. J., and DeJarnette, F. R., "Improved approximate method for computing convective heating on hypersonic vehicles using unstructured grids," in *9th AIAA/ASME Joint Thermophysics and Heat Transfer Conference*, no. 06-3394, 2006.

[36] Hamilton, H. H., Weilmuenster, K. J., and DeJarnette, F. R., "Approximate method for computing laminar and turbulent convective heating on hypersonic vehicles using unstructured grids," in *41st AIAA Thermophysics Conference*, no. 09-4310, 2009.

[37] Hartmann, D., Meinke, M., and Shröder, W., "A strictly conservative Cartesian cut-cell method for compressible viscous flows on adaptive grids," *Computer Methods in Applied Mechanics and Engineering*, vol. 200, pp. 1038–1052, 2011.

[38] Harvey, J. K., "A review of a validation exercise on the use of the DSMC method to compute viscous/inviscid interactions in hypersonic flow," in *36th AIAA Thermophysics Conference*, no. 03-3643, 2003.

[39] Harvey, J. K., Holden, M. S., and Wadhams, T. P., "Code validation study of laminar shock/boundary layer and shock/shock interactions in hypersonic flow. part b: Comparisons with Navier-Stokes and DSMC solutions," in *39th AIAA Aerospace Sciences Meeting and Exhibit*, no. 01-1031, 2001.

[40] Hash, D., Olejniczak, J., Wright, M. J., Prabhu, D. K., Pulsonetti, M., Hollis, B., Gnoffo, P. A., Barnhardt, M. D., Nompelis, I., and Candler, G. V., "Fire II calculations for hypersonic nonequilibrium aerothermodynamics code verification: DPLR, LAURA, and US3D," in *45th AIAA Aerospace Sciences Meeting and Exhibit*, no. 07-0605, 2007.

[41] Haüser, J., Vinckier, A., Zemsch, S., and Paap, H., *Supercomputing in hypersonic flow with non-equilibrium effects*, pp. 273–308. Computational Mechanics Publications, 1993.

[42] Hirsch, C., *Numerical Computation of Internal and External Flows : Volume 1 Fundamentals of Numerical Discretization*. John Wiley and Sons, 1991.

[43] Holden, M. S. and Wadhams, T. P., "A review of experimental studies for DSMC and Navier-Stokes code validation in laminar regions of shock/shock and shock/boundary layer interactions including real gas effects in hypervelocity flows," in *36th AIAA Thermophysics Conference*, no. 03-3641, 2003.

[44] Hollis, B., Streipe, S., Wright, M., Bose, D., Sutton, K., and Takashima, N., "Prediction of the aerothermodynamic environment of the Huygens probe," in *38th AIAA Thermophysics Conference*, no. 05-4816, 2005.

[45] John D. Anderson, J., *Computational Fluid Dynamics*. McGraw-Hill, 1995.

[46] John D. Anderson, J., *Hypersonic and High-Temperature Gas Dynamics*. AIAA Education Series, AIAA, 2006.

[47] Kim, K. H., Kim, C., and Rho, O. H., "Methods for the accurate computations of hypersonic flows, I. AUSMPW+ scheme," *Journal of Computational Physics*, vol. 174, pp. 38–80, 2001.

[48] Kim, K. H., Lee, J. H., and Rho, O. H., "An improvement of AUSM schemes by introducing the pressure-based weight functions," *Computers & Fluids*, vol. 27, no. 3, pp. 311–346, 1998.

[49] Klein, A., "Implementation of an implicit LU-SSOR scheme in a parallel unstructured Cartesian grid Navier-Stokes solver," 2006.

[50] Lee, J. D., *Development of an Efficient Viscous Approach in a Cartesian Grid Framework and Application to Rotor-Fuselage Interaction*. PhD thesis, School of Aerospace Engineering, Georgia Institute of Technology, 2006.

[51] Lee, J. W., *Parallelized Cartesian Grid Methodology for Non-equilibrium Hypersonic Flow Analysis of Ballutes*. PhD thesis, School of Aerospace Engineering, Georgia Institute of Technology, 2007.

[52] Lee, J.-H., *Basic Governing Equations for the Flight Regimes of Aeroassisted Orbital Transfer Vehicles*, vol. 96 of *Progress in Astronautics and Aeronautics*, pp. 3–53. AIAA, 1985.

[53] Liou, M.-S. and Steffen, C. J., "A new flux splitting scheme," *Journal of Computational Physics*, vol. 107, no. 1, pp. 23–39, 1993.

[54] Lofthouse, A. J., *Nonequilibrium Hypersonic Aerothermodynamics Using the Direct Simulation Monte Carlo and Navier-Stokes Models*. PhD thesis, Department of Aerospace Engineering, The University of Michigan, 2008.

[55] MacCormack, R. W. and Candler, G. V., "The solution of the Navier-Stokes equations using Gauss-Seidel line relaxation," *Computers & Fluids*, vol. 17, no. 1, pp. 135–150, 1989.

[56] Maicke, B., Majdalani, J., and Barber, T., "Evaluation of CFD codes for hypersonic flow modeling," in *46th AIAA/ASME/SAE/ASEE Joint Propulsion Conference and Exhibit*, no. 10-7184, 2010.

[57] Marshall, D. D., *Extending the Functionalities of Cartesian Grid Solvers: Viscous Effects Modeling and MPI Parallelization*. PhD thesis, School of Aerospace Engineering, Georgia Institute of Technology, 2002.

[58] Marshall, D. D. and Ruffin, S. M., "An embedded boundary Cartesian grid scheme for viscous flows using a new viscous wall boundary condition treatment," in *42nd AIAA Aerospace Sciences Meeting and Exhibit*, no. 04-0581, 2004.

[59] Marshall, D. D. and Ruffin, S. M., "A new inviscid wall boundary condition treatment for embedded boundary Cartesian grid schemes," in *42nd AIAA Aerospace Sciences Meeting and Exhibit*, no. 04-0583, 2004.

[60] McBride, B. J., Gordon, S., and Reno, M. A., "Coefficients for calculating thermodynamic and transport properties of individual species," Tech. Rep. 4513, NASA TM, 1993.

[61] McBride, B. J., Zehe, M. J., and Gordon, S., "NASA Glenn coefficients for calculating thermodynamic properties of individual species," Tech. Rep. 2002-211556, NASA TP, 2002.

[62] Micheltree, R., Wilmoth, R., Cheatwood, F., Brauckmann, G., and Greene, F., "Aerodynamics of Stardust sample return capsule," in *15th AIAA Applied Aerodynamics Conference*, no. 97-2304, 1997.

[63] Moss, J. N. and Bird, G. A., "DSMC simulations of hypersonic flows with shock interactions and validation with experiments," in *37th AIAA Thermophysics Conference*, no. 04-2585, 2004.

[64] Moss, J. and Bird, G., "Direct simulation of transitional flow for hypersonic reentry conditions," *Journal of Spacecraft and Rockets*, vol. 40, no. 5, pp. 830–843, 2003.

[65] Moss, J. and Bird, G., "Direct simulation Monte Carlo simulations of hypersonic flows with shock interactions," *AIAA Journal*, vol. 43, no. 12, pp. 2565–2573, 2005.

[66] Moss, J., Blanchard, R., Wilmoth, R., and Braun, R., "Mars Pathfinder rarefied aerodynamics," *Journal of Spacecraft and Rockets*, vol. 36, no. 3, pp. 330–339, 1999.

[67] Nompelis, I., Drayna, T. W., and Candler, G. V., "Development of a hybrid unstructured implicit solver for the simulation of reacting flows over complex geometries," in *34th AIAA Fluid Dynamics Conference and Exhibit*, no. 04-2227, 2004.

[68] Nompelis, I., Drayna, T. W., and Candler, G. V., "A parallel unstructured implicit solver for hypersonic reacting flow simulation," in *17th AIAA Computational Fluid Dynamics Conference*, no. 05-4867, 2005.

[69] Olynick, D., Chen, Y., and Tauber, M., "Aerothermodynamics of the Stardust Sample Return Capsule," *Journal of Spacecraft and Rockets*, vol. 36, no. 3, pp. 442–462, 1999.

[70] Olynick, D. R., Henline, W. D., Chambers, L. H., and Candler, G. V., "Comparison of coupled radiative flow solutions with Project Fire II flight data," *Journal of Thermophysics and Heat Transfer*, vol. 9, no. 4, pp. 586–594, 1995.

[71] Ozawa, T., Zhong, J., Levin, D., Boger, D., and Wright, M., "Modeling of the Stardust reentry flows with ionization in DSMC," in *45th AIAA Aerospace Sciences Meeting and Exhibit*, no. 07-0611, 2007.

[72] Park, C., "On convergence of computation of chemically reacting flows," in *23rd AIAA Aerospace Sciences Meeting and Exhibit*, no. 85-0247, 1985.

[73] Park, C., *Problems of Rate Chemistry in the Flight Regimes of Aeroassisted Orbital Trnasfer Vehicles*, vol. 96 of *Progress in Astronautics and Aeronautics*, pp. 511–537. AIAA, 1985.

[74] Park, C., "Assessment of two-temperature kinetic model for ionizing air," in *22nd AIAA Thermophysics Conference*, no. 87-1574, 1987.

[75] Park, C., "A review of reaction rates in high temperature air," in *24th AIAA Thermophysics Conference*, no. 89-1740, 1989.

[76] Park, C., *Nonequilibrium Hypersonic Aerothermodynamics*. John Wiley and Sons, 1990.

[77] Park, C., "Review of chemical-kinetic problems of future NASA missions, I: Earth entries," *Journal of Thermophysics and Heat Transfer*, vol. 7, no. 3, pp. 385–398, 1993.

[78] Park, C., Howe, J. T., Jaffe, R. L., and Candler, G. V., "Review of chemical-kinetic problems of future NASA missions, II: Mars entries," *Journal of Thermophysics and Heat Transfer*, vol. 8, no. 1, pp. 9–22, 1994.

[79] Park, C. and Yoon, S., "Fully coupled implicit method for thermochemical nonequilibrium air at suborbital fligh speeds," *Journal of Spacecraft and Rockets*, vol. 28, no. 1, pp. 31–39, 1991.

[80] Peyret, R. and Taylor, T. D., *Computational Methods for Fluid Flow*. Springer Series in Computational Physics, Springer-Verlag, 1983.

[81] Roe, P., "Approximate Riemann solvers, parameter vectors, and difference schemes," *Journal of Computational Physics*, vol. 43, no. 2, pp. 357–372, 1981.

[82] Ruffin, S. M., Zaki, M., and Sekhar, S., "A normal ray refinement technique for Cartesian-grid based Navier-Stokes solvers," *International Journal of Computational Fluid Dynamics*, vol. 26, no. 4, pp. 231–246, 2012.

[83] Scalabrin, L. C., *Numerical Simulation of Weakly Ionized Hypersonic Flow over Reentry Capsules*. PhD thesis, Department of Aerospace Engineering, The University of Michigan, 2007.

[84] Scalabrin, L. C. and Boyd, I. D., "Development of an unstructured Navier-Stokes solver for hypersonic nonequilibrium aerothermodynamics," in *38th AIAA Thermophysics Conference*, no. 05-5203, 2005.

[85] Schwartzentruber, T., *A Modular Particle-Continuum Algorithm for Hypersonic Non-Equilibrium Flows*. PhD thesis, School of Aerospace Engineering, The University of Michigan, 2007.

[86] Schwartzentruber, T. and Boyd, I., "A hybrid particle-continuum method applied to shock waves," *Journal of Computational Physics*, vol. 215, pp. 402–416, 2006.

[87] Schwartzentruber, T., Scalabrin, L., and Boyd, I., "Hybrid particle-continuum simulations of non-equilibrium hypersonic blunt body flow fields," in *9th AIAA/ASME Joint Thermophysics and Heat Transfer Conference*, no. 06–3602, 2006.

[88] Schwartzentruber, T., Scalabrin, L., and Boyd, I., "A modular particle–continuum numerical method for hypersonic non-equilibrium gas flows," *Journal of Computational Physics*, vol. 225, pp. 1159–1174, 2007.

[89] Schwartzentruber, T. E., Scalabrin, L. C., and Boyd, I. D., "Hybrid particle-continuum simulations of hypersonic flow over a hollow-cylinder-flare geometry," *AIAA Journal*, vol. 46, no. 8, pp. 2086–2095, 2008.

[90] Sekhar, S., Zaki, M., Ruffin, S. M., Kolobov, V. I., and Arslanbekov, R. R., "Evaluation of viscous flow solvers with adaptive Cartesian meshes for hypersonic flows," in *42nd AIAA Thermophysics Conference*, no. 11-4035, 2011.

[91] Steger, J. and R.F., W., "Flux vector splitting of the inviscid gasdynamic equations with application to finite-difference methods," *Journal of Computational Physics*, vol. 40, pp. 263–293, 1981.

[92] Tannehill, J. C., Anderson, D. A., and Pletcher, R. H., *Computational Fluid Mechanics and Heat Transfer*. Series in Computational and Physical Processes in Mechanics and Thermal Sciences, Taylor & Francis, 1997.

[93] Tölke, J. and Krafczyk, M., "TeraFLOP computing on a desktop PC with GPUs for 3D CFD," *International Journal of Computational Fluid Dynamics*, vol. 22, no. 7, pp. 443–456, 2008.

[94] Toro, E. F., *Riemann Solvers and Numerical Methods for Fluid Dynamics*. Springer-Verlag, 1997.

[95] Tran, H., Johnson, C., Rasky, D., Hui, F., Hsu, M.-T., Chen, T., Chen, Y., Paragas, D., and Kobayashi, L., "Phenolic Impregnated Carbon Ablators (PICA) as Thermal Protection Systems for Discovery missions," Tech. Rep. 110440, NASA TM.

[96] Tsuboi, N., Yamaguchi, H., and Matsumoto, Y., "Direct simulation monte carlo method on rarefied hypersonic gas flow around flat plates," *Journal of Spacecraft and Rockets*, vol. 41, no. 3, pp. 397–405, 2004.

[97] Tu, S., *Development of a Solution Adaptive Cartesian-Grid Solver for 2-D Thermochemical Nonequilibrium Flows*. PhD thesis, School of Aerospace Engineering, Georgia Institute of Technology, 2001.

[98] Udaykumar, H., Shyy, W., and Rao, M., "Elafint: a mixed Eulerian-Lagrangian method for fluid flows with complex and moving boundaries," *International Journal of Numerical Methods in Fluids*, vol. 22, no. 8, pp. 691–712, 1996.

[99] van Leer, B., "Towards the ultimate conservative difference scheme. V: A second-order sequel to Godunov's method," *Journal of Computational Physics*, vol. 32, no. 1, pp. 101–136, 1979.

[100] Vincenti, W. G. and Kruger Jr., C. H., *Introduction to Physical Gas Dynamics*. New York: John Wiley and Sons, 1965.

[101] Walpot, L., Caillaut, L., Molina, R., Laux, C., and Blanquaert, T., "Convective and radiative heat flux prediction of Huygens entry on Titan," *Journal of Thermophysics and Heat Transfer*, vol. 20, no. 4, pp. 663–671, 2006.

[102] Wang, W.-L., *Hybrid Particle/Continuum Approach for Nonequilibrium Hypersonic Flows*. PhD thesis, Department of Aerospace Engineering, The University of Michigan, 2004.

[103] White, J. A. and Morrison, J. H., "A pseudo-temporal multi-grid relaxation scheme for solving the Parabolized Navier-Stokes equations," in *14th AIAA Computational Fluid Dynamics Conference*, no. 99-3360, 1999.

[104] Wright, M., Beck, R., Edquist, K., Driver, D., Sepka, S., and Slimko, E., "Sizing and margins assessment of the Mars Science Laboratory aeroshell Thermal Protection System," in *41st AIAA Thermophysics Conference*, no. 09-4231, 2009.

[105] Wright, M. J., Candler, G. V., and Bose, D., "Data-Parallel Line Relaxation method for the Navier-Stokes equations," *AIAA Journal*, vol. 36, no. 9, pp. 1603–1609, 1998.

[106] Ye, T., Mittal, R., Udaykumar, H., and Shyyy, W., "An accurate Cartesian grid method for viscous incompressible flows with complex immersed boundaries," *Journal of Computational Physics*, vol. 156, pp. 209–240, 1999.

[107] Yee, L., Bailey, H. E., and Woodward, H. T., "Ballistic range measurements of stagnation-point heat transfer in air and in carbon dioxide at velocities up to 18,000 feet per second," Tech. Rep. D-777, NASA TN, 1961.

[108] Yoon, S., Gnoffo, P. A., White, J. A., and Thomas, J. L., "Computational challenges in hypersonic flow simulations," in *39th AIAA Thermophysics Conference*, no. 07-4265, 2007.

[109] Yoon, S. and Jameson, A., "An LU-SSOR scheme for the Euler and Navier-Stokes equations," in *25th AIAA Aerospac Sciences Meeting*, no. 87-0600, 1987.